Master of Science Thesis

Development of a Fatigue Analysis Tool Using Cohesive Zone Modelling for Composite Specimens

Eva Smeets

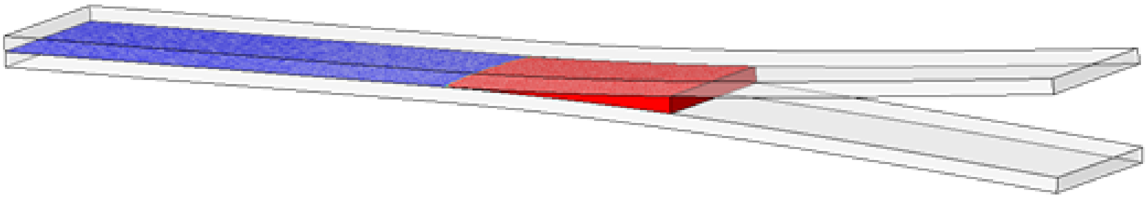

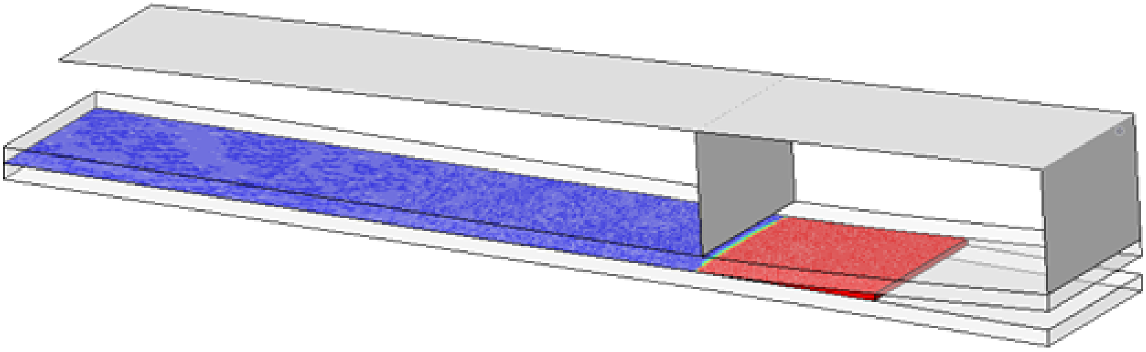

Faculty of Aerospace Engineering · Delft University of Technology

Development of a Fatigue Analysis Tool Using Cohesive Zone Modelling for Composite Specimens

MASTER OF SCIENCE THESIS

For obtaining the degree of Master of Science in Aerospace Engineering
at Delft University of Technology

Eva Smeets

4 November 2019

Faculty of Aerospace Engineering · Delft University of Technology

Delft
University of
Technology

Delft University of Technology
Faculty of Aerospace Engineering
Department of Aerospace Structures and Materials

GRADUATION COMMITTEE

Dated: 4 November 2019

Chair holder: Prof. Dr. Chiara Bisagni

Committee members: Dr. Boyang Chen

Dr. Ir. René Alderliesten

Dr. Antonio Raimondo

Abstract

The purpose of this research project is to implement Cohesive Zone Modelling (CZM) in the finite element analysis of composite structures subjected to fatigue loading. The focus of the research lies in the simulation of delamination growth when an initial delamination is present. Delamination is a common failure mode in composite structures. It can be the result of a number of different things such as impact damage, manufacturing defects, fatigue loading or out-of-plane loading, for example when the structure buckles. The characterisation of the delamination growth behaviour is important to ensure safe design. Simulations are a vital part to this characterisation to decrease the necessity of experimental tests, which are often time-consuming and expensive.

Two different coupon level tests are performed in this project. The first coupon specimen is the Double Cantilever Beam (DCB) specimen to characterise the mode I behaviour of the material. The second coupon is a Mixed-Mode Bending (MMB) specimen that is tested with two different mixed-mode ratios to analyse the mixed-mode behaviour. To carry out the simulations of these specimens, a subroutine is written to incorporate the damage model in Abaqus. At first, the subroutine is applied to the specimens under quasi-static loading. These results are compared to the Linear Elastic Fracture Mechanics (LEFM) analytical computations to verify the subroutine. Thereafter, the same specimens are subjected to fatigue loading. These results are compared to benchmark tests from literature and analytical results.

The subroutines for both the quasi-static and the fatigue analyses of the specimens are based on theoretical models taken from literature. The quasi-static model can be implemented as is. However for the fatigue model some adaptations are necessary. These adaptations are mainly needed in the analysis of mixed-mode loading cases where the calculations for some of the model parameters are adapted to obtain more accurate results.

The results of the quasi-static analyses show a good comparison to the analytical results for the damage onset and the static failure of the coupons. In the fatigue analyses, accurate results are obtained for crack propagation. Some differences are observed for the damage onset. The results for the simulations show a lower cycle count for onset when compared to the benchmark data.

Foreword

This master's thesis marks the end of a challenging research project and the end of my time as a student. I would like to thank my supervisor Prof. Dr. Chiara Bisagni for giving me the opportunity to work on this topic and for her support during the course of the project. Furthermore, I appreciate the advice that Dr. Antonio Raimondo has given me, his knowledge and experience were very helpful during this thesis. Lastly, I am thankful for my family and friends, who were always there for me. I am grateful for your support during this project each of you has contributed, even though you might not be aware of it.

Delft, University of Technology Eva Smeets
4 November 2019

Table of Contents

List of Figures

List of Tables

Nomenclature

Acronyms

CZM	Cohesive Zone Modelling
DCB	Double Cantilever Beam
ENF	End-Notched Flexure
FCG	Fatigue Crack Growth
FE	Finite Element
FI	Failure Index
LCZ	Local Cohesive Zone
LEFM	Linear Elastic Fracture Mechanics
MMB	Mixed-Mode Bending
SERR	Strain Energy Release Rate
TSL	Traction-Separation Law
UMAT	User Material
VCCT	Virtual Crack Closure Technique

Symbols

A_{cz}	Cohesive zone area	$[mm^2]$
D	Damage parameter	$[-]$
$^{da}/_{dN}$	Crack growth rate	$[mm\ cycle^{-1}]$
D_{fu}	Unwanted fatigue damage	$[-]$
D_s	Quasi-static damage	$[-]$
E	Young's modulus	$[Nm^{-2}]$
E_{11}	Longitudinal stiffness	$[Nm^{-2}]$
E_{22}	Transverse stiffness	$[Nm^{-2}]$
E_{33}	Through thickness stiffness	$[Nm^{-2}]$
G_I	Strain energy release rate in mode I	$[Nm^{-1}]$

G_{IC}	Critical strain energy release rate in mode I	$[Nm^{-1}]$
G_{II}	Strain energy release rate in mode II	$[Nm^{-1}]$
G_{IIC}	Critical strain energy release rate in mode II	$[Nm^{-1}]$
G_C	Critical strain energy release rate	$[Nm^{-1}]$
G_{max}	Maximum strain energy release rate during the fatigue cycle	$[Nm^{-1}]$
G_{min}	Minimum strain energy release rate during the fatigue cycle	$[Nm^{-1}]$
G_T	Total strain energy release rate	$[Nm^{-1}]$
G_{TC}	Total critical strain energy release rate	$[Nm^{-1}]$
G_{th}	Strain energy release rate threshold	$[Nm^{-1}]$
K	Stress intensity factor	$[-]$
l_{cz}	Cohesive zone length	$[mm]$
l_d	Length of the damaged zone	$[mm]$
l^e	Element length	$[mm]$
l_{fat}	Cohesive zone length under fatigue loading	$[mm]$
N	Fatigue cycles	$[cycles]$
R	Stress ratio	$[-]$
S_a	Stress amplitude	$[Nm^{-2}]$
S_{max}	Maximum applied stress during the fatigue cycle	$[Nm^{-2}]$
S_{min}	Minimum applied stress during the fatigue cycle	$[Nm^{-2}]$
S_{UT}	Ultimate stress	$[Nm^{-2}]$

Greek symbols

Δ^0	Damage onset threshold	$[mm]$
Δ^f	Final displacement jump	$[mm]$
δ_m^f	Maximum mixed-mode dislpacement	$[mm]$
ΔG	Change in strain energy release rate	$[Nm^{-1}]$
η	Benzeggagh-Kenane coefficient	$[-]$
λ	Displacement jump	$[mm]$
ν	Poisson's ratio	$[-]$
σ^c	Material strength	$[Nm^{-2}]$
σ_m	Maximum stress	$[Nm^{-2}]$
τ	Interface traction	$[Nm^{-2}]$

Chapter 1

Introduction

In the last decades, composite materials have been used more frequently due to their high specific strength and stiffness. A composite material is composed of different laminae consisting of unidirectional fibres embedded in a matrix material. The intrinsic strength and stiffness in fibre direction of each of these laminae are typical for the beneficial structural properties of composite materials. Furthermore, the laminae are stacked in different orientations to create a laminate that exhibits these structural properties in each of the fibre directions of the laminae.

These materials are more complex than the traditional metals because composites have an anisotropic behaviour due to the stacking of the laminae. This leads to an increased complexity in failure modes. Failure of composite materials can occur in the fibres, the matrix, or the fibre-matrix interface. When the fibre-matrix interface fails, delamination of the composite material occurs. These delaminations can be caused by, among other reasons, impact damage, loading perpendicular to the fibre direction or manufacturing defects. When a composite material is delaminated, there is a decline in the structural properties of the material. This deterioration can lead to failure of the entire structure.

To decrease the risk of failure, stringers are used to stiffen the skin in locations where high loading occurs, such as the fuselage and the wings of an aircraft. In these locations, the stiffened skin is subjected to in-plane loading, which does not result in any out-of-plane deformation in normal circumstances. Under severe loading cases, the stiffened skin can undergo buckling.

The buckling load of a composite structure is significantly lower than its failure load. If buckling would be allowed during service, lighter structures could be designed. However, buckling will cause out-of-plane deformations on skin stiffened panels. This results in the initiation of delamination of the skin-stiffener interface. During flight, this interface is subjected to fatigue loading, causing the delamination to propagate.

To ensure safe design it is important to predict the delamination propagation. Experimental tests with high cycle fatigue loading are very expensive, especially due to the duration of the test. Therefore, simulation tools are being developed to predict the delamination growth.

Due to the complexity in the prediction of failure modes of composite materials, a building block approach is used. This approach entails that knowledge is built step by step, from the coupon level to the full scale structure.

This thesis presents the development of a fatigue response simulation tool using Cohesive Zone Modelling (CZM) for composite structures at coupon level. The CZM is a technique to analyse the behaviour of an interface. The model is based on a specific Traction-Separation Law (TSL) which relates interface tractions to separations. In order to determine the capabilities of CZM, a series of coupon level Finite Element (FE) tests is performed and compared to benchmark results. This forms the basis for the expansion of the model to element level specimens, such as a single stringer compression specimen [1–4], according to the building block approach.

In Chapter 2, a literature study can be found. Different sources have been analysed. The chapter includes the foundations of the theory of fatigue response analysis, the use of CZM for the analysis of static loading, as well as the implementation of fatigue loading into the concept of CZM. Furthermore, the literature study has resulted in the definition of a research objective and multiple research questions to define the scope of the thesis work, presented in Chapter 3.

Chapter 4 describes the theoretical framework that forms the basis for the analyses. It includes the detailed formulation of a CZM for static loading and the expansion to the analysis of fatigue loading. A description of the subroutine for the implementation in Abaqus is also given. Furthermore, the procedure for the verification and validation of the model is presented. Lastly, as an additional verification, a Linear Elastic Fracture Mechanics (LEFM) formulation for the calculation of the global Strain Energy Release Rate (SERR) and compliance based on the crack length is presented.

The set-up of the FE specimens is described in Chapter 5. The material parameters for the composite specimens can be found here. The specific parameters for the Traction-Separation Law (TSL) of the different specimens are also presented. Furthermore the element distribution and the boundary conditions of the specimens are shown.

The results of the FE analyses are presented in Chapter 6. As an initial check for the written user subroutine and the FE models, the results of the static analyses are compared to the results of the same specimens with the constitutive model that is included in Abaqus 2017. The fatigue results are compared to a benchmark that was obtained with another numerical method based on LEFM.

Finally, Chapter 7 contains the conclusions drawn from the results, and some recommendations for future research into the simulation skin-stiffener separation under fatigue loading.

Chapter 2

Literature Review

This literature review is divided in three sections.
Section 2.1 is an overview of the current state of the theory regarding the fatigue characterization of composite structures.
In Section 2.2, the different methods for modelling interface behaviour under static loading are presented. The Virtual Crack Closure Technique (VCCT) is discussed briefly, but the main focus of the section is CZM since this is the method that will be used in the following research project. The different approaches to the relation between traction and separation of an interface are discussed as well as other characteristics of this method.
Different methods for the implementation of fatigue behaviour into CZM are discussed in Section 2.3. Four of the methods are based on the Paris relation. These methods differ from each other in the way they calculate the increase in damage per cycle. Another method uses a local approach that is based on the S-N curve rather than the Paris relation.

2.1 Fatigue Characterisation

This section contains a brief overview of the description of fatigue loading, fracture mechanics in composite materials and the methods for fatigue characterization. The fatigue characterisation can be divided into two major categories. The first one are the stress-fatigue life techniques, which are based on constructing a curve of the fatigue life, N, versus the stress amplitude, S_a, based on a number of tests. The second category are the Fatigue Crack Growth (FCG) techniques where the fatigue life calculations are based on the speed of crack growth.

2.1.1 Loading description

To characterise the fatigue loading of a specimen, several variables are used. The applied stress is defined as a function of time as can be seen in Figure 2.1. In this case, only constant amplitude loading is considered.

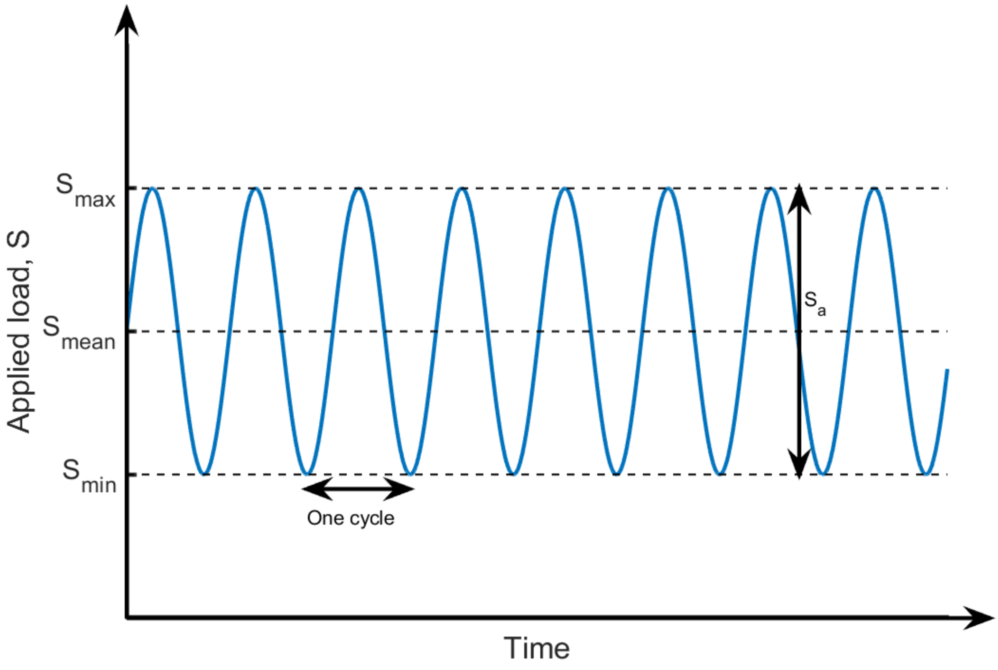

Figure 2.1: Constant amplitude loading.

The load cycles between the maximal applied stress, S_{max}, and the minimum applied stress, S_{min}. The stress amplitude S_a is the difference between S_{max} and S_{min}.

$$S_a = \Delta S = S_{max} - S_{min} \tag{2.1}$$

In the computations regarding fatigue analyses, the stress ratio is often used as a parameter to define the loading. The stress ratio is defined as:

$$R = \frac{S_{min}}{S_{max}} \tag{2.2}$$

2.1.2 Fracture mechanics

Fracture mechanics deals with the study of crack propagation. This section describes the concepts of the stress intensity factor, the strain energy release rate and the opening modes, which are important for the fatigue characterisation of materials. Both concepts are used to describe the loading state of a structure.

Stress intensity factor

In isotropic materials, the stress intensity factor is used as a way to characterise the stress state of the structure with a crack. It is a non-dimensionless factor that accounts for the shape of the structure and the applied load [5].

In a plate with an infinite width and a straight crack, the stress intensity factor, K, is calculated with:

$$K = \beta S \sqrt{\pi a} \tag{2.3}$$

where S is the applied stress level and a is the crack length. β is a geometry factor that takes the shape of the crack tip into account. Since K has a linear relation with the applied stress, S, it cycles in the same way. Thus we can define the maximum K during the fatigue cycle, K_{max} and the minimum K during the cycle, K_{min}. The stress ratio, R, is the same for the applied stress as for the stress intensity factor:

$$R = \frac{S_{min}}{S_{max}} = \frac{K_{min}}{K_{max}} \tag{2.4}$$

For plates with a finite width, a geometry correction factor, β is introduced in Equation 2.3. Many different calculations of this factor have been presented for different geometries.

Strain Energy Release Rate (SERR)

The SERR, G, is often used to characterise a fracture process. It is the energy that is dissipated per unit of newly created fracture surface during crack growth. This is equal to the energy that must be supplied to a crack so that it can grow. For this reason it is also called the crack driving force [5].

Fatigue analyses in composite often use criteria based on energy rather then stress-based criteria, such as K, for two main reasons. Firstly, when the crack has a known shape, such as an elliptical hole, the stress at the crack tip has a known distribution. However, in the case of cracks, where the radius of the crack tip is infinitesimally small, the stress distribution is not easily determined. Secondly, the different constituents of a composite material usually have different stiffnesses. Due to these differences, the crack resistant properties are not the same in every direction. This results in an irregular stress field at the crack tip, where it is difficult to obtain the exact distribution [6]. The use of the SERR avoids the need to calculate the stress distribution at the crack tip. In the analysis of fatigue response, the critical SERR is often used as a parameter to characterise the material. This parameters defines the resistance of the material against crack growth meaning that crack growth will occur when the release rate of the strain energy exceeds the critical value.

Opening Modes

In the characterisation of crack growth, it is important to know in which direction the crack is opening. For this reason, three opening modes are determined. These modes are shown in Figure 2.2.

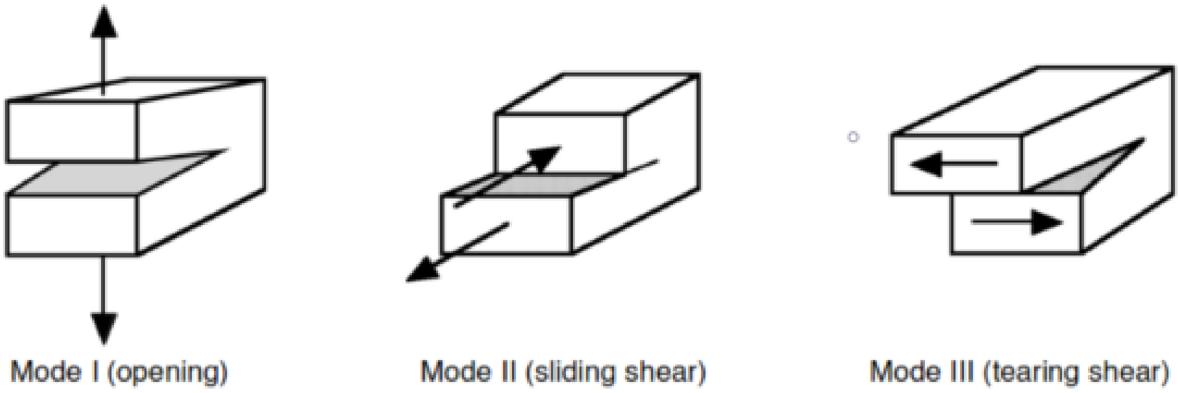

Figure 2.2: The three different opening modes [7].

All possible loading cases can be described as a combination of these three opening modes. In research on coupon level, the opening modes are often isolated to study their influence on the material. Sometimes mixed-mode coupon tests are also performed, where the ratio between the different modes is known. The damage behaviour for mode I opening is characterised using the Double Cantilever Beam (DCB) specimen [6]. Manufacturing imperfections can influence the results of these tests as they might introduce other opening modes into the problem. Mode II characterisation has not been studied as extensively. For this behaviour, End-Notched Flexure (ENF) [8] specimens are the most common. Mixed-Mode Bending (MMB) [9, 10] specimens are used to characterise the behaviour when mode I and II are both present.

The critical SERR for pure mode loading, where only one opening mode is present, is a material parameter that is determined through experimental testing. A real-life structure will rarely be subjected to only one opening mode. Benzeggagh and Kenane [11] have suggested an expression for the calculation of the total critical SERR as a function the critical SERRs for the different opening modes and the ratio in which these modes are present, $\frac{G_{II}}{G_T}$. Their proposed relation is:

$$G_{TC} = G_{IC} + (G_{IIC} - G_{IC}) \left(\frac{G_{II}}{G_T}\right)^{\eta} \tag{2.5}$$

where η is a semi-empirical coefficient and $G_T = G_I + G_{II}$. With experimental testing, this relation has been proven to be accurate for epoxy and PEEK composites [12].

2.1.3 Fatigue Crack Growth (FCG)

With the FCG curves, the fatigue life of a specimen is calculated using the increase in crack length, a, per cycle, N, $^{da}/_{dN}$ as a parameter as a function of a fracture mechanics parameter (K or SERR).

An example containing crack growth results can be seen in Figure 2.3. Here the crack growth rate is shown as a function of ΔK which is defined as $K_{max} - K_{min}$.

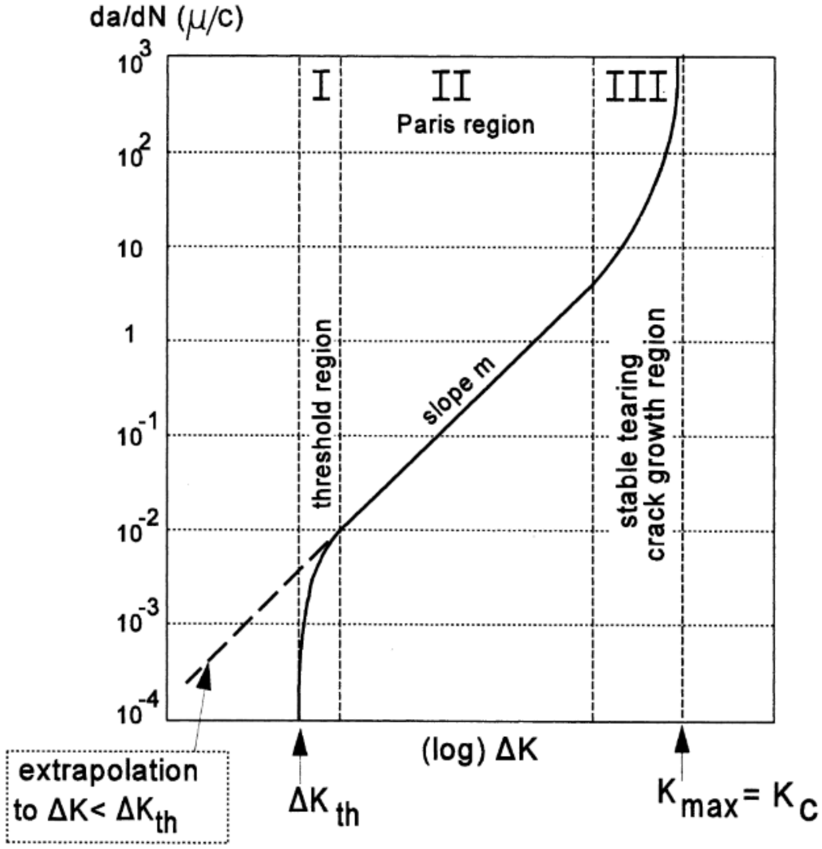

Figure 2.3: Crack growth rate results as a function of ΔK [5, p. 218]

Region I from this figure represents the threshold region. The threshold value ΔK_{th} is the level where microscopic cracks grow to macroscopic cracks. If ΔK is lower than this value, the crack growth slows down and it is assumed that no crack growth occurs. For values of ΔK in region II, stable crack growth is assumed. This region is called the Paris region. Paris was the one to describe the relation between the crack growth rate, $^{da}/_{dN}$, and the change in stress intensity factor, ΔK. According to Paris [13], this relation is described by a power function.

$$\frac{da}{dN} = C\Delta K^m \tag{2.6}$$

C and m are the Paris relation constants that are determined by using a power law curve fit on the experimental data such as in Figure 2.3. This expression was developed to characterise the crack growth rate in metals, thus the stress intensity factor is straightforward. In the case of composite materials this is a less straightforward parameter. The deformations around a crack tip in a composite material are constrained by the fibres. This makes it more difficult to determine the stress state around a crack tip.

When characterising the crack growth in composite materials, ΔG and G_{max} are often used to express the Paris relation since it is a more straightforward parameter. ΔG is defined as the difference between the maximal and the minimal SERR during the fatigue cycle, $G_{max} - G_{min}$. The Paris relation becomes:

$$\frac{da}{dN} = C\left(\Delta G\right)^m \tag{2.7}$$

Wang et al. were among the first to determine this relation [14]. With this relation, the graph in Figure 2.3 has the same shape, but the horizontal axis represents ΔG. The Paris relation constants in Equation 2.7 are material specific parameters and are usually determined through experiments.

Region III is called the stable-tearing crack growth region. The crack growth rate is very high, but the crack growth is still stable, because ductile tearing does not occur over the whole crack front. The fatigue life for loading in this region is usually very short, so the significance in engineering analyses is limited. When ΔK is higher than the critical value ΔK_c, final failure occurs and ductile tearing can be seen along the entire crack front.

The FCG is more often used to implement the fatigue damage modelling in numerical methods because it provides a more faithful representation [6]. In these methods, damage variables are established. These variables decrease the material parameters and are updated with the cyclic count and the FCG laws.

2.1.4 S-N curve

A common way to characterise the fatigue behaviour of a specimen is the use of an S-N curve, also called a Wöhler curve [5]. Such a curve is based on experimental data from tests with different stress amplitudes (S_a). After performing a series of fatigue tests, the number of cycles that the specimen can sustain, N, can be plotted against the applied stress amplitude. An example of this can be seen in Figure 2.4.

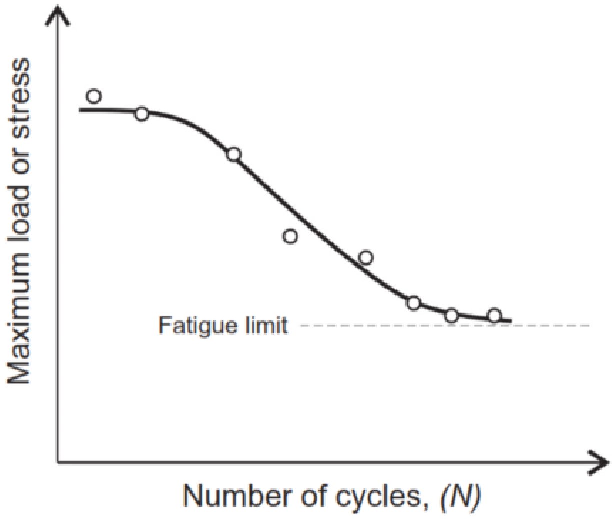

Figure 2.4: Schematic representation of an S-N curve [6, p. 103]

The fatigue life, N, is usually plotted on a logarithmic scale because it frequently results in an approximately linear relation for most of the range. The mathematical relation is written as: [5, p. 144]:

$$S_a^k N = \text{constant} \tag{2.8}$$

where S_a is the stress amplitude, N represents the number of cycles until failure and k is a constant coefficient. If the mean stress is equal to zero, the stress amplitude needed for failure at one cycle is equal to the ultimate strength, S_{UT}. Due to strain hardening, there is an upper horizontal asymptote in the curve. If the stress amplitude, S_a is only slightly smaller than the ultimate stress, S_{UT}, the specimen can survive many more cycles.

Although this approach was originally developed for metals, it has been proven by Campilho and da Silva to be applicable to composite materials. However, with the remark that the approach is better suited for high-cycle fatigue [6]. A shortcoming of this technique is that the fatigue life of a specimen cannot be separated into onset and propagation phases. Finally, the S-N curve is obtained from experimental results on a specific geometry and extrapolation to different geometries has proven inaccurate [15]. This means that fatigue design with the use of the S-N curve can only occur in a late stage of the design process as the information for the S-N curve has to be obtained by analysing the actual structure.

2.2 Modelling Approaches

There are a number of existing approaches to model the interface behaviour of composite materials. The approaches that are discussed here are the Virtual Crack Closure Technique (VCCT) that is based on the SERR and CZM, where the interface behaviour is modelled using a set of cohesive parameters and a TSL that relates the interface separation to the resulting traction.

2.2.1 Virtual Crack Closure Technique (VCCT)

The VCCT is based on fracture mechanics. It relies on Irwin's assumption [16] that the energy ΔE released by extending a crack with Δa is equal to the work required to close a crack by the same Δa. This assumption is used to compute the SERR at the crack front. When the computed value at a node exceeds the critical SERR, that node is released and the crack grows with Δa.

The first implementation of this assumption is a crack closure method in two analysis steps. In the first step, the reaction forces at the crack tip are calculated for a closed crack, using simple equilibrium equations. The second step then calculates the opening displacement of the node when the crack is extended with Δa [17].

This method is extended to the VCCT, which is based on the same assumption, with the additional notion that a crack extension from $a + \Delta a$ to $a + 2\Delta a$ has no significant influence on the state of the crack tip. This means that the energy to extend the crack tip from a to $a + \Delta a$ is the same as the energy to extend it from $a + 2\Delta a$ [17]. With this method, only one computational step is needed to calculate the SERR. Because the method relies on a self-similar delamination propagation, it needs previous knowledge on the location and the propagation of the crack front to be applicable. This means that damage initiation cannot be predicted with this method.

The equations to calculate the SERR are formulated by Raju [18]. The four-noded, two-dimensional element for which the equations are set up is shown in Figure 2.5.

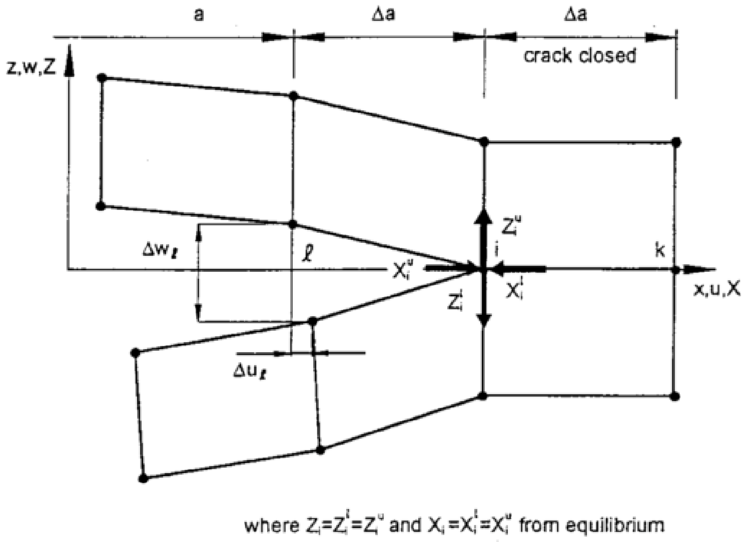

Figure 2.5: Virtual Crack Closure Technique (One-step crack closure technique) [17].

The SERR for opening modes I and II are calculated with the following equation. Note that mode III is not taken into account because we are considering a two-dimensional element.

$$\begin{aligned} G_I &= -\frac{1}{2\Delta a} Z_i (w_l - w_{l*}) \\ G_{II} &= -\frac{1}{2\Delta a} X_i (u_l - u_{l*}) \end{aligned} \tag{2.9}$$

Here X_i and Z_i are the nodal forces at node i in the x and z-direction respectively, w_l and u_l are the nodal displacements at the upper crack face (node l) and w_{l*} and u_{l*} are the nodal displacements at the lower crack face (node l*). Δa is the length of the elements at the crack front.

The total SERR is obtained by summing the results for the different modes:

$$G_T = G_I + G_{II} \tag{2.10}$$

This formulation assumes that there is orthogonality between the mesh and the crack front and that the elements before the crack front are the same size as the elements behind the crack front. Adaptations of this formulation have been made for different elements such as eight-noded elements or triangular elements.

2.2.2 Cohesive Zone Modelling (CZM)

When using CZM, cohesive elements are placed along the path where the crack is expected to grow. These cohesive elements are not standard linear elastic elements, but are governed by a Traction-Separation Law (TSL). This law relates the separation of the crack faces to the traction that opposes this separation. Several shapes of TSLs have been proposed [19].

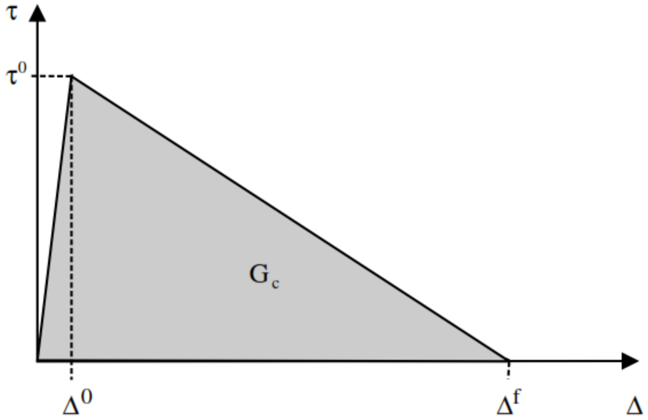

Figure 2.6: Bi-linear TSL as proposed by Turon et al. [12].

One of the more commonly used shapes is the bilinear law as proposed by Turon et al. [12], which is shown in Figure 2.6.

The equations to describe this bilinear TSL are described by Amiri-Rad and Mashayekhi [20]:

$$\begin{cases} \tau_i = K\lambda_i & \text{if } 0 \leq \lambda \leq \Delta^0 \\ \tau_i = (1-d)K\Delta^0 & \text{if } \Delta^0 \leq \lambda \leq \Delta^f \\ \tau_i = 0 & \text{if } \Delta^f \leq \lambda \end{cases} \tag{2.11}$$

where i is the identifier used for the different loading modes, therefore i is equal to 1,2 or 3. τ_i and λ_i are the components of the traction vector and the separation vector. For the cohesive elements a penalty stiffness, K is used, which represents the stiffness of the element. To combine different loading modes into one criterion, the variable λ is used. It is obtained from the displacement in the principal directions:

$$\lambda = \sqrt{\delta_1^2 + \delta_2^2 + \langle\delta_3\rangle^2} \tag{2.12}$$

The Macauley operator $\langle . \rangle$ means that negative values of δ_3 are omitted in Equation 2.12.

In Figure 2.6, the point of Δ^0 is the damage onset threshold. After the traction reaches the interface strength, there will be a decline in element stiffness and the traction will reduce for an increased separation. When the traction and stiffness are reduced to zero, at point Δ^f, complete failure is reached and the damage propagates to the next cohesive element. The decline in stiffness between damage onset and propagation can be characterized with a damage parameter, D, as seen in Equation 2.11. This damage parameter is dependent on the effective separation:

$$D = \frac{\Delta^f\,(\lambda - \Delta^0)}{\lambda\,(\Delta^f - \Delta^0)} \tag{2.13}$$

Since the energy release rate is defined as the total work per unit area, the critical energy release rate can be computed by integrating the traction-separation path:

$$G_c = \int_0^{\Delta^f} \tau(\delta)d\delta \tag{2.14}$$

In the case of mixed-mode loading conditions, a TSL is specified for each pure mode loading. To combine these into one TSL, which is defined by a combined penalty stiffness, and an onset and final displacement jump. These combined parameters are dependent on the mixed-mode ratio, which is defined as:

$$\beta = \frac{\Delta_{shear}}{\Delta_{shear} + \langle \Delta_3 \rangle} \tag{2.15}$$

To define the total critical SERR according to Equation 2.5, the ratio of $\frac{G_{shear}}{G_T}$ is needed. This ratio, B, is defined as [12]:

$$B = \frac{G_{shear}}{G_T} = \frac{\beta^2}{1 + 2\beta^2 - 2\beta} \tag{2.16}$$

Two important parameters for the successful implementation of a cohesive zone model into a FE analyses are the stiffness of the elements and the length of the cohesive zone.

Stiffness of the cohesive zone model

The stiffness of the cohesive elements should be carefully selected. If the contribution of the cohesive element to the global compliance is too large, a fictitious compliance is introduced to the model. Different guidelines have been proposed to select the stiffness of the interface. Turon et al. [21] have determined that the cohesive stiffness will not affect the properties of the composite if:

$$K = \frac{\alpha E_3}{t} \text{with } \alpha \gg 1. \tag{2.17}$$

In this equation E_3 is the Young's modulus through the thickness of the material and t is the thickness of an adjacent sub-laminate.

Cohesive zone length

The cohesive zone length is the distance between the crack tip and the point where the maximum cohesive traction is reached. To obtain sufficient accuracy of the CZM, there should be 3 to 5 elements present in this processing zone. Therefore it is important to have an accurate estimate of the cohesive zone length. When using a bi-linear TSL, this is equivalent to all the elements with a separation between Δ^0 and Δ^f. It is important to have an accurate estimation of the cohesive length since enough elements need to be present in the cohesive zone to obtain accurate results for the traction ahead of the crack tip [21]. In literature, different models have been proposed for the estimation of the cohesive zone length. In models that are governed by a TSL that prescribes zero traction for zero separation, predictions for the cohesive zone length have the form of[21]:

$$l_{cz} = ME\frac{G_c}{(\tau_0)^2} \tag{2.18}$$

where M is a parameter that depends on the specific cohesive model. In the most commonly used models, M is taken to be close or exactly equal to one [20]. For orthotropic materials with transverse isotropy where a plane strain condition can be assumed, the Young's modulus in Equation 2.18 is the transverse modulus E_2.

Advantages

The main advantage of CZM is that it is able to predict damage initiation as well as propagation. Therefore an initial crack is not necessary although it is still common practice to use an initial crack to reduce the computational cost [22]. Unlike other fracture modelling techniques,the method is also independent of the mesh and time step that are used in the model [23]. Another advantage is that it is a procedure with high flexibility which allows for the development of numerically stable models for crack extension [19]. Furthermore, there is no need to remesh the structure after each step of crack growth [20, 24].

Limitations

Like any numerical method, CZM also has some limitations. There is a possibility that artificial compliance is introduced into the model [25]. This artificial compliance is inversely proportional to element size, so a user has to be careful when performing a mesh convergence, as refining the mesh might not always result in a more accurate representation. Another limitation is that the cohesive zone requires 3 to 5 elements to be able to accurately predict damage evolution. This means that the mesh needs to be rather fine in order to capture all the effects, so a lot of elements and nodes are needed. This can lead to high computation times. Lastly, the computational implementation of the technique requires an array of double nodes between plies to accommodate for the cohesive elements. This increases the number of degrees of freedom in the system and can have a negative effect on the computational time [26].

2.3 Fatigue in Cohesive Zone Modelling

Different authors have developed methods to incorporate fatigue behaviour into the cohesive zone model that was described previously. These models are based on two different approaches to take the cyclic loading into account; either an envelope approach or a loading-unloading hysteresis model is used. Most models use the bi-linear TSL as this is researched extensively for static behaviour. To ensure irreversibility, the models use an unloading and reloading criterion that follows the cohesive law. To keep track of this irreversibility, internal variables are used in the reloading criterion. Examples of these variables are the unloading stiffness [27, 28], damage variables which degrade the onset traction [29] or the initial stiffness of the undamaged cohesive law [30–32]. The fatigue models are all based on a quasi-static model, where an additional formulation is proposed for the development of the internal variables with the number of cycles.

2.3.1 Envelope load models vs loading-unloading hysteresis damage models

The envelope approach to fatigue modelling means that only the maximum load is taken into account. The cyclic variations of the load are accounted for by using the load ratio [33]. The evolution of the analysis is expressed in terms of the number of cycles, N, which is used as pseudo-time. This means that it is also a continuous and differentiable variable. Envelope load models are characterised by the damage rate dD/dN. Mostly the damage is split in two terms according to Equation 2.19.

$$D_{tot} = D_s + D_f \tag{2.19}$$

The part that is related to the fatigue damage, D_f, and the part that is due to the quasi-static damage, D_s, which develops according to the TSL specific to the chosen model [33].

Loading-unloading hysteresis damage models on the other hand, simulate each cycle in a fatigue analysis. These models simulate the cyclic development of the damage by applying a change in the interfacial constitutive stiffness during each cycle. The advantage of these models is that every cycle is completely modelled, which makes more detailed analyses possible. When using this type of models, the user needs to be careful as they can become computationally expensive. Most loading-unloading hysteresis models use an expression for the change in interfacial constitutive stiffness that depends on whether the interfacial separation is increasing or decreasing [33].

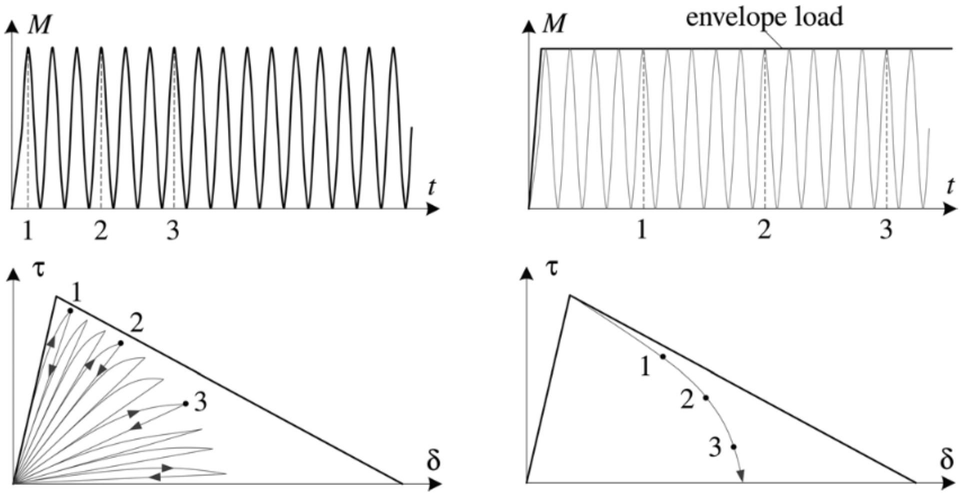

Figure 2.7: Example of the TSL for an loading-unloading hysteresis model (left) and for an envelope load model (right) [33]

For applications in the aerospace industry, the envelope approach is more widely used since it can cut down the computational time significantly compared to the loading-unloading hysteresis models. The difference in the models that apply this strategy is the way in which they obtain the change in the damage parameter per cycle.

2.3.2 Combined initiation and propagation model

May and Hallet note that a cycle-by-cycle law is not suitable for high cycle fatigue analysis since it would require more computational power, thus a hysteresis model is used [34].

The developed model does not need a pre-existing crack in order to model the material behaviour, instead the cycles until onset of damage are calculating by using the ratio of the applied stress to the material failure stress. The onset location is determined by calculating a failure index for every element which based on the strain energy release rate.

Once the number of cycles to initiate damage is calculated, the damage propagation process can be modelled. Harper and Hallet use a loading envelope strategy because this is better suited for high cycle fatigue [35]. Most damage propagation laws for cohesive elements are based on the Paris relation that was explained in Chapter 2.1.

Another characteristic that is needed for damage propagation is the strain energy release rate. For fatigue loading, the strain energy release rate changes within each cycle. The change in strain energy release rate can be expressed using the maximum strain energy release rate, G_{max}, and the stress ratio, R:

$$\Delta G = G_{max} \cdot (1 - R^2) \tag{2.20}$$

As described in section 2.2.2, it is important to have an accurate simulation of the cohesive zone length. The damage zone length for fatigue loading can be expressed in terms of the cohesive zone length in a static loading case [35].

$$l_{fat} = \frac{1}{2} \cdot \frac{G_{max}}{G_C} \cdot l_{CZf} \tag{2.21}$$

Note that the static cohesive zone length is a required user input that should be obtained from previous static tests.

For the propagation model, the damage parameter is dependent on the static damage parameter $D = \frac{\delta - \delta_0}{\delta_{max} - \delta_0}$. Because the cohesive elements have no knowledge of their location in the cohesive zone, the accumulation of some fatigue damage in the quasi-static region cannot be avoided. This causes the actual TSL to differ from the bi-linear TSL with no fatigue damage. This deviation can be seen in the bottom right of Figure 2.7. This unwanted fatigue damage, D_{fu}, has to be accounted for. A way to compute this parameter is presented by Harper and Hallet [35]. The fatigue damage parameter is computed by:

$$\frac{\delta D_{fp}}{\delta N} = \frac{1 - D - D_{fu}}{l_{fat}} \frac{da}{dN} \tag{2.22}$$

The total damage is a combination of the fatigue damage and the quasi-static damage: $D_{tot} = D + D_{fp}$. The total damage is accumulated from zero, when there is no damage, to one, when the element fails and all the element stresses are reduced to zero.

Damage onset location

Using the assumption that no imperfections are present in the structure, the damage initiation will be in a location with a local stress concentration such as ply drops, holes and curvature. In a standard linear-elastic analysis, the element that fails first will be the one with the highest stress. However, May and Hallet use cohesive elements with a bilinear TSL [36], the material shows a softening behaviour. This means that a different failure criterion is needed. A more suitable way to determine the onset location is using a Failure Index, which is based on the strain energy release rate. To calculate the Failure Index, the maximum load in the interface element under mixed-mode conditions, σ_m and the maximum mixed-mode displacement, δ_m^f are used:

$$FI = \frac{G_m}{G_{mc}} \quad \text{with} \quad G_{mc} = \frac{1}{2}\sigma_m \delta_m^f \tag{2.23}$$

The model also includes a set of damage initiation laws that will be applied to the element with the highest Failure Index (FI) and the surrounding elements. These initiation laws are based on the severity, which is defined as the ratio of the applied cyclic stress to the static failure stress [36]. The zone of the element with the highest FI and its surrounding elements is called the initiation zone. The radius of the initiation zone is an empirical input parameter. The elements outside the initiation zone only accumulate propagation damage according to the Paris relation.

The results of the initiation criterion are promising, the cycles until failure have shown good correspondence with available experimental data [36]. However, it has also been found that the parameters of the initiation criterion, the severity and the radius of the initiation zone, have a significant influence on the following propagation behaviour. This can cause problems in the use of the model since the radius is a mostly empirical parameter and severity can be difficult to accurately extract from the analysis [34]. Furthermore, static analyses are always necessary beforehand in order to determine the static failure stress that is needed to calculate the severity.

The propagation model was also tested separately from the initiation model, with some difficulties as well. The three point bending simulations resulted in the model predicting an infinite fatigue life, which is contradictory to the expectations [34]. The addition of the initiation criterion, results in a finite fatigue life, so the issues of the propagation model on itself are solved.

2.3.3 Non-local propagation model

Turon et al [30] developed a cohesive zone model for high cycle fatigue that combines fracture and damage mechanics. This results a formulation for the evolution of the damage variable in terms of the crack growth rate, $^{da}/_{dN}$. The model is called a non-local model because the damage in one integration point depends on the damage of other points in the model. This dependency is caused by the fact that the damage parameter is calculated based on the SERR and the cohesive zone length. These are both global parameters. The constitutive model is based on a previous model for quasi-static loading developed by the same authors [12].

The constitutive model for high-cycle fatigue is based on the Paris relation that is described in chapter 2.1. The parameter that is used in this model is the damage variable which depend on the damage initiation and propagation which were described in the quasi-static model. The evolution of this damage variable can be described as [30]:

$$\frac{\partial D}{\partial N} = \frac{1}{l_{CZ}} \frac{\left(\Delta^f(1-D) + D\Delta^0\right)^2}{\Delta^f \Delta^0} \frac{da}{dN} \tag{2.24}$$

In this expression, the initiation criterion, Δ^0, and the propagation criterion, Δ^f are obtained from the previously discussed quasi-static constitutive model by Turon et al.[12]. The term A_{cz} refers to the area of the cohesive zone. When this equation is used for a 2D analysis, it should be replaced with l_{cz}, the length of the cohesive zone. The last term in this expression is simply the crack growth rate defined by the Paris law. Instead of the parameter ΔK, Turon et al. use the change in strain energy release rate $^{\Delta G}/_{G_c}$. This is slightly different from Equation 2.7, which means that the coefficients have different values. The parameters C, m and G_{th} are dependent on the mode ratio. For C and m, the definition by Blanco et al. [37] is used. To determine the mixed-mode strain energy release rate an expression is used that is similar to the one introduced by Benzegaggh and Kenane [11].

When the analysis involves high-cycle fatigue, calculating every cycle is computationally exhaustive process. The cycle jump strategy is implemented where the computations are done for a set of loading cycles at a time, thus reducing the computational resources that are required. The number of loading cycles that are included in the computation depend on the maximum increase in the damage variable that is allowed to occur. This parameter is set by the user as an input, Turon suggests setting this to 0.001 [30].

This model by Turon et al. [30] was validated with different tests including a simulation of mixed-mode loading where experimental results and computational results were compared to a Paris law curve fit. It was seen that the predicted data for small values of the energy release rate from the applied moment was slightly higher than the experimental data. Furthermore, the model was able to approximate the Paris relation growth rate without any further adjustment parameters. The cohesive zone length estimation in this model is based on pure mode I loading, therefore the results are more accurate when mode I loading is dominant. This can cause inaccuracies when the model is used for mixed-mode loading cases, however the length of the cohesive zone can be adapted based on preliminary results.

2.3.4 Geometry independent model

Ami-Rad and Mashayekhi [20] developed a model for fatigue-driven delamination analysis also based on the quasi-static-constitutive model by Turon et al. [12]. This model is not dependent on the cohesive zone length for the calculation of the change in damage parameter per cycle. The authors make the assumption that the cohesive zone ahead of the crack tip is moving at a rate of $^{da}/_{dN}$. This leads to an expression for the change in damage parameter with respect to the cycles.

$$\frac{\partial D}{\partial N} = \frac{\Delta^f \Delta^0}{\delta^2(\Delta^f - \Delta^0)} \frac{\partial \delta}{\partial x} \frac{da}{dN} \tag{2.25}$$

The first fraction in this equation is the equation for the damage parameter, equation 2.13 derived with respect to the separation. The two other fractions are partial derivatives to relate the speed of the tip of the crack front to the speed of the front of the partially damaged cohesive zone. The parameters for the Paris law for the mixed-mode loading are computed in the same way as Turon et al. [30].

The model has been validated with the use of several benchmark cases in mode I, II and mixed-mode loading conditions and shows promising results. However, all these cases were only tested in 2D models. The authors mention that the method can be easily expanded to 3D cases, but this has yet to be demonstrated [20].

2.3.5 Adaptive element splitting technique

In composite structures, it is often difficult to predict where the crack path or the delamination path will form as there are many interface surfaces between plies. When using the standard cohesive zone method, the user would need to apply cohesive elements along all the plausible crack paths. However, adding cohesive elements on too many interfaces within a structure would result in an unwanted artificial compliance [25].

Shor and Vaziri developed a method for adaptive insertion of cohesive elements called the Local Cohesive Zone (LCZ) methodology [38]. The premise of this technique is that in the zones away from the crack tip, it is not necessary to have cohesive elements during the whole analysis. The cohesive elements are introduced locally around the crack tip when they are needed in the analysis. This means that the elements that are fully delaminated and the ones that are undamaged are thick shell elements or solid elements which are split into a cohesive element between two shell elements when the element falls within a predefined radius R of the crack tip. Once an element is fully delaminated, the cohesive element is deleted. The LCZ program is not a FEM solver, instead the structural problem is solved using LS-DYNA and the LCZ performs the specific operations such as the element splitting and the introduction of new elements.

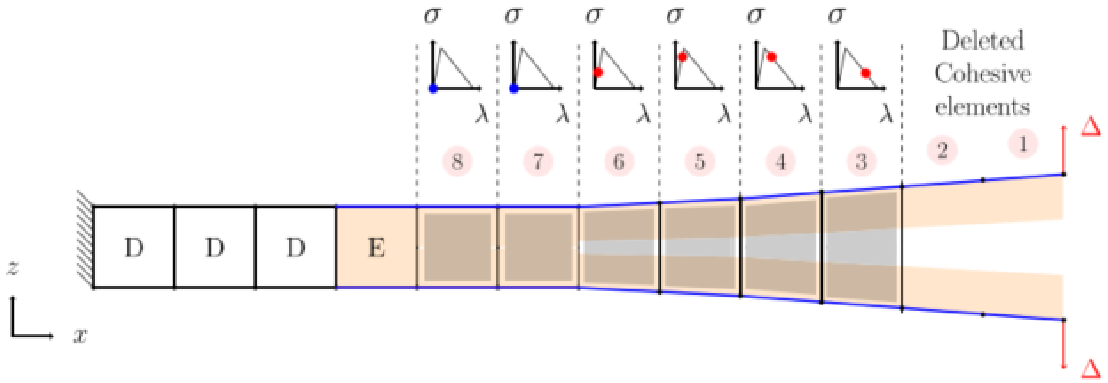

Figure 2.8: Part of the element splitting algorithm by Shor and Vaziri [38].

The model is verified using a DCB specimen that is modelled with the traditional cohesive element formulation and one that is modelled with the LCZ model. The force-displacement curve and the overall energy balance were compared to other numerical and analytical models. The results were in good agreement, however due to the fact that the LCZ module is not a built in feature of LS-DYNA, some computational noise is created. The authors further developed this model for the use of impact damage modelling [39]. Other modelling issues include the compatibility between the existing shell elements and the inserted cohesive elements due to a difference in available degrees of freedom. Similar issues are to be expected when implementing the method in Abaqus [40]. Furthermore, numerical issues regarding the scalability and the computational efficiency are posed by the authors [38].

2.3.6 S-N based local approach

The models that were previously discussed are based on the Paris relation that was discussed in Chapter 2.1. This poses difficulties since all these methods are local methods that rely on the state of the processing zone, but the Paris relation is a non-local relation, so using it in a local formulation can cause inaccuracies. The work of Dávila [41] presents a purely local method for damage propagation. This means that the method is only relying on the loading history and damage accumulation of a point to determine the damage propagation at said point.

The foundation of the model is a bilinear traction separation law, where the stiffness degradation, $(1-d)$, can be calculated as follows:

$$(1-D)=\frac{\lambda^{*}-\Delta^{f}D}{\lambda^{*}} \tag{2.26}$$

where D is the damage norm, $\frac{\lambda}{\lambda^{*}}$ is the relative displacement jump at any point P. These parameters are defined as:

$$D=\frac{\lambda^{*}-\Delta^{0}}{\Delta^{f}-\Delta^{0}} \text{ and } \frac{\lambda}{\lambda^{*}}=\frac{\sigma^{max}}{(1-D)\sigma_{c}} \tag{2.27}$$

where σ^{c} is the material strength and σ^{max} is the maximal applied stress. For the damage accumulation, the following equation is proposed:

$$\frac{dD}{dN}=(D+\gamma)\left(\frac{\lambda}{\lambda^{*}}\right)^{\beta} \tag{2.28}$$

The two parameters, γ and β, are heuristic parameters that can be found by solving a set of non-linear equations or by matching the response of the model to experimental data for the S-N curve.

The model was found to be capable of predicting failure in unnotched specimens, in cases where the physics are dominated by the S-N diagram. It was also found to be able to predict crack propagation in cases where the Paris relation would originally be applied. However, the model was only validated for DCB and MMB specimens with one specific composite material, so additional validation is necessary to make definite conclusions about the accuracy of the model.

Chapter 3

Research Objective and Questions

This chapter contains the research objective and corresponding research questions that define the scope of the research project. These are based on an analysis of the literature review.

3.1 Research Objective

The research objective is defined as:

To implement cohesive zone modelling in the finite element fatigue analysis of coupon level composite structures by using a non-local propagation model.

The main advantages of CZM over VCCT are that the need for remeshing along a predefined crack path is avoided when it is used as a predictive model [24]. In CZM, the elements are placed along the paths where cracks are expected before the analysis is started. Furthermore, CZM is capable of including the damage onset phase into an analysis. Other methods are only capable of analysing the damage propagation. Since most CZM rely on fracture mechanics formulations to predict the crack growth rate, it suffers from the same shortcomings as these formulations. The main drawback of the fracture mechanics formulations is that there is a lack of understanding the physics of the fracture process. Thus, the models are based on previous experience and curve-fitted data [24].

The non-local propagation model is developed by Turon et al [30] and is based on a quasi-static model by the same authors [21]. Both models will be implemented in a numerical analysis.

The quasi-static model was developed, primarily to allow the use of larger mesh sizes compared to previously developed CZM. This is beneficial in large-scale analyses because it reduces computational time. There are two parameters that have a big influence on the success of a FE simulation using CZM [42]. Firstly, the interface stiffness should be large enough so that the contribution of the cohesive zone to global compliance is negligible. Secondly, the element size should be smaller than the cohesive zone length. To select these parameters, Turon et al. [21] presented two guidelines. This approach is unique because it is based on mechanical aspects, not dependent on previous experiences. To enable the use of coarser meshes, the interface stiffness is decreased to allow a larger cohesive zone. This does, however, result in a less accurate representation of stress concentrations near the crack tip.

The non-local propagation model by Turon et al. is capable of predicting fatigue crack growth without model-specific curve-fitting parameters [30]. The model links fracture mechanics and damage mechanics by deriving the computation of the damage evolution from a fracture mechanics description. This makes it possible to consider loading conditions such as load ratio, SERR and mode mixity to determine the damage accumulation.

To verify and validate the prediction of fatigue crack growth by the implemented non-local propagation model, the results of the analysis will be compared to different benchmark results from literature.

3.2 Research Questions

To achieve the research objective, the following research question is put forward.

- Is it possible to implement the fatigue model by Turon et al into a User Material (UMAT) for Abaqus?
    - What adaptations are necessary for the implementation?
    - What is the performance of the model compared to a numerical benchmark?
    - What is the achievable accuracy when compared to experimental data?
    - What type of coupon tests can be used to test the performance of the implementation?

Chapter 4

Methodology

This chapter describes the methodology followed for this research project. This consists of a theoretical model, its implementation into a UMAT routine for Abaqus and the validation of the developed subroutine.

The theoretical model chosen is developed by Turon et al. The model was briefly mentioned in Chapter 2. In this chapter it is explained in more detail. The static model is shown first, secondly the expansion to a model for the analysis of fatigue behaviour is explained. Both models are taken from literature.
Thereafter, the UMAT routine is discussed. This routine was developed during this project to implement the theoretical model into Abaqus for the fatigue analysis of composite structures at coupon level.
Finally, the verification and validation strategies for the UMAT routine are presented. This consists of a series of benchmark tests and a set of analytical calculations based on LEFM that are taken from literature.

4.1 Theoretical Model

This section contains a detailed description of both models for the analysis of the static response and the fatigue response. The constitutive model is based on a bi-linear Traction-Separation Law (TSL) for the element degradation.

4.1.1 Static model

The theoretical model that is used for the analysis of the static response was developed by Turon et al. [43]. The model uses a bi-linear TSL. A representation of this TSL with the parameters is shown in Figure 4.1.

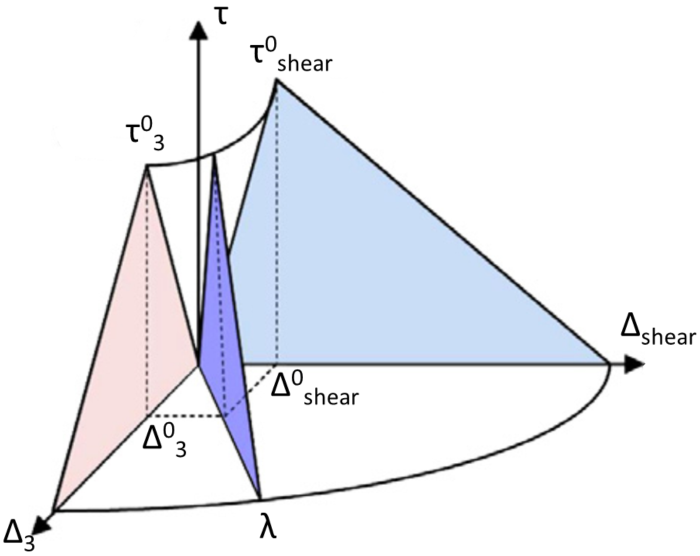

Figure 4.1: A 3D bi-linear TSL (adapted from [34])

The main parameter in the model is the displacement jump tensor, λ, which is used to compare different states of the displacement. The displacement jump tensor is always positive and continuous and is defined as:

$$\lambda = \sqrt{\langle\Delta_3\rangle^2 + (\Delta_{shear})^2} \tag{4.1}$$

where Δ_3 is the separation in mode I and $\Delta_{shear} = \sqrt{(\Delta_1)^2 + (\Delta_2)^2}$, the Euclidian norm of the separations in modes II and III. The Macauley operator is used with Δ_3 to omit negative values. When Δ_3 is smaller than zero, there is a compressive mode I loading. It is assumed that a compressive loading does not result in any damage. The model uses a bilinear TSL, so two important parameters are the onset displacement jump, Δ^0, and the final displacement jump, Δ^f. First, the onset displacement jump is calculated for each opening mode:

$$\Delta_i^0 = \frac{\tau_i^0}{K} \qquad i = 3, shear \tag{4.2}$$

where τ_i^0 are the interfacial strengths for each opening mode and K is the interface stiffness. In the case of mixed-mode loading, there are two parameters β and B to characterise the mode-mixity, where β is the ratio of the shear opening separation to the total separation and B is the ratio of the strain energy release rate for the shear opening modes, G_{shear} to the total strain energy release rate, G_{tot}. These parameters are calculated by: [12]

$$\beta = \frac{\Delta_{shear}}{\langle\Delta_3\rangle + \Delta_{shear}} \tag{4.3}$$

$$B = \frac{G_{shear}}{G_T} = \frac{\beta^2}{1 + 2\beta^2 - 2\beta} \tag{4.4}$$

The mixed-mode SERR is calculated using the Benzeggagh-Kenane criterion [11].

$$G_{TC} = G_{IC} + (G_{IIC} - G_{IC})[B]^\eta \tag{4.5}$$

where η is a semi-empirical coefficient and $G_T = G_I + G_{II}$.

With the mixed-mode ratios known, the mixed-mode onset and final displacement jumps can be calculated as a combination of the pure displacement jumps, the strain energy release rates and B:

$$\Delta^0 = \sqrt{\langle \Delta_3^0 \rangle^2 + \left[(\Delta_{shear}^0)^2 - (\Delta_3^0)^2 \right] [B]^\eta} \tag{4.6}$$

$$\Delta^f = \frac{2}{K\Delta^0} \left[G_{Ic} + (G_{IIc} - G_{Ic}) [B]^\eta \right] \tag{4.7}$$

A second important parameter to define is the damage threshold. This parameter is used to test whether the displacement jump is large enough to result in damage in the model. The onset and final displacement jumps are used to determine the damage threshold at the current time step, r^t, and the damage threshold at the next step is the maximum of the current damage threshold and the displacement jump norm that is calculated with Equation 4.1:

$$r^t = \frac{\Delta^0 \Delta^f}{\Delta^f - d^t \left[\Delta^f - \Delta^0 \right]} \tag{4.8}$$

$$r^{t+1} = \max\{r^t, \lambda\} \tag{4.9}$$

With the damage threshold and the displacement jumps, the damage, D, at the next time step is calculated:

$$D^{t+1} = \frac{\Delta^f \left(r^{t+1} - \Delta^0 \right)}{r^{t+1} \left(\Delta^f - \Delta^0 \right)} \tag{4.10}$$

From this equation, if the displacement jump tensor does not exceed the damage threshold, the damage at the next time step will be the same as the damage at the current time step. Once the damage at the next time step is known, the stiffness loss in the element is known, so the traction in the element is calculated:

$$\tau_i = D_{ij}\Delta_j = \bar{\delta}_{ij} K \left[1 - D \left(1 + \bar{\delta}_{3j} \frac{\langle -\Delta_j \rangle}{\Delta_j} \right) \right] \tag{4.11}$$

In the case where Δ_3 is bigger than zero, this extensive tensor notation can be simplified to:

$$\begin{bmatrix} \tau_3 \\ \tau_{shear} \end{bmatrix} = \begin{bmatrix} K\left(1 - D^{t+1}\right) & 0 \\ 0 & K\left(1 - D^{t+1}\right) \end{bmatrix} \begin{bmatrix} \Delta_3 \\ \Delta_{shear} \end{bmatrix} \tag{4.12}$$

The term D_{ij} in Equation 4.11 is the secant stiffness. However, for further calculations, the tangent stiffness D_{ij}^{tan} is needed so that Abaqus can calculate the strain increments for the next time step. This can be calculated with:

$$D_{ij}^{tan} = \begin{cases} \left(D_{ij} - K \left[1 + \bar{\delta}_{3j} \frac{\langle -\Delta_j \rangle}{\Delta_j} \right] \left[1 + \bar{\delta}_{3j} \frac{\langle -\Delta_j \rangle}{\Delta_j} \right] \frac{\Delta^f \Delta^0}{\Delta^f - \Delta^0} \frac{1}{\lambda^3} \Delta_i \Delta_j \right) & \text{for } r^t < \lambda < \Delta^f \\ D_{ij} & \text{for } r^t > \lambda \text{ or } \Delta^f < \lambda \end{cases} \tag{4.13}$$

If the displacement jump tensor is between the damage threshold and the final displacement jump, the secant stiffness is reduced by a multiple of the interfacial stiffness. However, if the displacement jump tensor is not within this interval, the secant stiffness is not reduced.

4.1.2 Fatigue model

This section describes the model for fatigue analysis by Turon et al [30]. It is based on the static model from the previous section. The fatigue model is based on the premise that the static damage and the fatigue damage can be calculated separately from each other. The static part of the damage is calculated with the equations from the previous section. The fatigue damage is calculated with the procedure in this section and the two are added to obtain the total damage.

This model is based on linking the evolution of the damage variable to the crack growth rate ${}^{da}\!/_{dN}$. This link is made with the equation:

$$\frac{\partial D}{\partial N} = \frac{\partial D}{\partial l_d}\frac{\partial l_d}{\partial N} \tag{4.14}$$

where l_d is the length of the damaged area and $\partial l_d/\partial N$ is the growth rate of length of the damaged area. The last term is a material property that can be related to the Paris relation with:

$$\frac{\partial l_d}{\partial N} = \frac{l^e}{l_{CZ}}\frac{da}{dN} \tag{4.15}$$

l_{CZ}/l^e is the ratio that represents the number of elements in the cohesive zone. By stating that the ratio between the damaged area with respect to the element size is equal to the ratio of the dissipated energy over the fracture toughness, Turon et al. come to an equation for the ratio between the damaged area with respect to the element size:

$$\frac{l_d}{l^e} = \frac{d\Delta^0}{\Delta^f(1-d) + d\Delta^0} \tag{4.16}$$

By combining Equations 4.14, 4.15 and 4.16, the following equation is obtained:

$$\frac{\partial D}{\partial N} = \frac{1}{l_{cz}}\frac{\left(\Delta^f(1-d) + d\Delta^0\right)^2}{\Delta^f\Delta^0}\frac{da}{dN} \tag{4.17}$$

Here, l_{cz} is the length of the cohesive zone. For pure mode I, this parameter is calculated with:

$$l_{cz} = \frac{9\pi}{32}\frac{E_3 G^{max}}{(\tau^0)^2} \tag{4.18}$$

where E_3 is the Young's modulus of the material in the normal direction, τ^0 is the interface strength in mode I opening and G_{max} is the maximum strain energy release rate in the loading cycle. The parameter $\frac{9\pi}{32}$ is a fitting parameter that can be modified when required. Different authors have determined different parameters to be used in the calculation of the area [21].

From Equation 4.17 it can be seen that the evolution of the damage variable is dependent on the damage, D, in the previous loading cycle, the characteristics of the TSL used by the model, Δ^0 and Δ^f, the size of the cohesive zone, l_{cz}, and the crack growth rate ${}^{da}\!/_{dN}$. The crack growth rate is dependent on the loading and material properties. It has been defined by Paris [13] as:

$${}^{da}\!/_{dN} = CG_{max}^m \text{ if } G_{th} < G_{max} < G_C \tag{4.19}$$

If the strain energy release rate is below the threshold, G_{th}, the loading is not high enough to cause any crack growth. However, when the strain energy release rate is higher than the critical strain energy release rate, G_C, the crack growth rate is unstable, it no longer follows Equation 2.7 and catastrophic failure occurs.

The maximal strain energy release rate, G_{max}, and the variation of the strain energy release rate, ΔG are found by computing the area under the TSL as can be seen in Figure 4.2.

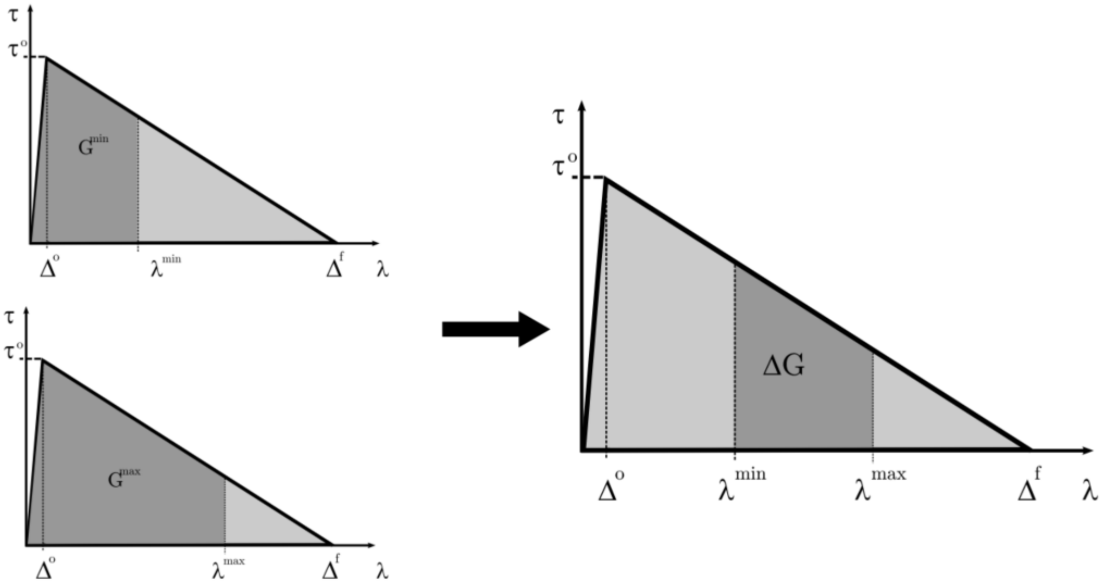

Figure 4.2: Variation of the strain energy release rate [30].

So for G_{max}, the area under the TSL is:

$$G_{max} = \frac{\tau^0}{2} \left[\Delta^f - \frac{\left(\Delta^f - \lambda_{max}\right)^2}{\Delta^f - \Delta^0} \right] \tag{4.20}$$

where λ_{max} is the maximum displacement jump during the loading cycle. In the case of mixed-mode loading, the threshold and critical strain energy release rates should be calculated using the Benzegagh-Kenane mixed-mode loading criterion [11].

Turon et al. chose to implement a cycle jump strategy into the model since a cycle by cycle strategy would be too tedious when the process involves high-cycle fatigue. This cycle jump strategy is based on the one presented by Van Paepegem and Degrieck [44].

So the damage variable at integration point J, at time step $i + \Delta N_i$ is calculated with:

$$D^J_{i+\Delta N_i} = D^J_i + \frac{\partial D^J_i}{\partial N} \Delta N_i \tag{4.21}$$

where D^J_i is the damage variable at time step i, $\frac{\partial D^J_i}{\partial N}$ is the damage growth rate at the same time step and ΔN_i is the number of cycles that is skipped to the next time step. The accuracy of the results will be dependent on the number of cycles ΔN_i that can be skipped.

To determine this number, the maximum damage increase is chosen by the user from which the number of jumped cycles is calculated:

$$\Delta N_i = \frac{\Delta D_{max}}{\max\limits_{j} \left\{ \frac{\partial D_i^J}{\partial N} \right\}} \tag{4.22}$$

When Δd_{max} is increased, the accuracy of the analysis will be decreased, but the analysis will be faster.

Finally, after all the calculations above are performed, the total damage can be calculated:

$$D_{tot} = D_{stat} + D_{i+\Delta N_i}^J \tag{4.23}$$

Once the damage parameter is known, Equations 4.11 and 4.13 are calculated.

4.1.3 Modifications for fatigue model

For the analyses of loading cases where multiple opening modes are present, some adaptations were necessary to the fatigue model. The modifications are needed to include a formulation for a mode-dependent penalty stiffness and a mode-dependent cohesive zone length.

Mode-dependent penalty stiffness

The first modification is the inclusion of a mode-dependent penalty stiffness as proposed by Turon et al.[45]. It was developed to deal with changes in the local mixed-mode ratio. The formulation for the shear mode penalty stiffness, K_{sh} is:

$$\frac{K_{sh}}{K_3} = \frac{G_{Ic}}{G_{IIc}} \left(\frac{\tau_{sh}^0}{\tau_3^0} \right)^2 \tag{4.24}$$

where τ_{sh}^0 and τ_3^0 are the interlaminar strengths for the shear mode and mode I, G_{Ic} and G_{IIc} are the pure-mode SERR and K_3 is the penalty stiffness for mode I.

With the shear mode penalty stiffness known, the mode-dependent penalty stiffness is defined as:

$$K_B = K_3(1 - B) + BK_{sh} \tag{4.25}$$

where B is the local mixed-mode ratio, that is computed with:

$$B = \frac{K_{sh}\Delta_{sh}^2}{K_{sh}\Delta_{sh}^2 + K_3 \langle \Delta_3 \rangle^2} \tag{4.26}$$

Δ_{sh} is the shear interface separation that is calculated in the same way as the original model.

The mixed-mode equivalent displacement jump is calculated with:

$$\lambda = \frac{K_{sh}\Delta_{sh}^2 + K_3 \langle \Delta_3 \rangle^2}{\sqrt{K_{sh}^2\Delta_{sh}^2 + K_3^2 \langle \Delta_3 \rangle^2}} \tag{4.27}$$

The mixed-mode onset displacement jump is obtained from the following equation:

$$\lambda^0 = \sqrt{\frac{K_3(\Delta_3)^2 + K_{sh}(\Delta_{sh}^0)^2 - K_3(\Delta_3^0)^2]B^\eta}{K_B}} \tag{4.28}$$

The mixed mode critical displacement jump reads:

$$\lambda^c = \frac{K_3\Delta_3^0\Delta_3^c + [K_{sh}\Delta_{sh}^0\Delta_{sh}^c - K_3\Delta_3^0\Delta_3^c]B^\eta}{K_B\lambda^0} \tag{4.29}$$

These new calculations for the penalty stiffness and the different displacement jumps replace the equations for these parameters in the original model.

Mode-dependent cohesive zone length

The second modification is to include a formulation for a mode-dependent cohesive zone length. The determination of the cohesive zone length in the original model is based on material parameters for mode I. In the case of mixed-mode loading, this is adapted to include parameters for mode II for a more accurate computation of the cohesive zone length. This formulation was proposed by Turon et al. [46].

Firstly, the mixed-mode Young's modulus, E_m, needs to be determined:

$$E_m = E_I(1 - B) + E_{II}B \tag{4.30}$$

where B is the mixed-mode ratio and E_I and E_{II} are the equivalent Young's moduli for the separate modes. These are determined with:

$$E_I = \left(\frac{E_{22}}{Q}\right)\ , E_{II} = \frac{E_{22}}{Q}\left(\frac{E_{11}}{E_{22}}\right)^{\frac{1}{2}} \tag{4.31}$$

where:

$$Q = \frac{1}{2}\sqrt{2\left[\left(\frac{E_{22}}{E_{11}}\right)^{\frac{1}{2}} - \nu_{21}\right] + \frac{E_{22}}{G_{12}}} \tag{4.32}$$

With the mixed-mode Young's modulus, a new cohesive zone length can be calculated:

$$l_{CZ} = ME_m\frac{G_c}{(\tau^0)^2} \tag{4.33}$$

where M is a constant parameter that was discussed in the original model, G_c is the mixed-mode fracture toughness that can be calculated from the pure mode values with the Benzegaggh-Kenane criterion [11] and τ^0 is the mixed-mode interlaminar strength that is calculated with:

$$(\tau^0)^2 = (\tau_3^0)^2 + \left[(\tau_{shear}^0)^2 - (\tau_3^0)^2\right]B^\eta \tag{4.34}$$

When the mode-dependent penalty stiffness and cohesive zone length are implemented into the original model, a more accurate representation of the behaviour under mixed-mode loading conditions can be achieved.

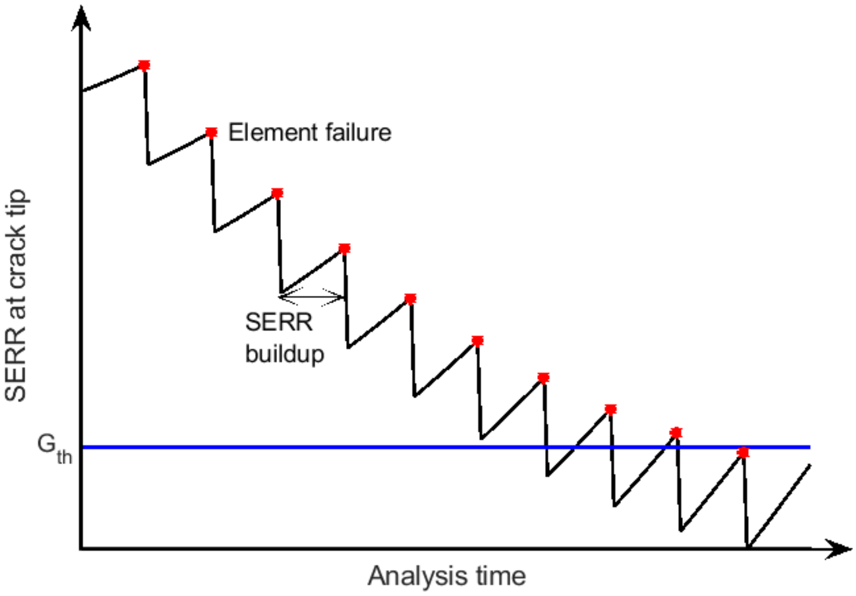

Figure 4.3: Hypothetical plot of the SERR at the crack tip as the analysis progresses.

Fluctuating SERR

Due to the discrete nature of a finite element analysis the SERR at the crack tip shows a fluctuating pattern such as Figure 4.3.

The SERR in the element at the crack tip builds up until this element fails. At this instance, the next element becomes the crack tip. This element has a lower SERR thus the crack tip SERR suddenly drops until that element fails. This pattern continues through the analysis.

To compare the SERR to the threshold value, the value before element failure should be used and not the value right after element failure.

Mixed-mode SERR

The local SERR in each element is calculated with the area under the TSL from the element state. When a specimen is subjected to a pure mode loading condition, this value corresponds to the global SERR which is used in the Paris relation. However, under mixed-mode loading conditions, the mode-mixity changes over the length of the processing zone. As a result of this, the local SERR is different from the global ratio. This causes difficulties when determining whether the loading is in the crack propagation region of the Paris relation. To circumvent this issue, the global SERR is calculated from the specimen compliance with a set of analytical equations based on LEFM these equations are explained in detail in Section 4.3.2.

4.2 User Subroutine

Abaqus [40] is a commercial software for finite element analysis of a wide range of structural problems. It contains a wide range of element types which all have a different constitutive model. Abaqus also provides the option of adding user subroutines to adapt the analysis to specific needs. In this project, a User Material (UMAT) subroutine is developed to include a new constitutive model. All subroutines must be written in Fortran so that Abaqus can compile the code to use in the analysis.

A UMAT routine is called during every iteration of the analysis at each integration point. The inputs of a UMAT routine are the stresses and strains at the start of the iteration and the strain increments. The material properties are defined before the start of the analysis. They do not change over the course of the analysis. The output of the routine are the stress increments and the tangent stiffness tensor. These outputs are used by Abaqus to compute the inputs for the next iteration.

This section describes the two UMAT routines that were written based on the theoretical models from Sections 4.1.1 and 4.1.2.

4.2.1 User Material routine for static loading

The flow of one increment of the subroutine can be seen in Figure 4.4. The material properties for this analysis are the critical SERR for the different opening modes, the material stiffness, the interfacial strengths and η, the exponent of the relationship for mixed-mode strain energy release rate by Benzegagh and Kenane [11]. The equations used in the subroutine were written as presented by Turon et al. [21]. *Input* 1, the material properties are the input at the start of the analysis, these parameters do not change during the analysis. *Input* 2 is the separations and the damage variable at the start of the current increment. The damage variable is an immediate output of the previous increment and the separations are calculated with the tangent stiffness tensor that is an output of the previous increment. The values for *Input* 2 are not constant during the analysis and are different for each increment and each element.

The complete code for one increment of the subroutine is shown in Appendix A.

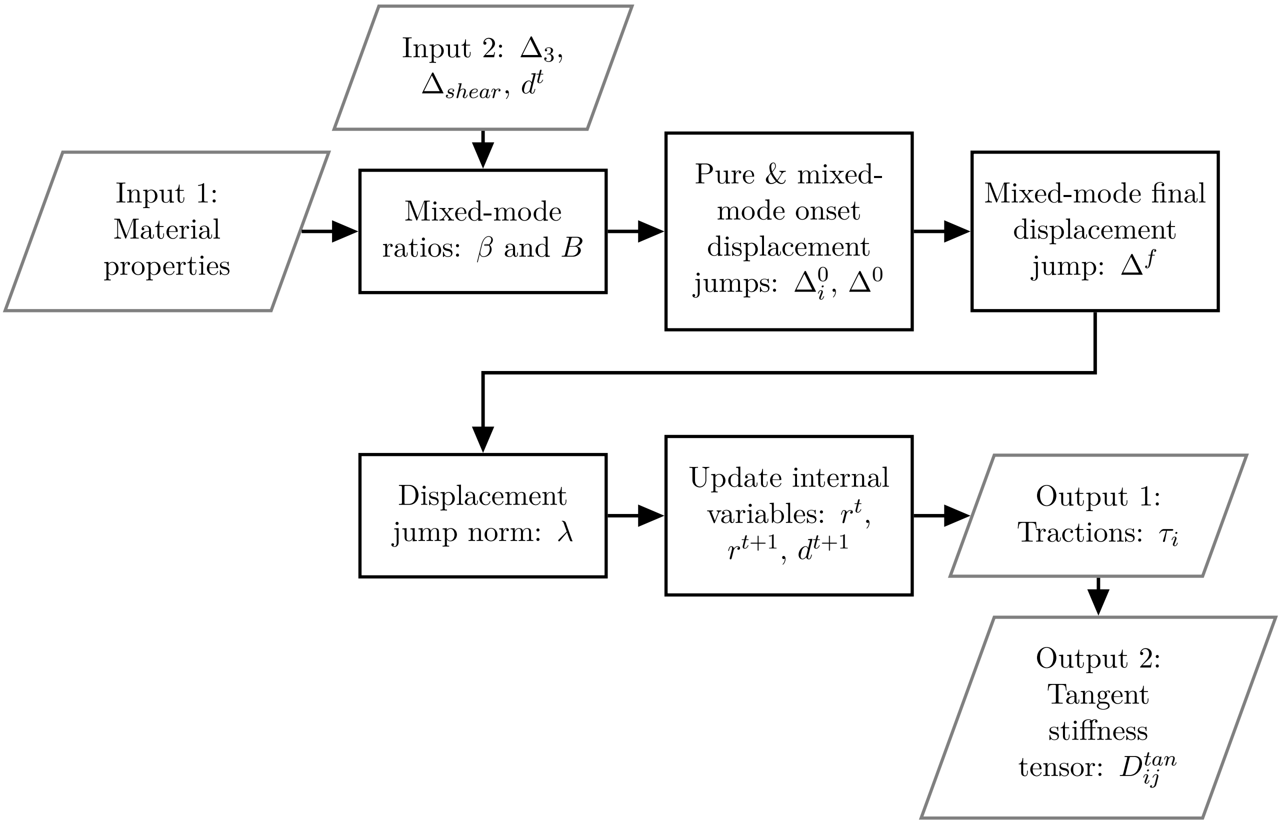

Figure 4.4: Flowchart of the UMAT routine for static loading.

4.2.2 User Material routine for fatigue loading

The routine to implement the fatigue model is written according to the flowchart that shown in Figure 4.5.

Every iteration of the fatigue analysis starts with the computation of the static damage parameter according to the static model as described in Section 4.2.1.

Two phases can be distinguished during the analysis. In the first phase, the displacement starts at zero and is increased to the maximal cyclic displacement for the fatigue analysis. Only an analysis with the static routine is performed during this phase. Once the maximal cyclic displacement is reached at time step one, the fatigue phase of the analysis starts. During this phase, the displacement is kept constant at the maximum fatigue load. The displacement profile of the analysis can be seen in Figure 4.6.

In the first decision block it is tested whether the time step is larger than one, if so, the fatigue analysis can be initiated. At the same time, it is tested whether the static damage has not reached one, because this would mean that the element has already failed. It is unnecessary to calculate the fatigue damage if the element has already failed.

If the time step is larger than one and the static damage is smaller than one, the total damage is the sum of the static damage and the fatigue damage. The fatigue damage is the value

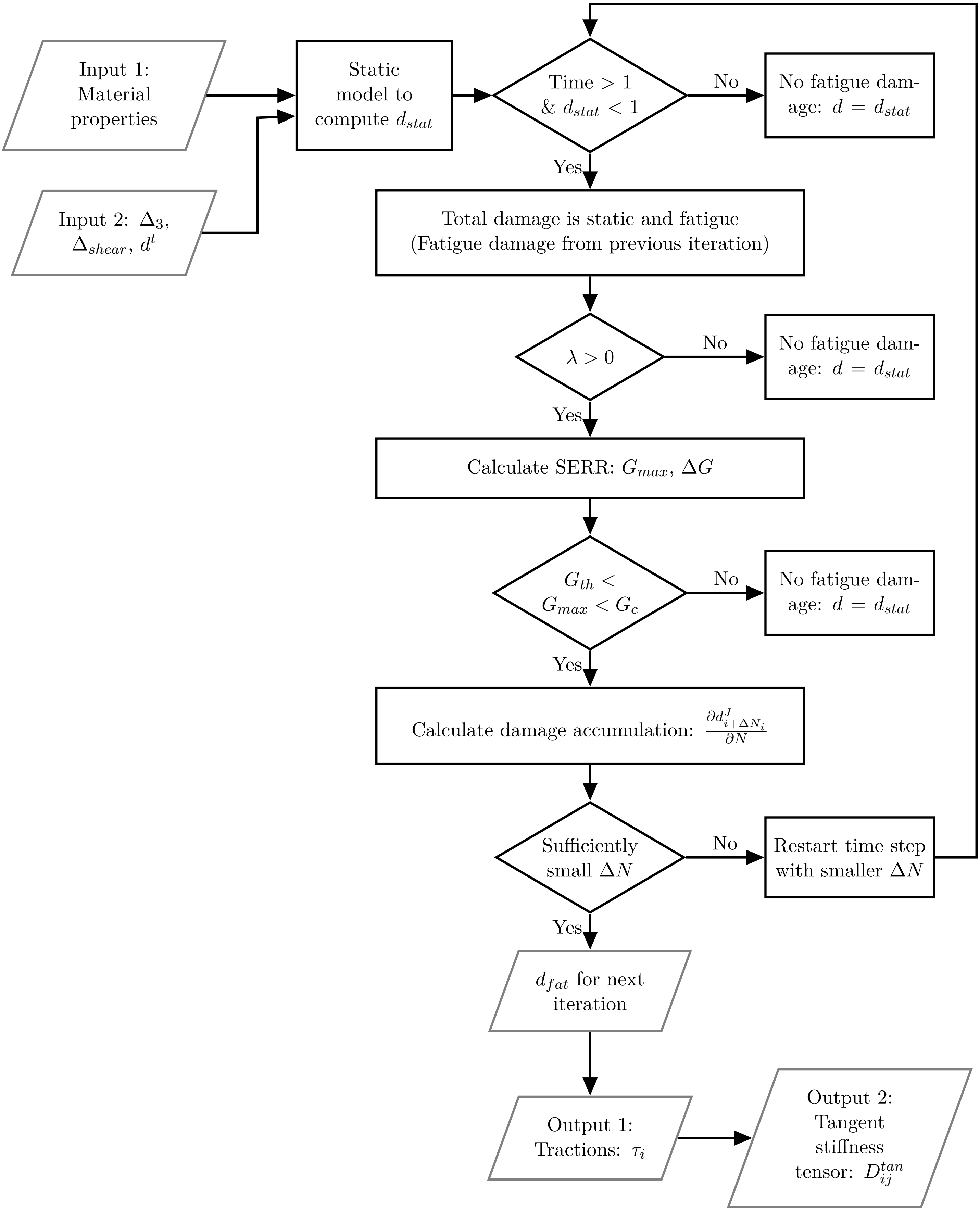

Figure 4.5: Flowchart for one iteration of the UMAT routine for fatigue loading.

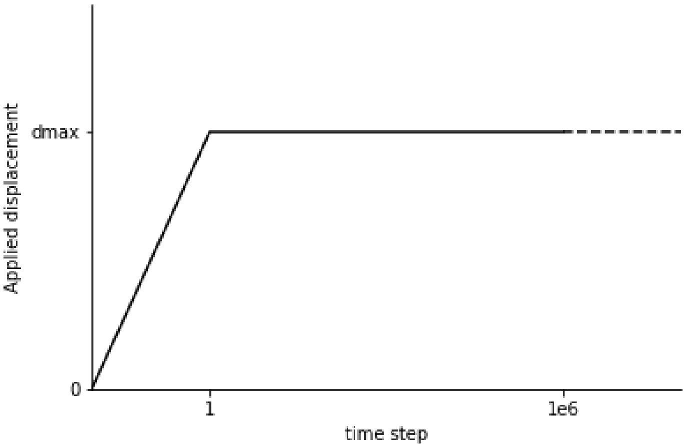

Figure 4.6: Displacement profile of the analysis.

that was calculated in the previous iteration. This yields the total damage at the start of the increment, which is used to calculate the tractions and the tangent stiffness tensor for the current iteration. The other steps in this iteration are used to calculate the change in fatigue damage during the current iteration, which will be used to calculate the fatigue damage of the next iteration.

The first step in the calculation of the change in fatigue damage is the check whether the displacement jump, λ is greater than zero. If this is not the case, there is no increase in fatigue damage in this iteration. This means that the damage that will be used in the next iteration only consists of static damage. Secondly, the maximal SERR during the fatigue cycle is obtained by computing the area under the TSL. The TSL during the fatigue analysis does not follow the bilinear TSL exactly. It shows a deviation due to the fatigue damage this can be seen in Figure 4.7.

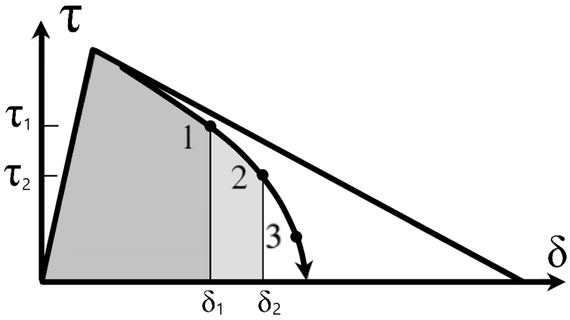

Figure 4.7: TSL for a cohesive element in a fatigue analysis.

Due to this deviation the SERR calculated with Equation 4.20 is only accurate for the first iteration of each element. For the elements thereafter, a trapezoidal approximation is used to obtain a more accurate value. With this approximation, the SERR is calculated as an incremental change with respect to the value of the previous iteration. The SERR at iteration N is calculated with:

$$G_{max,N} = G_{max,N-1} + \frac{(\tau_1 + \tau_2)}{2} * (\delta_2 - \delta_1) \tag{4.35}$$

Once the SERR is known, there is a check whether it is between the threshold and the critical value. If this is not the case, no fatigue damage is accumulated and the damage for the next iteration only consists of the static damage. To ensure that the fatigue damage accumulation is stopped only when the crack tip SERR is lower than the threshold before the element failure, a flag parameter is introduced. This is a binary parameter that is determined with the following part of the code.

```
!THE ELEMENT HAS JUST FAILED WHEN THE CURRENT DAMAGE IS ...
   ONE, BUT THE PREVIOUS VALUE IS LOWER THAN ONE
IF ((DMG .EQ. ONE) .AND. (DMG_OLD .LT. ONE)) THEN
    IF (G_MAX .LT. GTH) THEN
        KFLAG = 1
    ELSE
        KFLAG = 0
    END IF
END IF
```

Normally, in a UMAT routine, the current iteration for the current element can only access the state of that specific element and the global material parameters. To ensure that the analysis is stopped for the whole specimen, the parameter $KFLAG$ is defined as a $COMMON$ variable which means that it is passed between integration points.

In the cycle jump strategy, a maximal allowed damage accumulation is predetermined to limit the amount of cycles that are jumped according to Equation 4.22. When the calculated value exceeds this allowable, the iteration is restarted with a smaller time step. To perform this check, the $PNEWDT$ parameter is used. This parameter is the ratio of the suggested new time step and the current time step to use for a restart of the iteration. The analysis uses a pseudo-time where the number of cycles is equal to the analysis time. In the subroutine it is calculated with the following part of the code:

```
!MAX NUMBER OF CYCLES
DELTAN_MAX = DMG_MAX/DDDN
!CHECK FOR MAX NUMBER OF CYCLES
IF (DTIME.GT.DELTAN_MAX) THEN
    PNEWDT = 0.8*DELTAN_MAX/DTIME
END IF
```

The maximal allowed time increment is calculated with the maximum change in damage parameter, Δd_{max}, which is coded as DMG_MAX and $DDDN$ which is the change in damage parameter per cycle, calculated with Equation 4.17. This results in the maximal allowed time increment which is compared to the current time increment, $DTIME$. If the current time increment is too large, the iteration is restarted with a time increment that is 80% of the previously attempted increment. The new increment is not equal to the maximal increment so that the code is faster as it has to restart the analysis less frequently by taking a smaller value.

If the time increment is below the maximal allowed increment, the fatigue damage in the specific element is passed on to the next iteration for this element. At the start of the next iteration, this value is used to calculate the tractions and tangent stiffness tensor again. This process repeats for every element until the total damage in the element is equal to one.

Once the SERR in every element is smaller than the threshold ratio, the final crack length has been reached and the analysis will continue without running the subroutine, since calculation of the fatigue damage parameter is unnecessary.

4.3 Verification and Validation Strategy

This section describes the strategies that are used to verify and validate the results produced by the UMAT developed in this project.

To assess the implementation of the non-local propagation model, several coupon level tests are used. Validation consists of the comparison of the results of both subroutines to several benchmark tests available in literature.

4.3.1 Coupon level tests

To assess the performance of the developed UMAT, several coupon level tests are used. To characterize the mode I behaviour, a DCB specimen is chosen and for the mixed mode I and II behaviour, an MMB specimen is used. Both tests are standardised tests that are used to characterise the fracture behaviour of a material.

Pure mode I loading - DCB test

The DCB test is used to characterise the pure mode I opening behaviour of a material [6, 20, 41, 47, 48]. It consists of a single composite specimen, where a delamination or crack has been created during the manufacturing process by inserting a piece of non-adhesive foil at the desired location. During the test, the two arms of the specimen are pulled apart with a controlled displacement. This opens the arms of the specimen so that the initial crack is extended. A schematic of the test is presented in Figure 4.8. In this drawing, a represents the crack length, δ is the opening displacement and P is the reaction force.

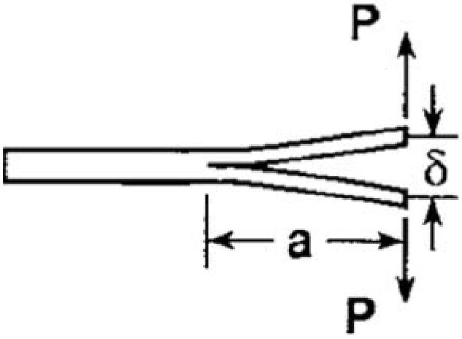

Figure 4.8: Schematic of the DCB test [49].

Mixed mode I and II loading - MMB test

For the characterisation of the behaviour under loading conditions with both mode I and II present, the MMB test is used [20, 22, 47, 50]. The specimen itself is similar to the DCB specimen. It is a composite specimen with an initial crack manufactured with a non-adhesive foil. To obtain mixed-mode loading conditions, the specimen is placed into a loading fixture as shown in Figure 4.9. In this schematic, c is the loading arm length and P is the reaction force.

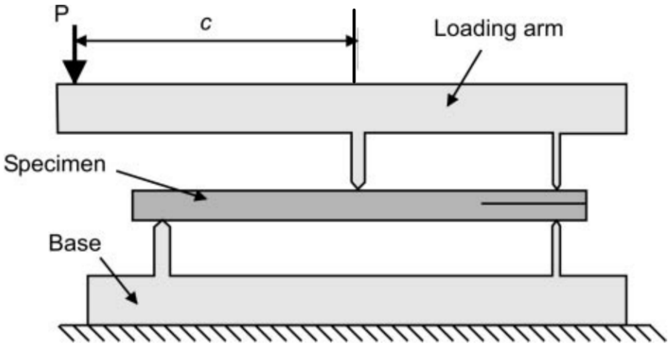

Figure 4.9: Schematic of the MMB test [8].

The loading fixture consists of a base which holds the specimen in place and ensures that the specimen is pinned at the opening of the initial crack. The loading is applied through the loading arm. The leftmost point of the loading arm is subjected to a downwards displacement. The right point of the loading arm is pinned to the specimen so that it opens the initial crack. The middle point of the loading arm applies a force on the specimen, this causes a mode II opening component to be present in the specimen. The mixed-mode ratio is fixed during the test and is determined based on the length of the loading arm, c. A shorter loading arm will induce a bigger mode II opening component.

4.3.2 Analytical calculations

This section describes an analytical calculation method based on LEFM. The method is used for the verification of the subroutines in three different ways. In the graphs with the results, all the results that are obtained with these methods are referred to as "Analytical".

For the static analysis, the equations are used to compute the resultant force-displacement curve. This is based on the assumption that the SERR is always equal to the critical SERR. This theoretical force-displacement curve can be compared to the results of the subroutine.

For the fatigue analyses, one of the verification strategies is to compare the resultant ${}^{da}/_{dN}$ and SERR to the Paris relation for the material. Because the calculation of the global SERR is not an inherent part of the CZM, this method is used to calculate the crack length and associated SERR based on the compliance of the specimen. The method is proposed by Reeder [51].

To verify the crack growth rate curves, the calculations for the SERR can be substituted into the Paris relation to obtain analytical expressions of the number of cycles as a function of the crack length.

Pure mode I loading - DCB test

When only mode I opening is present along the entire crack front, opening displacement is expressed as a function of the crack length as follows:

$$\delta_I = \left(\frac{2(a+\chi h)^3}{3EI}\right) P_I \tag{4.36}$$

where C_I is the compliance of the specimen, thus: $C_I = \delta_I / P_I$, E is the transverse stiffness, E_{33} of the specimen, I is the second moment of inertia of one arm, and h is the height of one arm, so half the height of the entire specimen. χ is a correction term calculated with:

$$\chi = \sqrt{\frac{E_{11}}{11G_{13}}\left[3 - 2\left(\frac{\Gamma}{1+\Gamma}\right)^2\right]} \tag{4.37}$$

where Γ is calculated with:

$$\Gamma = 1.18\frac{\sqrt{E_{11}E_{22}}}{G_{13}} \tag{4.38}$$

In Equation 4.36, P_I and δ_I are the mode I opening force and displacement as defined in Figure 4.10.

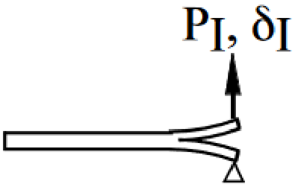

Figure 4.10: Definition of the DCB specimen opening force and displacement [7].

With the crack length known, the SERR is calculated based on LEFM:

$$G = \frac{P^2}{2b}\frac{dC}{da} \tag{4.39}$$

Thus resulting in an expression for the SERR

$$G_I = \frac{P_I^2(a + \chi h)^2}{bEI} \tag{4.40}$$

To obtain the analytical expression for the fatigue crack growth, a function for the SERR is substituted into the Paris relation, shown in Equation 4.19. To be able to compute the resulting value, the maximal SERR during the fatigue cycle should be expressed as a function of one unknown, the crack length a. This is achieved by combining Equations 4.36 and 4.40. This results in:

$$G_{max} = \frac{9EI\delta_{max}^2}{4b(a + \chi h)^4} \tag{4.41}$$

The Paris relation is rewritten to obtain an expression for the number of cycles:

$$N = \int_{a_0}^{a} \frac{1}{CG_{max}^m} da \tag{4.42}$$

When this integral is solved with a certain upper limit, a, the result is the number of cycles that is necessary to reach that crack length. The resulting expression is:

$$N(a) = \frac{1}{(4m+1)C}\left(\frac{4b}{9EI\delta_{max}^2}\right)^m \left[(a + \chi h)^{4m+1} - (a_0 + \chi h)^{4m+1}\right] \tag{4.43}$$

This expression is used to calculated the number of cycles for every crack length until the final crack length is reached. The final crack length is calculated by solving Equation 4.41 for the crack length, a, when $G_{max} = G_{th}$.

Mixed mode I and II loading - MMB test

When mode II loading is also present along the crack front, the test can be represented as a decomposition of a pure mode I test (DCB) and a pure mode II test, an ENF, such as shown in Figure 4.11.

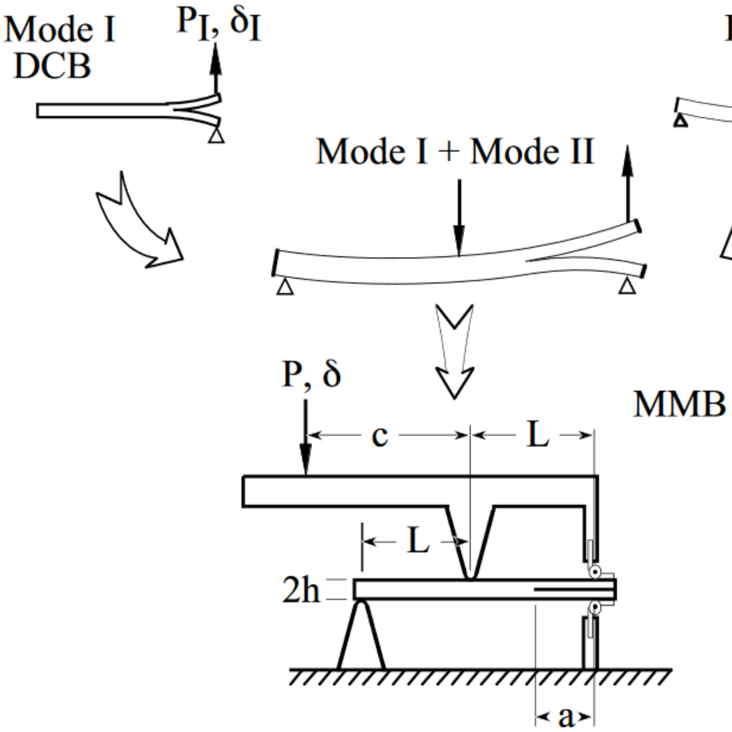

Figure 4.11: Decomposed representation of the MMB specimen [7].

The total reaction force is split in two pure mode components with the following equation:

$$P_I = P * \left(\frac{3c - L}{4L}\right) \text{ and } P_{II} = P * \left(\frac{c + L}{L}\right) \tag{4.44}$$

In the same way, the pure mode displacements can be combined to find the total displacement.

$$\delta = \left(\frac{3c - L}{4L}\right)\delta_I + \left(\frac{c + L}{L}\right)\delta_{II} \tag{4.45}$$

Note that the displacement in this case is the vertical displacement of the loading point at the end of the lever. c is the length of the lever and L is half of the specimen length.

The mode II compliance and SERR are calculated with the same correction factor as the mode I calculations.

$$G_{II} = \frac{6P_{II}^2(a + 0.42\chi h)^2}{64bEI} \text{ and } C_{II} = \frac{\delta_{II}}{P_{II}} = \frac{2L^3 + 3(a + 0.42\chi h)^3}{96EI} \tag{4.46}$$

Combining this with the equations from the pure mode I loading conditions and equations 4.44 and 4.45, an expression for the total displacement is obtained:

$$\delta = \frac{4(3c-L)^2(a+\chi h)^3 + (c+L)^2\left[3(a+0.42\chi h)^3 + 2L^3\right]}{96L^2EI}P \tag{4.47}$$

With the LEFM relation from the calculation for the DCB specimen, the total SERR is calculated:

$$G_{tot} = \frac{4(3c-L)^2(a+\chi h)^2 + (c+L)^2 3(a+0.42\chi h)^3}{64bL^2EI}P^2 \tag{4.48}$$

For the fatigue analyses verification, the procedure can be performed as described here. Starting from the compliance which can be easily extracted from the results of the analysis. This leads to the calculation of the global SERR that is used to compare the Paris relation.

For the verification of the static analyses, the equations have to be used in a different way. Starting from a known SERR, which is equal to the critical SERR the equations can be used to calculate the compliance for each crack length and construct a force-displacement curve that can be compared to the results of the analyses.

Similar to the procedure for the pure mode I loading, an expression for G_{max} has to be obtained to substitute it into the Paris relation. This can be obtained by combining Equations 4.47 and 4.48:

$$G_{max} = \frac{144EI}{b}L^2\delta_{max}^2 \frac{4(3c-L)^2(a+\chi h)^2 + (c+L)^2 3(a+0.42\chi h)^3}{\left(4(3c-L)^2(a+\chi h)^3 + (c+L)^2\left[3(a+0.42\chi h)^3 + 2L^3\right]\right)^2} \tag{4.49}$$

This expression is substituted in Equation 4.42. In this case, solving the expression analytically would result in a rather complex expression, thus the integral is solved numerically. The final crack length is calculated by finding the crack length for which $G_{max} = G_{th}$

4.3.3 Benchmark tests

The static analysis of the DCB specimen is compared to a test performed by Turon et al. [21]. These results are part of the validation study for the model that is presented. The results are referred to as "Benchmark Turon" For the fatigue analysis, results by Krüger [9] are used. The MMB specimens under static loading are compared to results by Krüger [52]. This benchmark was created using an independent analysis software based on the VCCT. For the fatigue loaded MMB specimens, results by Krüger and Carvalho [53] are used. The fatigue benchmark was also created using the VCCT in combination with the Paris relation. All the results by Krüger are referred to as "Benchmark Krüger".

In the static models, the most important comparison is the force-displacement behaviour of the specimen. The important parameters are the compliance, final failure load and critical displacement. The analysis results are compared to the benchmarks mentioned above and to a static analysis of the same model that is performed with the default cohesive elements in Abaqus.

For the fatigue analysis, the crack growth will be used as a comparison parameter. This means that the crack length vs number of cycles will be compared to the benchmark results. Furthermore, the resultant Paris relation can be compared to the input for the model.

Chapter 5

DCB and MMB finite element models

This chapter contains a description of the different FE specimens that were used in this project, including their material parameters. The mode I behaviour is investigated with a DCB specimen. For the mixed-mode behaviour, a MMB specimen is used.

Firstly, the experimental set-up of the DCB specimen is described. The response of the specimen was modelled for both static and fatigue loading with a 2D and a 3D model. The DCB specimens for the static and fatigue analysis have a different specimen geometry. Secondly, the set-up for the MMB specimen is treated. This specimen was analysed with different mixed-mode ratios. The response was also modelled for static and fatigue loading with 2D and 3D models. The MMB specimens all have the same specimen geometry.

5.1 Double Cantilever Beam (DCB) specimen

The DCB specimen is used to characterize the mode I behaviour of a material. The models for static and fatigue analyses use specimens with different materials and dimensions. This choice was made because of the availability of benchmark data.

5.1.1 Static analysis

For the static analysis, the DCB specimen is used as described by Turon et al. [21]. The specimen is modelled with a 2D plane strain analysis and a 3D analysis. Both specimens are used in two analyses types. First the default cohesive material in Abaqus is used with a traction separation constitutive description. Secondly, the UMAT described in Chapter 4 is used.

Specimen geometry

A schematic drawing of the specimen is shown in Figure 5.1, the dimensions of the specimen are given in Table 5.1.

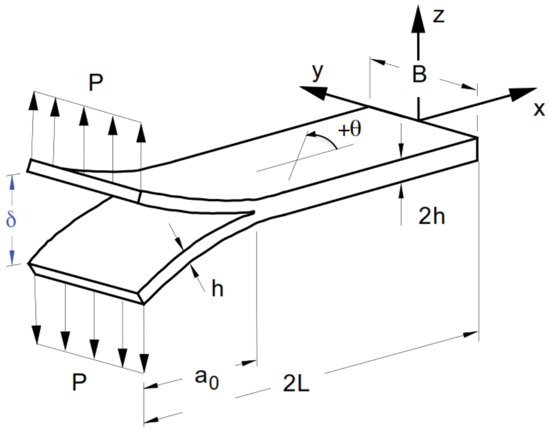

Figure 5.1: Schematic drawing of the DCB specimen [9].

Table 5.1: Dimensions of the DCB specimen for static analysis [43].

Parameter	Value
Arm height (h)	1.98 mm
Length ($2L$)	150 mm
Width (B)	20.0 mm
Initial crack length (a_0)	55.0 mm

The lay-up of the specimen is a unidirectional T300/977-2 carbon fibre reinforced epoxy laminate with an orientation of 0 degrees with 12 plies in each arm. The material properties are listed in Table 5.2.

Table 5.2: Material properties of T300/977-2 carbon fibre reinforced epoxy [43].

Parameter	Value
E_{11}	150 GPa
E_{22}	11.0 GPa
E_{33}	11.0 GPa
υ_{12}	0.25
ν_{13}	0.25
υ_{23}	0.45
G_{12}	6.00 GPa
G_{13}	6.00 GPa
G_{23}	3.70 GPa
G_{IC}	0.352 N/mm

FE model

The 2D specimen is modelled with 4-node bilinear plane strain elements with incompatible modes, CPE4I. The choice for an element with incompatible modes was made because of the improved bending behaviour [40]. Two different element widths are used. The region in which crack growth is expected, uses a smaller element width of 0.05 mm. The smaller element width is also needed a few millimetres before the crack tip to ensure that the stress concentration at the crack tip is completely captured. For the outer regions of the specimen a larger element width of 0.5 mm is used. The specimen has four elements through the thickness. The specimen can be seen in Figure 5.2. The 2D specimen has 4144 nodes and 3020 elements.

The interface is modelled with a 4-node two-dimensional cohesive element, COH2D4. The interface is divided in the same regions as the rest of the specimen, with a smaller element width in the region of crack growth and a larger element width in the outer regions. The elements are modelled as zero thickness elements to minimise their influence on the mechanical behaviour. There are no cohesive elements on the interface of the initial crack, there are free nodes on both sides of the specimen.

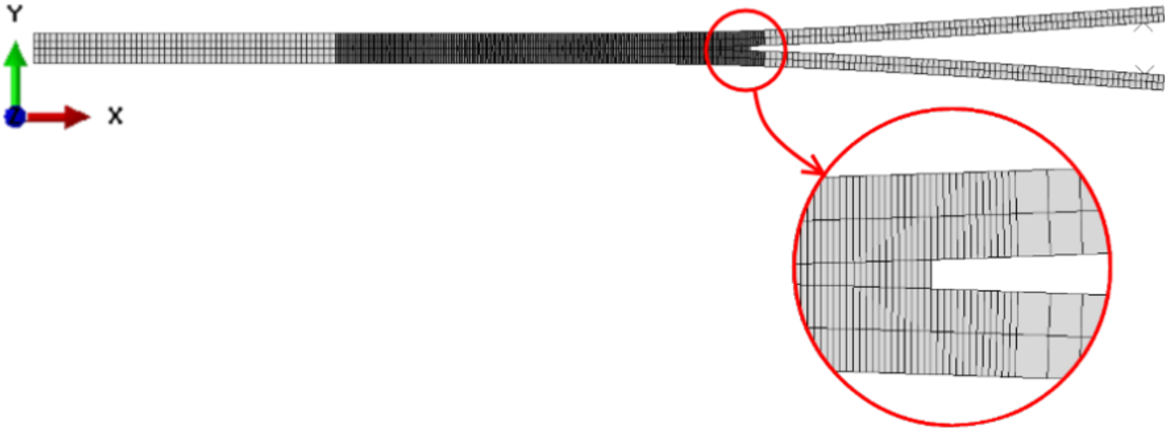

Figure 5.2: Mesh of the 2D DCB specimen.

For the 2D analysis, a static general step is used with a minimum step size of 1e-15 and a maximum step size of 0.01. The applied displacement is increased until 3.5 mm on each of the arms, resulting in the final opening displacement of the specimen is 7 mm. The boundary conditions for the specimen can be seen in Figure 5.3. The displacement is applied equally to the tips of the specimen arms and the opposite edge is clamped

Figure 5.3: Boundary conditions for the 2D DCB specimen.

For the 3D specimen, 8-node quadrilateral continuum shell elements, SC8R, are used. The choice for continuum shell elements, rather than conventional shell elements, was made because the setup of the elements. Continuum shell elements have 8 nodes which all have displacement degrees of freedom. On the other hand, conventional shell elements only model the reference surface with 4 nodes which rotational and displacement degrees of freedom. These characteristics make it easer to connect the cohesive elements and the continuum shell elements since they have shared nodes at the interface. The cohesive interface is modelled with an 8-node three-dimensional cohesive element, COH3D8. This element has the same degrees of freedom as the continuum shell elements. The element sizes are the same as for the 2D model, with 27 elements through the width of the specimen. The isometric view is shown in Figure 5.4. The 3D specimen has 84.840 nodes and 65.772 elements.

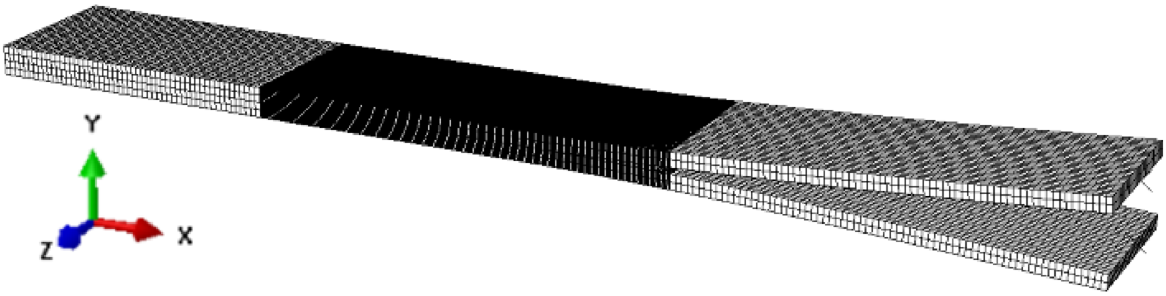

Figure 5.4: Mesh of the 3D DCB specimen.

The boundary conditions of the 3D specimen can be seen in Figure 5.5. The displacement is applied through two reference points at the tips of the specimen arms. The reference points are tied to the front row of nodes with a rigid body tie. This enforces the whole front node to have the same displacement. The opposite edge of the specimen is clamped.

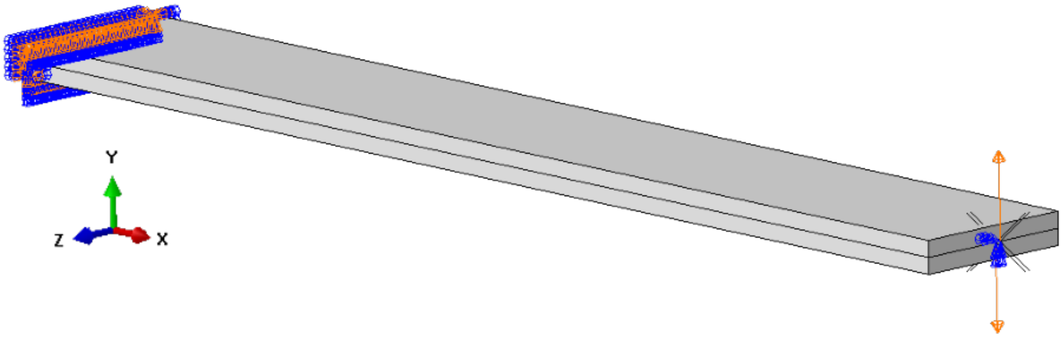

Figure 5.5: Boundary conditions for the 3D DCB specimen.

The 3D analysis was not able to converge with a static general analysis. This is due to the high stiffness drop when initial failure occurs. Adding artificial viscosity led to convergence, but accuracy was lost. Therefore the 3D analysis was performed with a dynamic implicit step with a slow enough load application so that dynamic effects are minimized and the loading can be considered quasi-static.

5.1.2 Fatigue analysis

The DCB specimen for fatigue analysis is dimensioned according to the benchmark developed by Krüger [9]. Again, both a 2D plane strain and a 3D model are used. The fatigue analysis will only be performed with the UMAT since the default cohesive elements from Abaqus are not capable of modelling high-cycle fatigue.

Specimen geometry

The specimen dimensions are given in Table 5.3. This specimen is manufactured from a unidirectional graphite/epoxy prepreg, T300/1076, with a 0 degree orientation with 12 plies in each arm, the material parameters of this material can be seen in Table 5.4.

Table 5.3: Dimensions of the DCB specimen for fatigue analysis [9].

Parameter	Value
Arm height (h)	1.50 mm
Length ($2L$)	150 mm
Width (B)	25.0 mm
Initial crack length (a_0)	30.5 mm

Table 5.4: T300/1076 material properties [9].

Parameter	Value
E_{11}	139.4 GPa
E_{22}	10.16 GPa
E_{33}	10.16 GPa
v_{12}	0.30
v_{13}	0.30
v_{23}	0.436
G_{12}	4.60 GPa
G_{13}	4.60 GPa
G_{23}	3.54 GPa

The parameters that are used for the cohesive zone can be seen in Table 5.5

FE model

For the 2D and the 3D analyses, the specimen is set up in the same way as the specimens for static analyses, with a similar mesh distribution and the same element types. The 2D specimen has 7.206 nodes and 5.903 elements and the 3D specimen has 62.312 nodes and 47.565 elements. The analysis is divided in two phases. During the first phase, a static analysis is performed where the displacement is increased until the maximal displacement. During the second phase, the displacement is kept constant and the time represents the number of fatigue cycles. The load profile can be seen in Figure 4.6. Both phases use a static

Table 5.5: Cohesive parameters for the DCB specimen for fatigue analysis.

Parameter	Value
K	1.70e5 N/mm^3
τ_3^0	30.0 MPa
G_{IC}	0.17 N/mm
G_{Ith}	0.06 N/mm
RATIO	0.1
C_I	2.44e6
m_I	10.61
D_{max}	0.001

general step. The simulation of the fatigue cycles is done according to the cycle jump strategy that is discussed in Chapter 4. The maximal displacement is 0.67 mm on each arm, resulting in a total displacement of 1.34 mm and the load ratio is 0.1.

5.2 Mixed-Mode Bending (MMB) specimen

To characterise the mixed-mode behaviour, an MMB specimen is used. The model is set up according to the benchmark developed by Krüger [52]. For static and fatigue analyses, the same specimens with the same dimensions and material parameters are used. Similar to the DCB specimen, the static analysis is performed with the default Abaqus cohesive material with a traction separation constitutive description and with the UMAT from Chapter 4.

Specimen geometry

A schematic drawing of the specimen can be seen in Figure 5.6. The mixed-mode ratio is dependent on the length of the loading arm, marked as c in the drawing. The tests are performed with a mixed-mode ratio of 0.2 and 0.5.

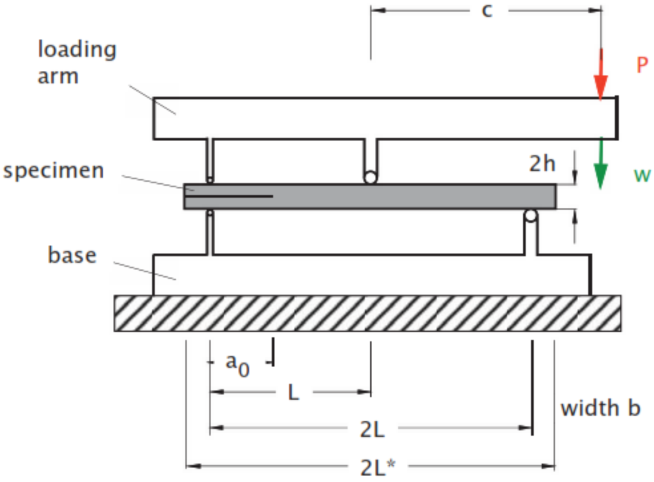

Figure 5.6: Schematic drawing of the MMB specimen [52].

The dimensions of the specimen are summarised in Table 5.6.

Table 5.6: Dimensions of the MMB specimen [9].

Parameter	Value
Arm height (h)	2.25 mm
Length ($2L$)	100.8 mm
Width (B)	25.4 mm
Initial crack length (a_0)	25.4 mm
Loading arm length for $G_{II}/G_T = 0.2$ (c)	92.9 mm
Loading arm length for $G_{II}/G_T = 0.5$ (c)	41.3 mm

The specimen is made of a unidirectional graphite/epoxy prepreg, IM7/8552, with an orientation of 0 degrees with 12 plies in each arm, the material parameters are shown in Table 5.7. The cohesive parameters for both the static and the fatigue analysis can be seen in Table 5.8.

Table 5.7: IM7/8552 material properties [52].

Parameter	Value
E_{11}	161.0 GPa
E_{22}	11.38 GPa
E_{33}	11.38 GPa
v_{12}	0.32
v_{13}	0.32
v_{23}	0.45
G_{12}	5.20 GPa
G_{13}	5.20 GPa
G_{23}	3.90 GPa

Table 5.8: Cohesive parameters for the MMB specimen.

Parameter	Value
K	1.70e5 N/mm^3
τ_3^0	32 MPa
τ_1^0	61 MPa
τ_2^0	61 MPa
G_{IC}	0.212 N/mm
G_{IIC}	0.774 N/mm
G_{IIIC}	0.774 N/mm
η	2.1
$G_{th,20}$	0.06 N/mm
C_{20}	2412
m_{20}	8.4
$G_{th,50}$	0.06 N/mm
C_{50}	6.79
m_{50}	5.40
D_{max}	0.001

FE model

The 2D specimen is composed of CPE4I elements, with COH2D4 elements for the cohesive interface. Similar to the DCB specimen, the region around the expected crack is modelled with a fine mesh of 0.05 mm. The interface of the initial crack has free nodes and the finer mesh starts before the crack tip. The outer regions of the specimen are modelled with a coarser mesh of 0.5 mm. The specimen has six elements through the thickness. The mesh distribution can be seen in Figure 5.7. The 2D MMB specimen has 4.402 nodes and 3.095 elements.The boundary conditions for the 2D specimen are shown in Figure 5.8.

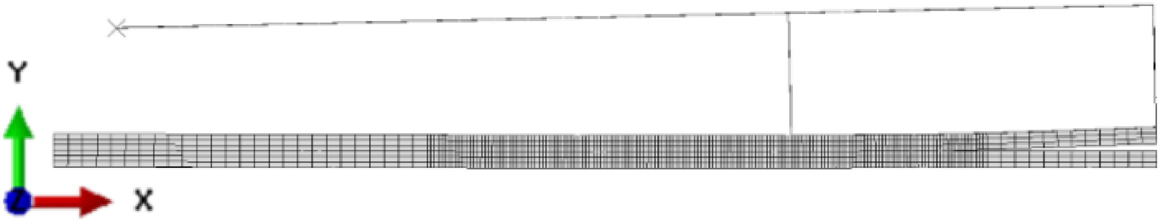

Figure 5.7: Mesh of the 2D MMB specimen.

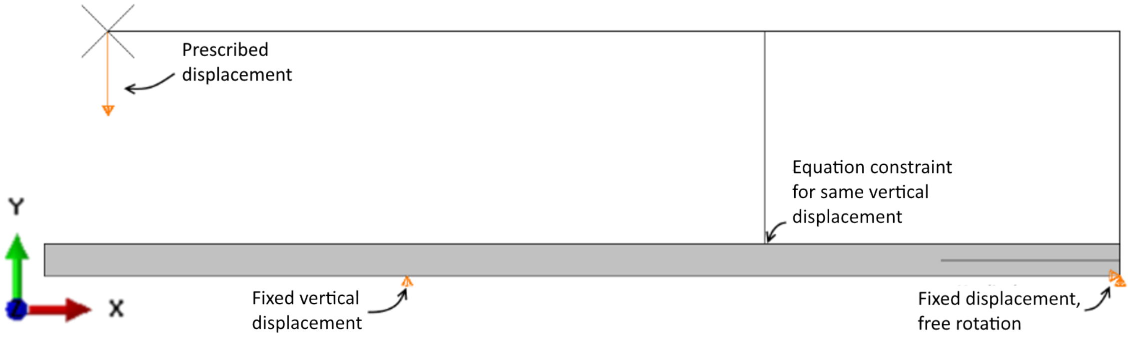

Figure 5.8: Boundary conditions of the 2D MMB specimen.

The 3D specimen uses SC8R elements for the arms of the specimen and the cohesive interface is modelled with COH3D8 elements. The mesh size is the same as for the 2D specimen, with 14 elements through the width. The top view of the mesh can be seen in Figure 5.9. The 3D specimen has 81.070 nodes and 65.930 elements.

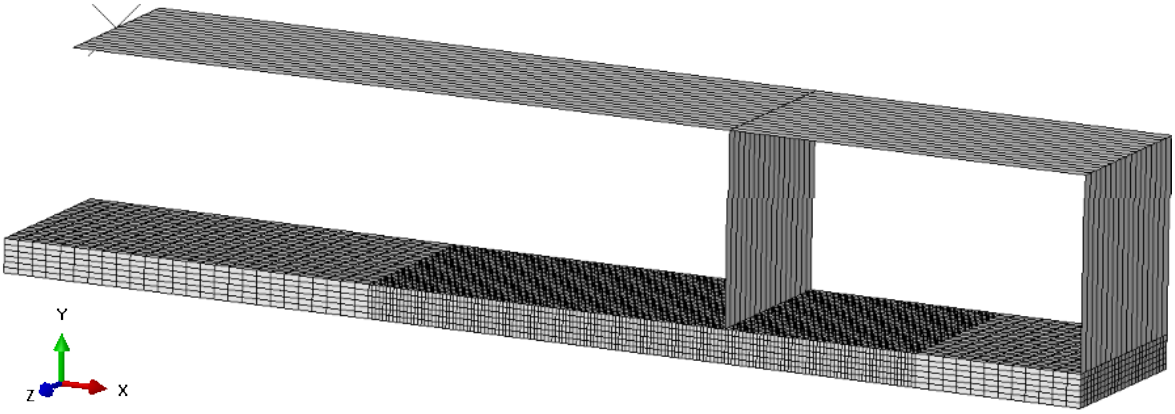

Figure 5.9: Mesh of the 3D MMB specimen.

The loading arm is modelled with rigid elements, with a pin constraint to the front row of the specimen. A surface-to-surface constraint is used to impose the vertical displacement of the loading arm on the middle of the specimen. These boundary conditions can be seen in Figure 5.10.

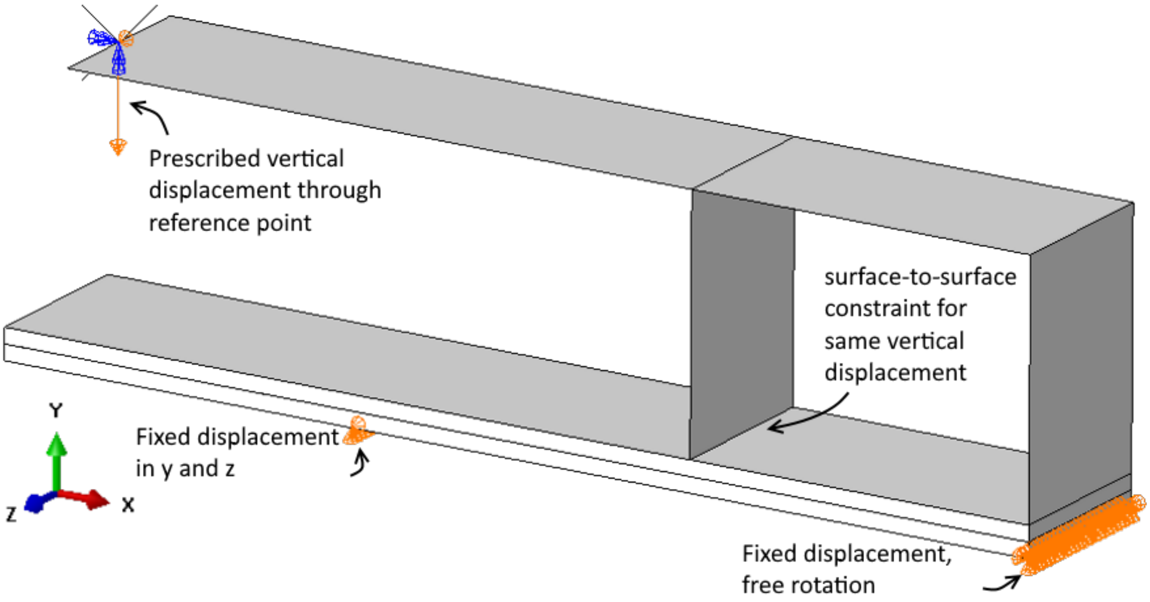

Figure 5.10: Boundary conditions of the 3D MMB specimen.

5.2.1 Static analysis

For the static analyses, the applied displacement has a linear increase from 0 mm to 10 mm. The 2D specimens converge with a static general step without added artificial viscosity. For the 3D specimens, however, a dynamic implicit analysis is used. This is necessary to overcome the drop in stiffness when the specimen fails. The loading is applied slow enough to minimise the dynamic effects so that the analysis can be compared to a quasi-static analysis.

5.2.2 Fatigue analysis

In the fatigue analyses, a maximum displacement of 1.27 mm and 1.04 mm is applied for G_{II}/G_T is 0.2 and 0.5 respectively. The load ratio is 0.1 for both analyses. The fatigue analysis is performed in the same way as the DCB tests. So two loading phases are executed, where the displacement is increased in the first step and is kept constant during the second step. The loading profile can be seen in Figure 4.6.

Chapter 6

Results

In this chapter, the results of the FE analyses are presented. Both the DCB specimen and MMB specimen with different mixed-mode ratios are analysed. Both specimens are modelled in a 2D plane strain and a full 3D configuration to compare the accuracy. All of these specimens were used in a static and a fatigue analysis. The static analysis results are compared to benchmark results from literature [30, 52] and to results of the default cohesive elements in Abaqus [40]. The fatigue analyses results are only compared to benchmark results from literature [9, 53].

6.1 Double Cantilever Beam (DCB) specimen

To characterise the mode I opening behaviour of a material, the DCB specimen is used. An initial crack is created in the specimen and the two arms are pulled apart with a controlled displacement. The specimen is subjected to a static or fatigue loading, both are shown in this section.

6.1.1 Static results

Since the default cohesive elements implemented in Abaqus [40] are capable of modelling static crack growth, the UMAT results can be compared to the results obtained with Abaqus. This is done to verify the FE models before using them to predict the fatigue behaviour of the specimens.

Sensitivity study

For the DCB static analysis, a convergence check is performed with the 2D model with the default Abaqus cohesive model. The results are compared to the analytical solution from Section 4.3.2. It is assumed that these values will also be a good configuration to perform the

3D analyses and the analysis with the cohesive model from the UMAT. The most important parameters that determine the success of a cohesive FE analysis are the interface strength and stiffness and the size of the elements in the cohesive zone. A convergence check is done for these 3 parameters. Note that only one parameter is varied while the others are kept constant so that the influence of the specific parameter can be determined.

The load displacement curves are used as a tool to compare the performance of different input parameters. Figure 6.1 shows a close-up image of the load-displacement response at the critical displacement. It can be seen that element sizes of 0.2 mm and larger result in non-convergence of the analysis and are thus unsuitable. For the smallest element size of 0.025 mm, the response shows saw-teeth after the critical displacement, this is undesired numerical noise because the element size is too small. The element size of 0.1 is chosen as a suitable value because it is the highest possible value for convergence that also has enough elements in the processing zone to provide a accurate description of the behaviour.

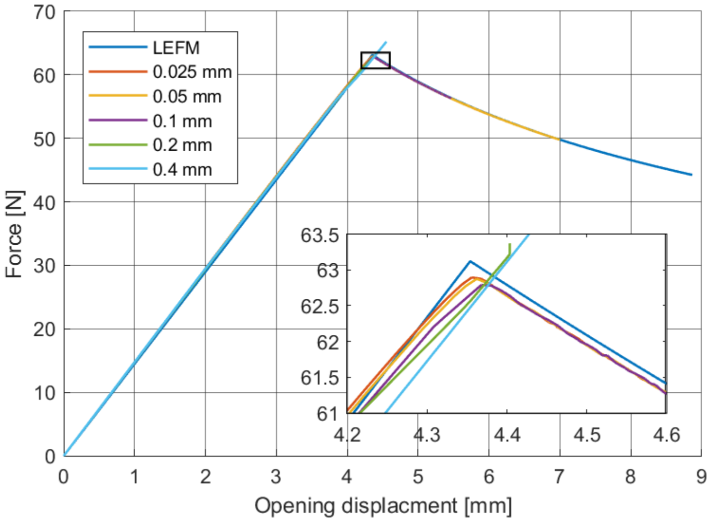

Figure 6.1: Force-displacement curve for the 2D static DCB specimen for different interface element sizes.

The results for different interface stiffnesses are compared in Figure 6.2. The lowest stiffness of 555 N/mm is too low, since there is no traction in the cohesive surface, thus the elements don not fail. The highest stiffness approaches is so large that once the cohesive surface is separated, the traction goes to infinity and no failure will occur. Between those values, the final value of $5.55e5$ N/mm was chosen because it allows for convergence of the analysis and provides a sufficient number of elements in the cohesive zone.

The interface strength was also varied during different analyses. The resultant force-displacement response is shown in Figure 6.3. The entire curve shows little difference, thus a detail around the critical displacement is shown. The lowest value of 45 MPa leads to abortion of the analyses around the critical displacement point. The value of 50 and 65 MPa result in a fair amount of numerical noise after failure has occurred. Therefore, a value of 60 MPa was chosen for these analyses.

The chosen values for the cohesive zone for the DCB specimen are shown in Table 6.1.

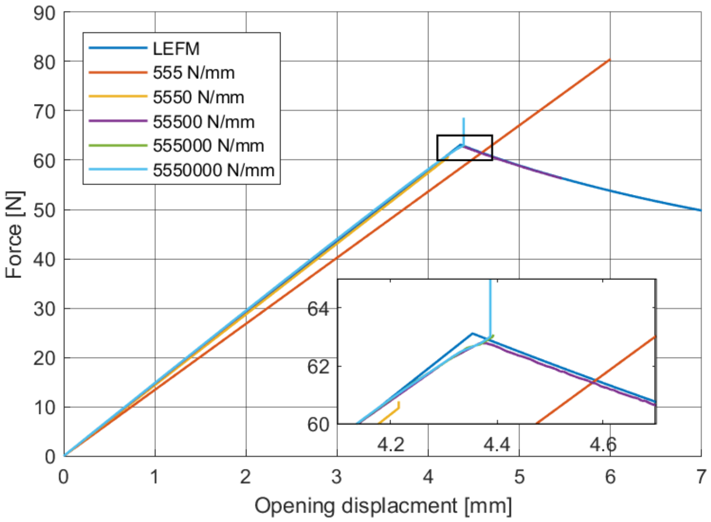

Figure 6.2: Force-displacement curve for the 2D static DCB specimen for different interface stiffnesses.

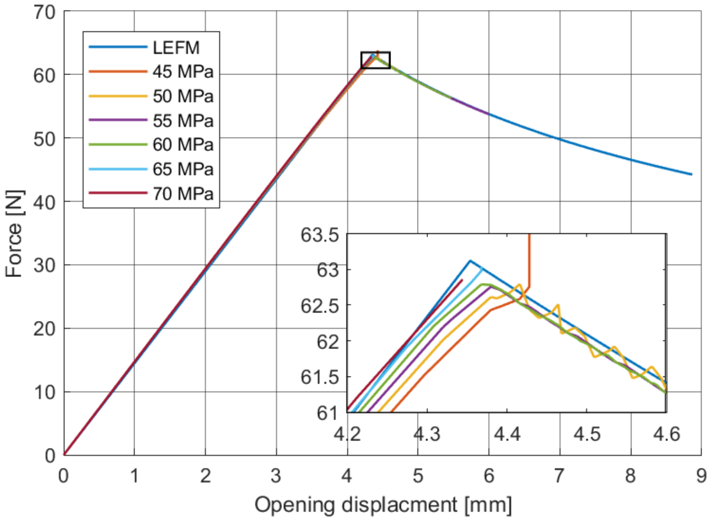

Figure 6.3: Force-displacement curve for the 2D static DCB specimen for different interface strengths.

Table 6.1: Cohesive parameters for the DCB specimen for static analysis.

Parameter	Value
element size	0.05 mm
K	5.55e5 N/mm^3
τ_3^0	60 MPa

Force-displacement results

The displacement profile of the 2D DCB specimen is shown in Figure 6.4 and the 3D DCB specimen can be seen in Figure 6.5.

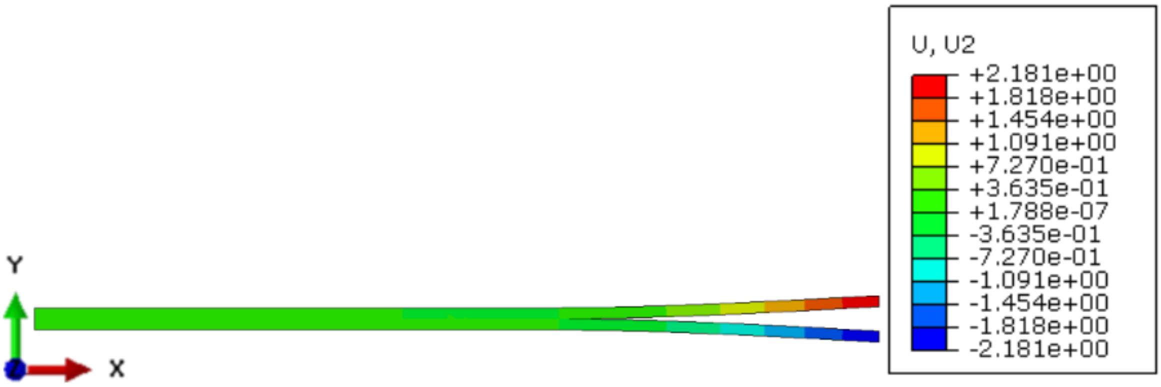

(a) Opening displacement of 4.36 mm.

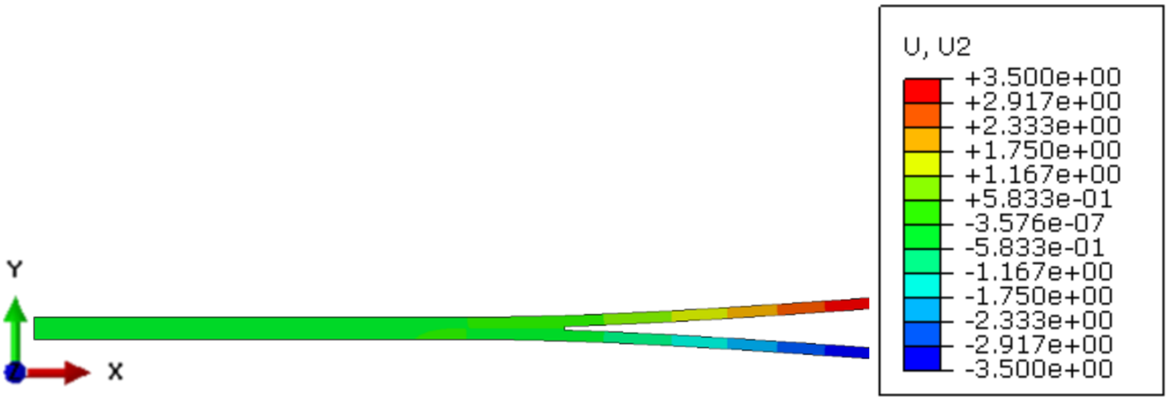

(b) Opening displacement of 7 mm.

Figure 6.4: Displacement profile of the 2D DCB specimen at two different opening displacements obtained with the UMAT during the static analysis.

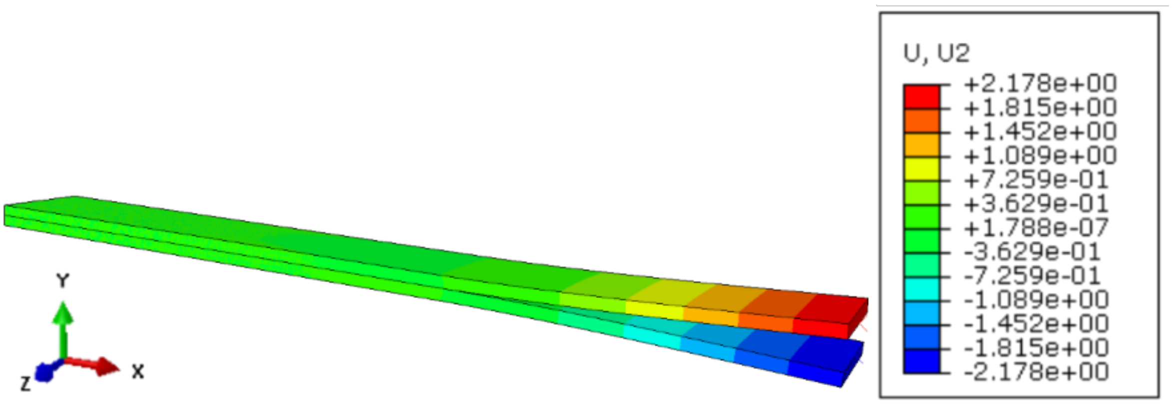

(a) Opening displacement of 4.36 mm.

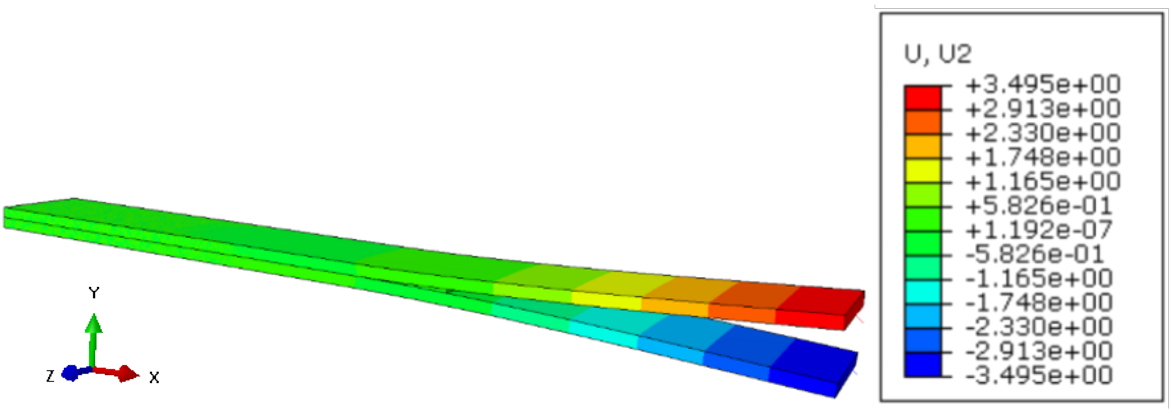

(b) Opening displacement of 7 mm.

Figure 6.5: Displacement profile of the 3D DCB specimen at two different opening displacements obtained with the UMAT during the static analysis.

The resultant force-displacement plots for the static DCB models can be seen in Figure 6.6. The total reaction force is measured at the point of load application on the upper arm of the specimen. In the 2D specimen, this is just a single node. In the 3D specimen, the load is applied through a row of nodes so the reaction force of each of these nodes is summed to obtain the total reaction force. The opening displacement is computed by extracting the displacement from this same node and multiplying it by two since the two arms have the same displacement in opposite direction.

The results are compared to the benchmark by Turon et al. [21] and the theoretical LEFM solution. The critical force and displacements are summarized in Table 6.2. The percentage difference with the LEFM solution are also given.

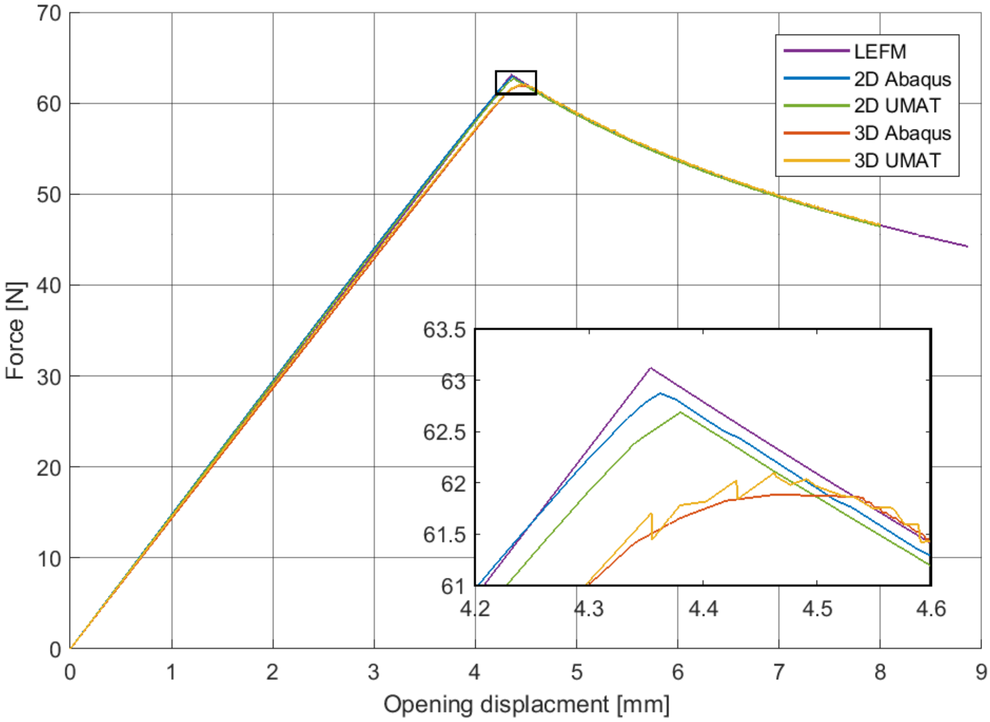

Figure 6.6: Force-displacement curve for the static DCB specimen.

Table 6.2: Critical force and displacement for the DCB static analyses compared to the LEFM solution.

	Critical force [N]	Difference [%]	Critical displacement [mm]	Difference [%]
LEFM	63.12	-	4.35	-
2D Abaqus	62.87	0.39	4.36	0.19
2D UMAT	62.69	0.69	4.38	0.60
3D Abaqus	61.88	1.98	4.46	2.41
3D UMAT	62.10	1.63	4.46	2.47

It can be seen that all the analyses show a slightly higher stiffness than the experimental benchmark. This can be attributed to the fact that the numerical analyses assume pristine material and loading conditions, which is not the case for the experimental tests. The different numerical analyses all show the same stiffness. The critical opening displacement of the numerical analyses is slightly lower in the numerical analyses than the benchmark, but the critical load matches the benchmark. After failure, the numerical analyses all show the same decreasing reaction force, but the benchmark shows a slower decrease in reaction force. This can be attributed to the uncertain nature of experimental results.

The crack front of the 3D DCB specimen at two different opening displacements can be seen in Figure 6.7. The crack front shows the toenail shape that is expected in a DCB specimen.

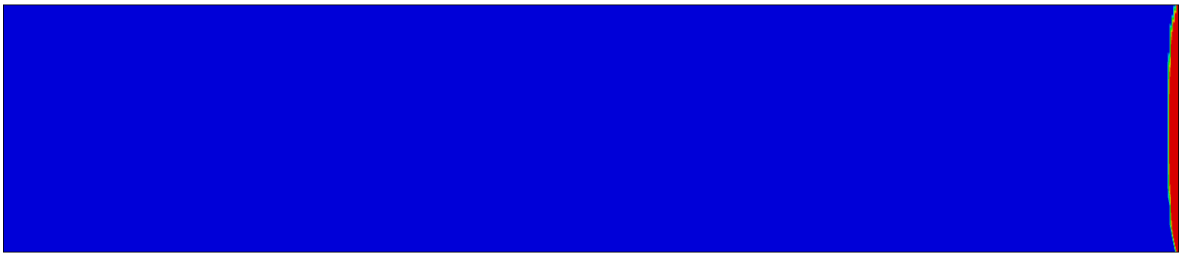

(a) Opening displacement of 4.36 mm.

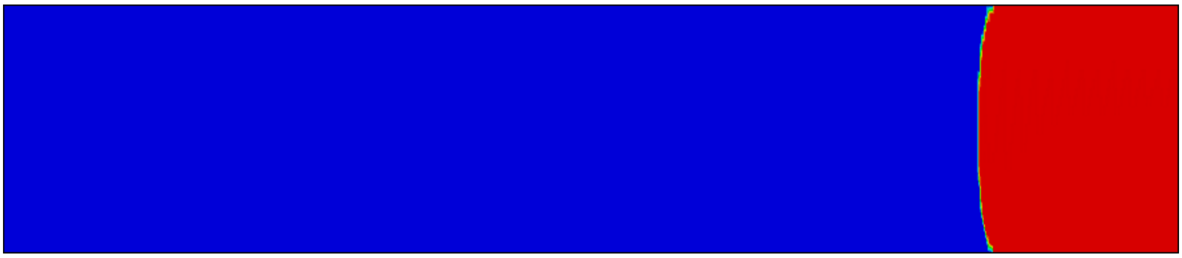

(b) Opening displacement of 7 mm.

Figure 6.7: Crack front of the 3D DCB specimen at two different opening displacements obtained with the UMAT during the static analysis.

6.1.2 Fatigue results

The default cohesive elements from Abaqus [40] are not able to perform fatigue analyses. Therefore only results from the UMAT for 2D and 3D analyses are compared to a benchmark. The benchmark is taken from analyses performed by Krüger, obtained with VCCT [9]. The maximum cyclic displacement is 0.67 mm on each arm, thus a total opening displacement of 1.34 mm with a load ratio of 0.1. The final displacement of the specimen is shown in Figure 6.8

Figure 6.8: Final displacement of the DCB specimen in the fatigue analysis.

Figure 6.9 shows the resulting crack length versus the number of cycles of the DCB specimens from the different analyses. A quantitative comparison of the data is shown in Table 6.3. The crack length is obtained through a Python script. This script checks each cohesive element where the damage parameter is equal to one. When this condition is met, the specific element has failed. All the failed elements are counted and multiplied by the element width. For the 2D model this results in the delamination length. For the 3D model, this number is divided by the number of elements through the width of the specimen to obtain the average crack length over the width of the crack front. Since the analysis uses pseudo-time, the number of cycles is equal to the time increment from the analysis. Note that the benchmark results have an initial crack length of 30 mm instead of 30.5 mm due to the large mesh size that was used here. The results are also compared to the analytical solution. This solution is obtained with the equations that are mentioned in Section 4.3.2.

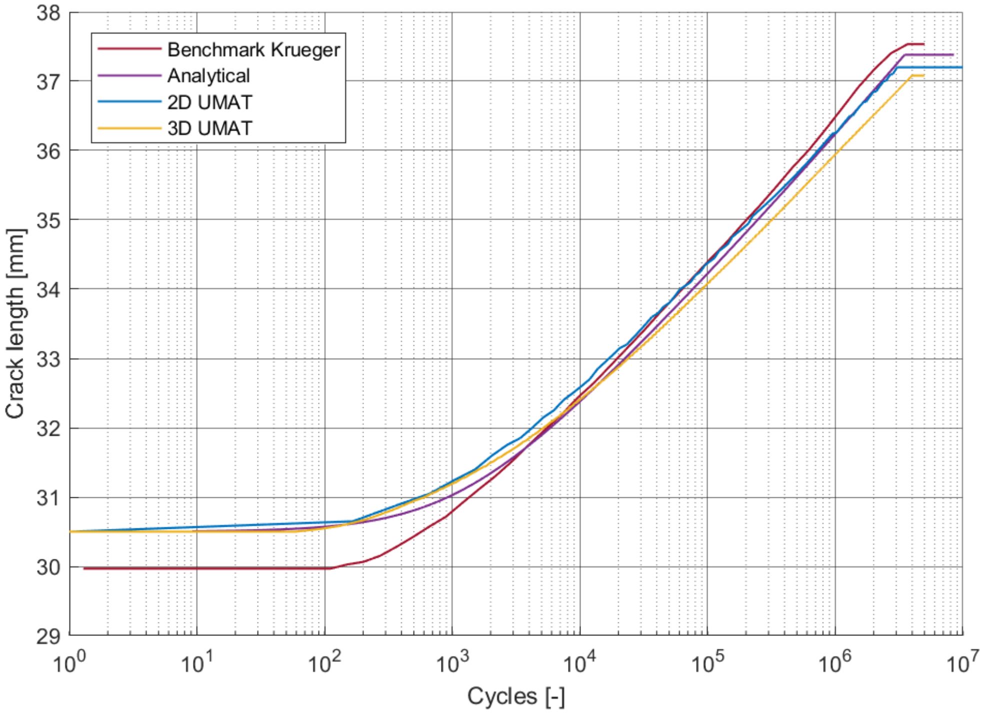

Figure 6.9: Crack length vs number of cycles of the DCB specimen.

Table 6.3: Final crack length of the DCB specimen compared to the benchmark data by Krüger [52] and the analytical solution.

	Final crack length [mm]	Difference [%]
Benchmark	37.53	-
2D UMAT	36.70	2.22
3D UMAT	36.58	2.54
Analytical	37.38	-
2D UMAT	36.70	1.82
3D UMAT	36.58	2.15

The crack growth curve shows that the crack onset of the UMAT is at a slightly lower cycle count than the benchmark. Crack propagation is slower for the UMAT results, and the final crack length is lower for all the analyses compared to the benchmark. This might be due to the shape of the crack front. Figure 6.10 shows the delamination front at three different stages in the analysis. The crack front has a curved shape where the crack at the edges is shorter than in the middle of the specimen. In the analyses that were preformed, the crack length was calculated by taking the average length over the whole crack front. It is not known how these calculations where performed in the Krüger benchmark, but it can be assumed that here the maximal crack length, thus at the centre element was taken.

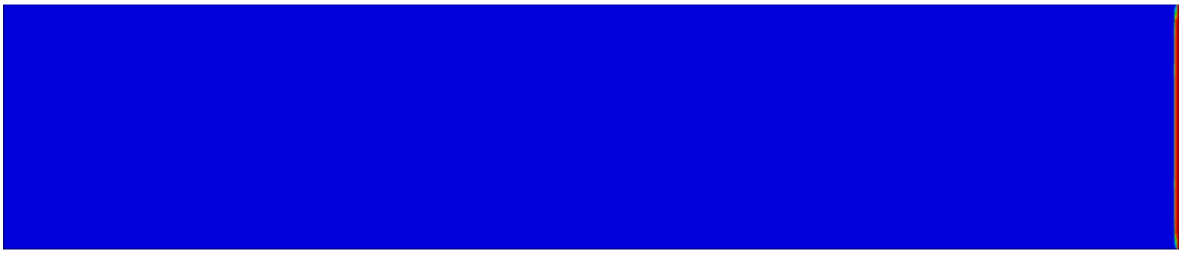

(a) Start of the fatigue loading.

(b) After 1.5e5 cycles.

(c) Final delamination after 5e6 cycles.

Figure 6.10: Delamination length at different stages during the fatigue analysis of the DCB specimen.

In the figures of the crack front (Figure 6.10), the damage variable is plotted. In the blue area, the damage variable is zero, which means that these elements are not affected by the loading. The red area represents a damage variable of one, so these are the elements that have failed. In Figure 6.10a the crack has not grown beyond the initial crack length. In Figures 6.10b and 6.10c, a vertical black line represents the location of the initial crack. Looking at the different stages of the crack front, it is seen that at the start of the fatigue loading, there are already some damaged elements. However, there are no elements that have already failed.

For validation purposes, the obtained Paris relation is shown in Figure 6.11. A comparison of the data to the material parameters is shown in Table 6.4. For this graph, the SERR is computed with the compliance of the specimen, according to the procedure outlined in Chapter 4. The crack growth rate is obtained by dividing the increase in crack length by the increase in cycle count for each time increment.

The 2D and 3D analyses show the same behaviour and show a good comparison to each other, but some differences with the benchmark can be identified. The upper limit of the SERR is not equal to the critical value. The applied displacement is 80% of the static failure displacement, therefore it is expected that the maximum value of the SERR is 80% of the critical value. The threshold SERR is a bit higher in the numerical analyses than the theoretical value. This can

Table 6.4: Strain Energy Release Rate data of the DCB specimen compared to the material parameters.

	G_{th}	Difference [%]	G_{max}	Difference[%]
Material parameters	0.06	-	0.136	-
2D UMAT	0.062	3.28	0.126	7.05
3D UMAT	0.061	1.34	0.123	9.24

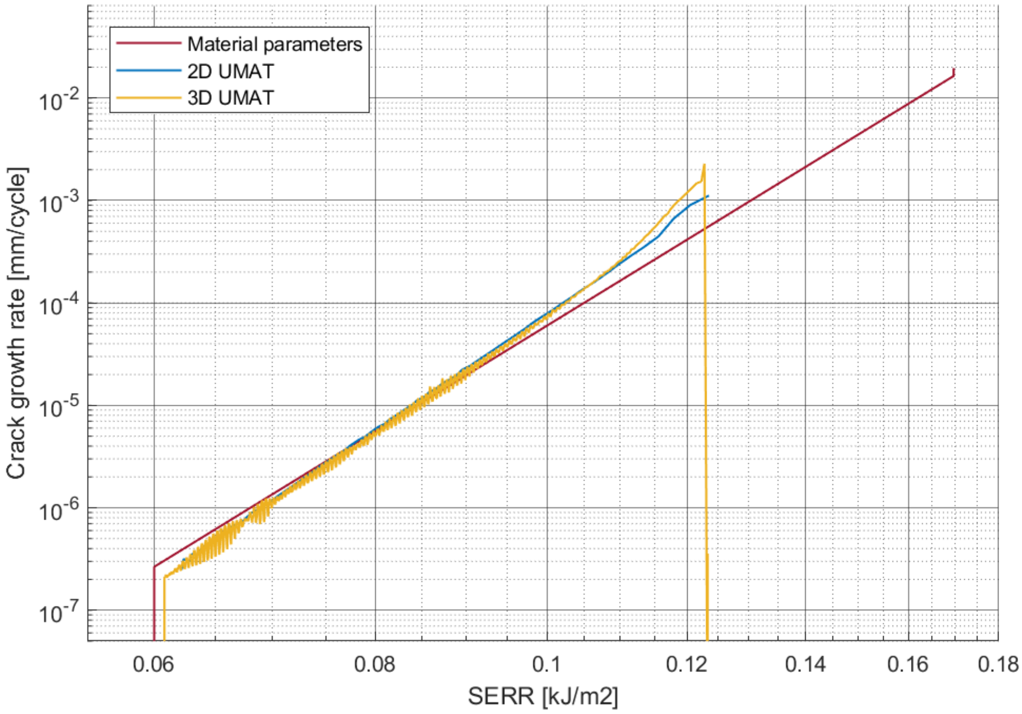

Figure 6.11: The obtained Paris relation for the DCB specimen.

be attributed to the discrete nature of FE computations. When an element fails, the SERR at the crack tip shows a sudden drop. Then the SERR builds up in the next element, until that fails, then this procedure repeats as the crack grows. If the SERR at the crack tip would be plotted as a function of the number of cycles, a saw tooth pattern would show. An example of this can be seen in Figure 4.3. This means that when the last element in the analysis fails, the SERR suddenly drops below the threshold, which is not possible, therefore the previous crack location is taken to be the final crack front, but the SERR is slightly higher than the theoretical threshold. Using a smaller element size would results in a smaller difference. This can be seen in Figure 6.12. The results in this graph were obtained with the same DCB specimen with element sizes of 0.05 mm and 0.005 mm in the cohesive zone.

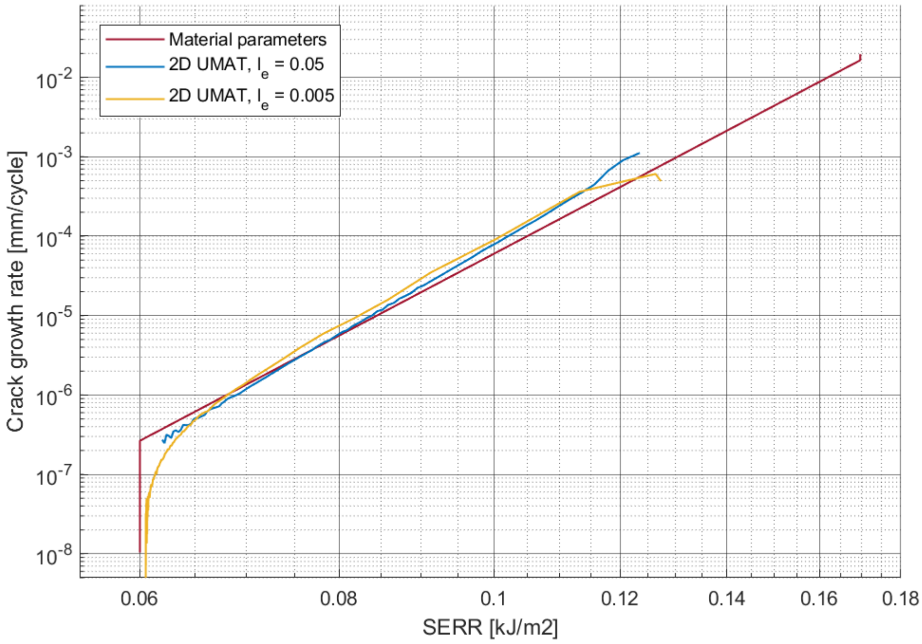

Figure 6.12: The obtained Paris relation for the 2D DCB specimen with 2 different element sizes.

Table 6.5: Strain Energy Release Rate data of the 2D DCB specimen with different element sizes compared to the material parameters.

	G_{th}	Difference[%]
Material parameters	0.06	-
$l^e = 0.05$ mm	0.062	3.28
$l^e = 0.005$ mm	0.06	0.85

In Table 6.5, the obtained threshold SERR is compared to the material data for the two DCB specimens with different element sizes. It is seen that the smaller element size does result in a smaller difference for the threshold SERR, however this also results in an increase in the computational time. Therefore, the element size was kept to 0.05 mm.

6.2 Mixed-Mode Bending (MMB) specimen

The MMB specimen is used to assess the mixed-mode bending behaviour of the material. In this project it was used for in both static and fatigue analyses. Both analyses were performed with two different mixed-mode ratios of 20 and 50%. The specimens have an initial crack and a controlled displacement is applied on the end of the loading arm to open the crack. The different mixed-mode ratios are achieved with different loading arm lengths.

6.2.1 Static results

The displacement profile of the 2D MMB specimen is shown in Figure 6.13 and of the 3D MMB specimen in Figure 6.14. These results are obtained with the UMAT.

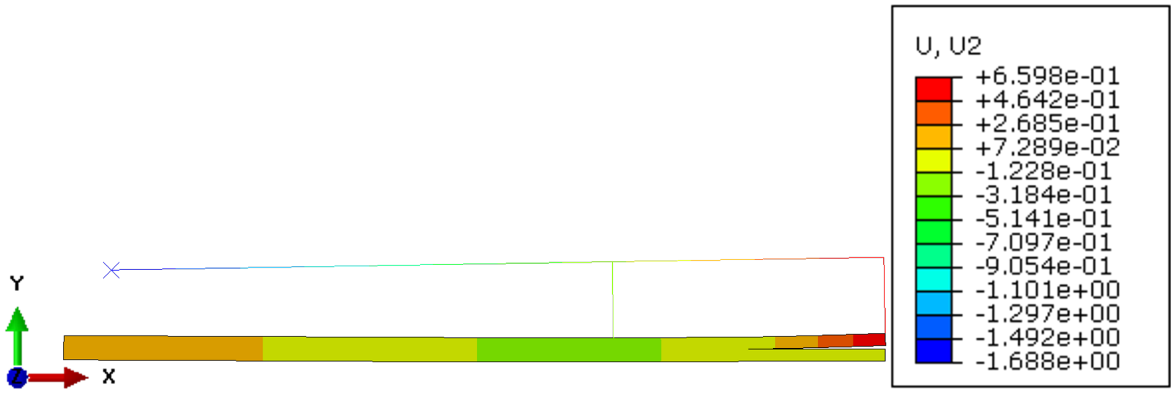

(a) Opening displacement of 1.67 mm.

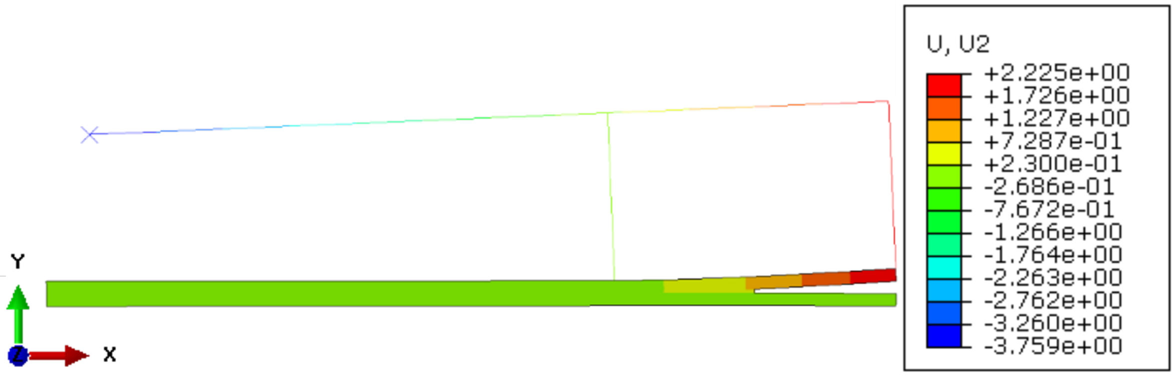

(b) Opening displacement of 3.75 mm.

Figure 6.13: Displacement profile of the 2D MMB specimen with $G_{II}/G_T = 0.2$ at two different opening displacements obtained with the UMAT during the static analysis.

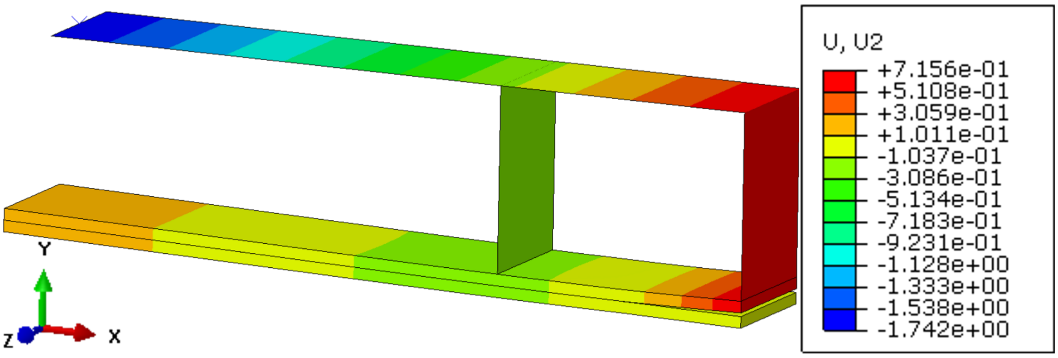

(a) Opening displacement of 1.74 mm.

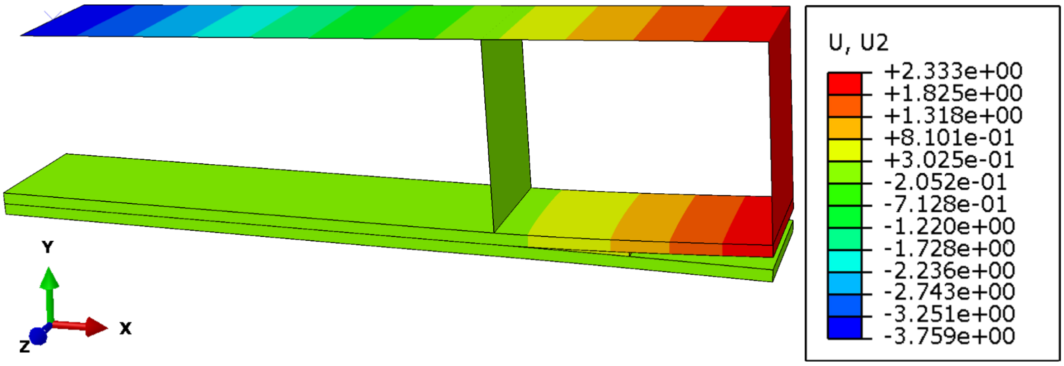

(b) Opening displacement of 3.76 mm.

Figure 6.14: Displacement profile of the 3D MMB specimen with $G_{II}/G_T = 0.2$ at two different opening displacements obtained with the UMAT during the static analysis.

The results for 20% mode mixity are shown in Figure 6.15. A quantitative overview of the data is given in Table 6.6. In this case, the opening displacement is defined as the downwards displacement of the tip of the lever arm. The reaction force is also taken at this point.

Table 6.6: Critical force and displacement for the MMB static analyses with $G_{II}/G_T = 0.2$ compared to the benchmark by Krüger [9].

	Critical force [N]	Difference [%]	Critical displacement [mm]	Difference [%]
Benchmark Krüger [9]	129.53	-	1.64	-
2D Abaqus	130.80	0.98	1.77	7.46
2D UMAT	126.20	2.60	1.75	6.50
3D Abaqus	128.31	0.94	1.84	11.59
3D UMAT	123.81	4.51	1.75	6.50

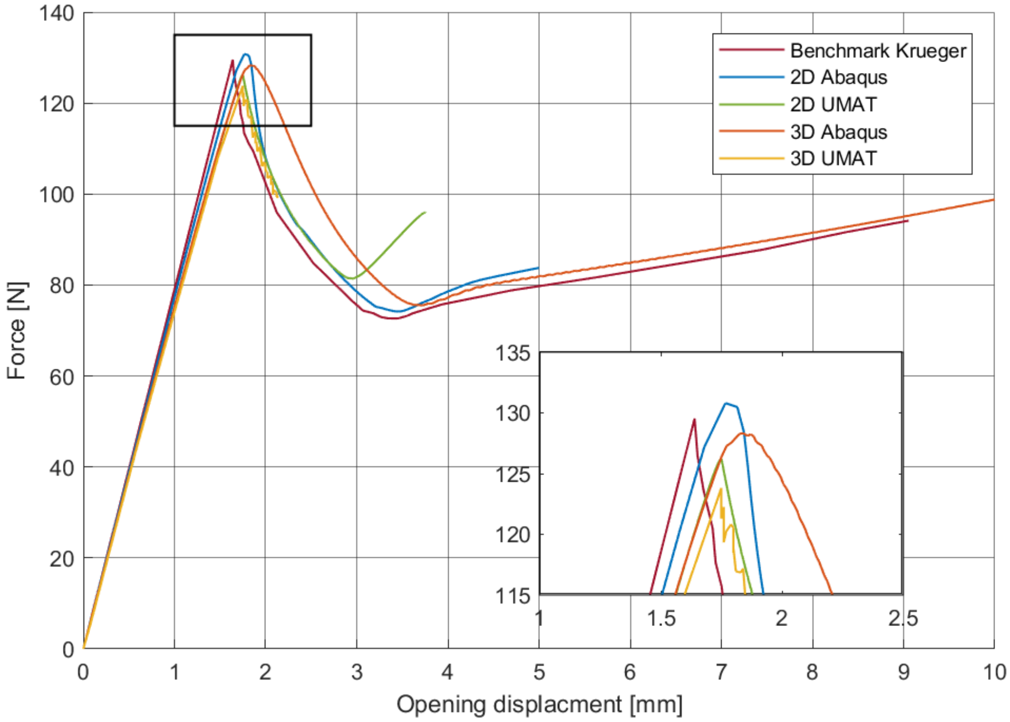

Figure 6.15: Force-displacement curve for the static analyses of the MMB specimen with $G_{II}/G_T = 0.2$.

In the force-displacement graph it can be seen that the initial stiffness of the model is estimated correctly. For the most part all the results coincide before static failure occurs. However, at the point of static failure, it can be seen that the computed stiffness of the specimens is lower compared to the benchmark case.

The crack front of the 3D MMB specimen with 20% mode-mixity at two different opening displacements can be seen in Figure 6.16.

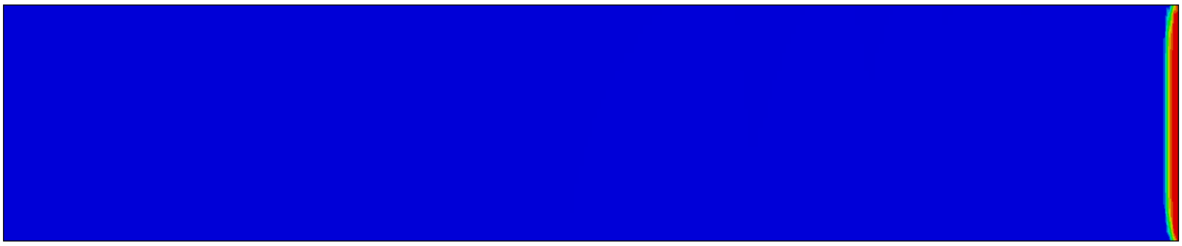

(a) Opening displacement of 1.74 mm.

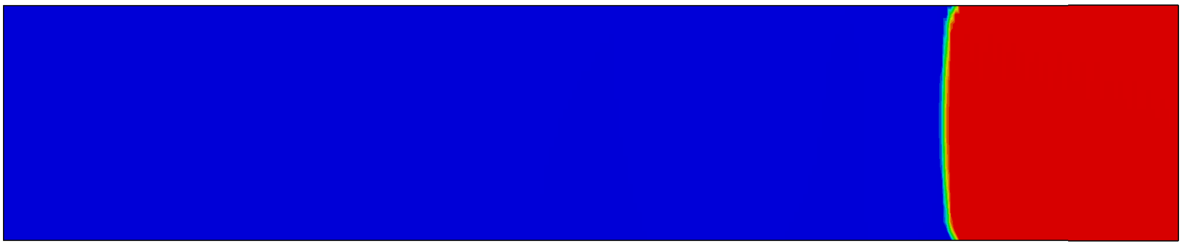

(b) Opening displacement of 3.76 mm.

Figure 6.16: Crack front of the 3D MMB specimen with $G_{II}/G_T = 0.2$ at two different opening displacements obtained with the UMAT during the static analysis.

The displacement profile of the MMB specimen with a mode-mixity of 50% at two different opening displacements can be seen in Figure 6.17

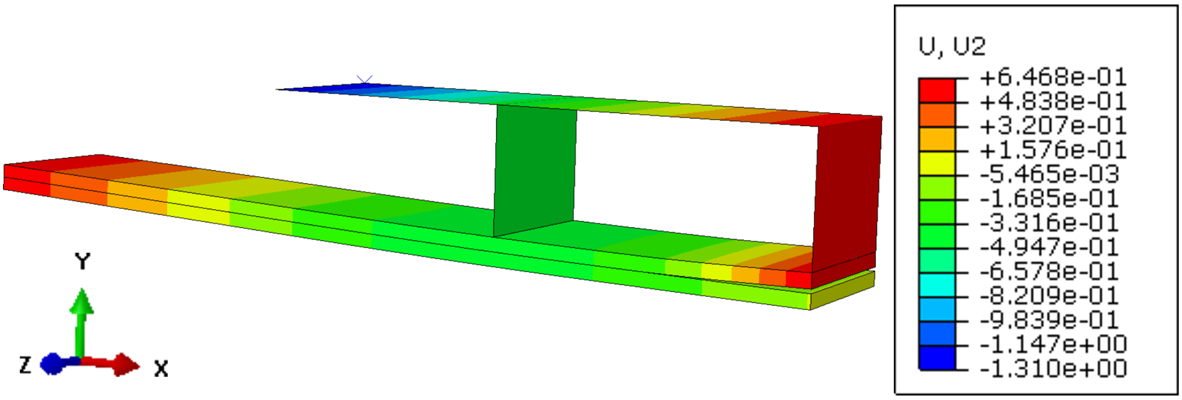

(a) Opening displacement of 1.31 mm.

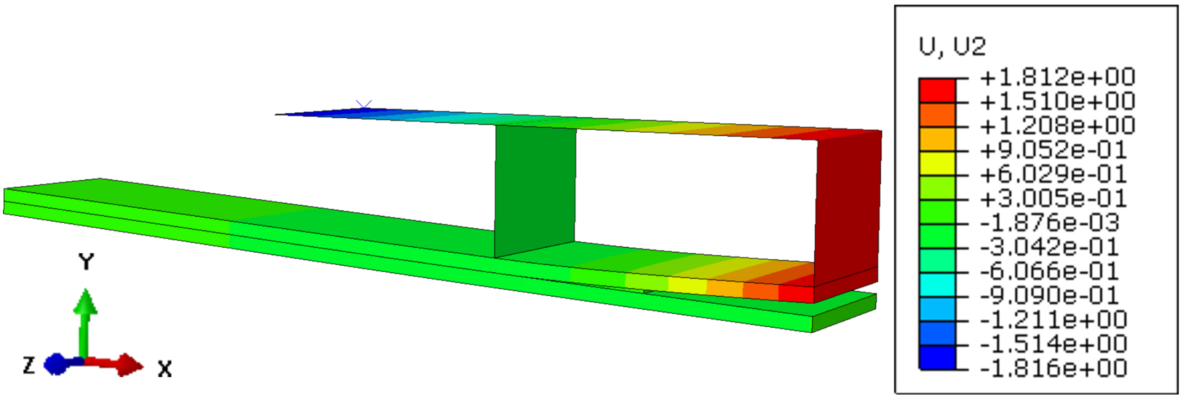

(b) Opening displacement of 1.8 mm.

Figure 6.17: Displacement profile of the 3D MMB specimen with $G_{II}/G_T = 0.5$ at two different opening displacements obtained with the UMAT during the static analysis.

The static results are shown in Figure 6.18.The critical force and displacement as well as the differences to the benchmark are shown in Table 6.7. The behaviour until the point of failure is represented well. The computed failure load of the specimens is lower compared to the benchmark.

Table 6.7: Critical force and displacement for the MMB static analyses with $G_{II}/G_T = 0.5$ compared to the benchmark by Krüger [9].

	Critical force [N]	Difference [%]	Critical displacement [mm]	Difference [%]
Benchmark Krüger [52]	384.00	-	1.37	-
2D Abaqus	368.76	4.05	1.38	0.53
2D UMAT	357.95	7.02	1.31	4.67
3D Abaqus	354.65	7.95	1.33	3.39
3D UMAT	353.59	8.24	1.31	4.66

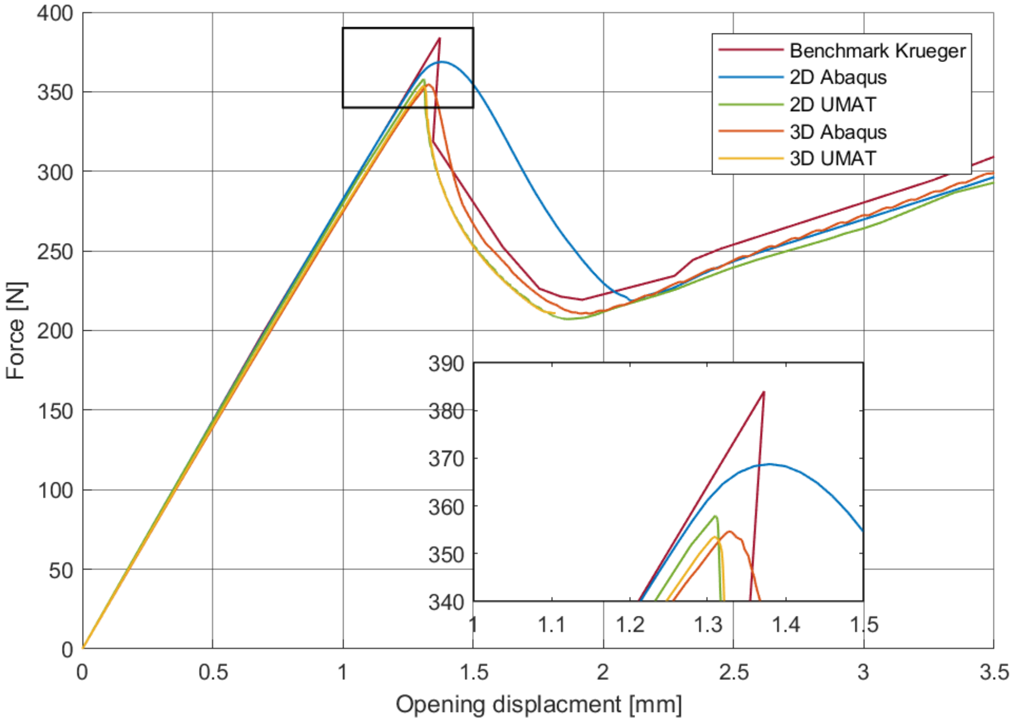

Figure 6.18: Force-displacement curve for the static analyses of the MMB specimen with $G_{II}/G_T = 0.5$.

When the crack has grown up to the point where the upper loading fixture touches the specimen, the stiffness of the specimen increases as the loading fixture provides a downward load. This downward load closes the crack. This corresponds to an opening displacement of around 3 mm for the 20% mode-mixity and 2 mm for 50% mode-mixity. The resultant stiffness of the benchmark case is higher than the current analyses, but the difference is only minor, so this can be neglected in this case as it is a result of slightly different boundary conditions for the upper fixture.

The crack front at two different opening displacements of the MMB specimen with 50% mode-mixity can be seen in Figure 6.19.

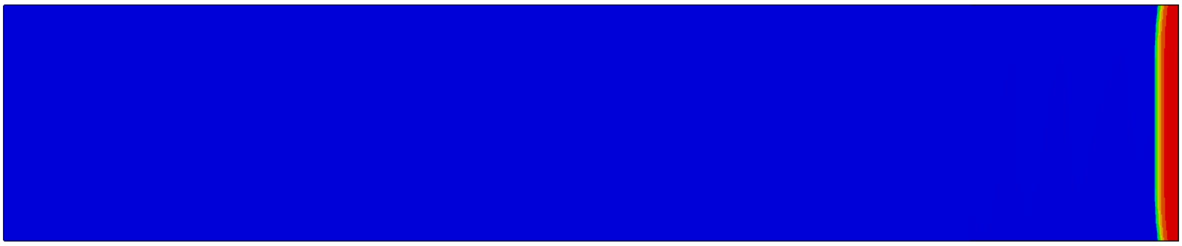

(a) Opening displacement of 1.31 mm.

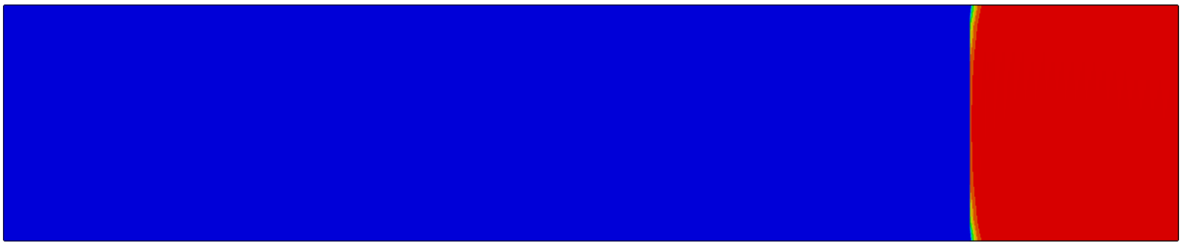

(b) Opening displacement of 1.8 mm.

Figure 6.19: Crack front of the 3D MMB specimen with $G_{II}/G_T = 0.5$ at two different opening displacements obtained with the UMAT during the static analysis.

6.2.2 Fatigue results

The fatigue analyses of the MMB are carried out with the same specimen as the static analyses. For the fatigue analysis the maximum cyclic lever displacement is 1.27 mm and 1.04 mm for G_{II}/G_T of 0.2 and 0.5 respectively with a load ratio of 0.1 for both specimens. The computed results are compared to the crack growth graph and the Paris relation from the benchmark case by Krüger [53].

The final displacement of the MMB specimen with 20% mode-mixity is shown in Figure 6.20.

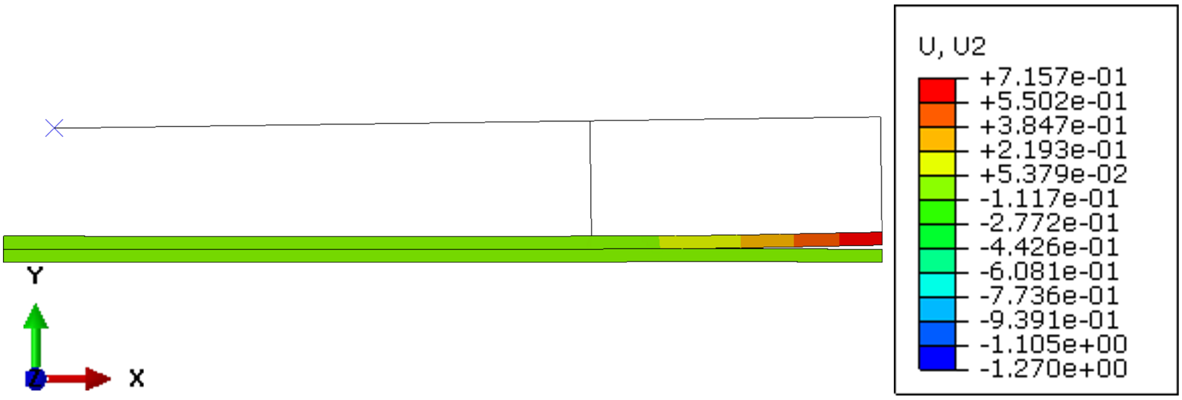

Figure 6.20: Final displacement of the MMB specimen with $G_{II}/G_T = 0.2$ during the fatigue analysis.

The crack growth data for the specimens with a mode-mixity of 20% is presented in Figure 6.21. In Table 6.8, a quantitative comparison with the benchmark is presented.

Table 6.8: Final crack length of the MMB specimen with $G_{II}/G_T = 0.2$ compared to the benchmark by Krüger [53] and the analytical solution.

	Final crack length [mm]	Difference [%]
Benchmark	39.889	-
2D UMAT	39.889	0.03
3D UMAT	39.887	0.03
Analytical	39.897	-
2D UMAT	39.889	0.01
3D UMAT	39.887	0.02

When comparing the data to the benchmark, it shows that the benchmark data predicts the onset of fatigue damage to occur later than the subroutine.

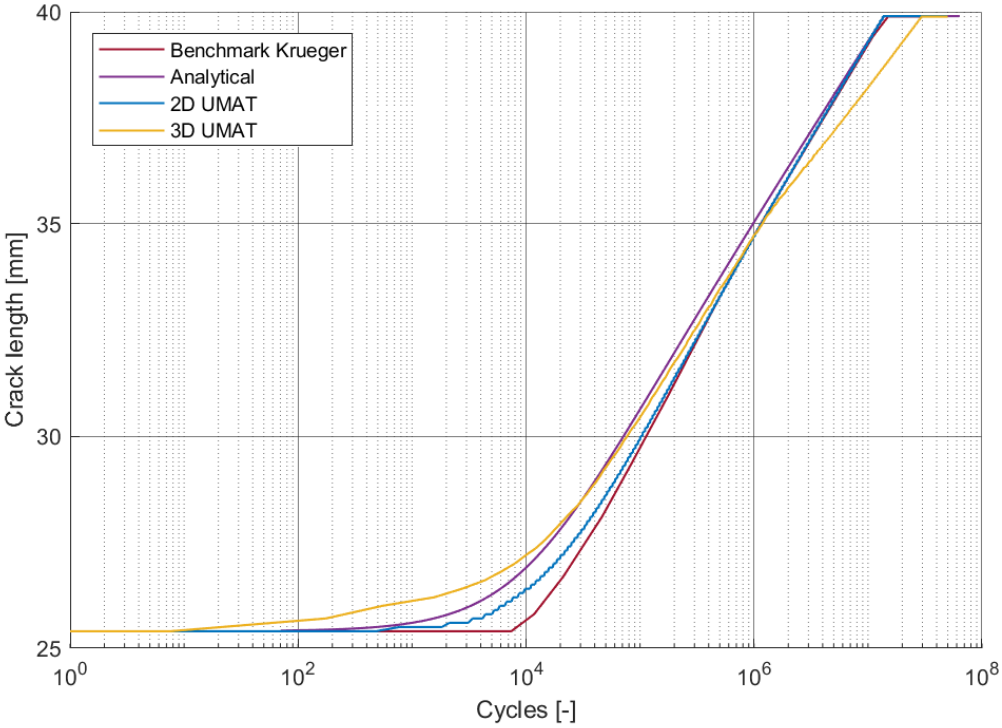

Figure 6.21: Delamination growth curve for the 2D MMB specimen with a $G_{II}/G_T = 0.2$.

The Paris relation for the MMB specimen with 20% mode-mixity is shown in Figure 6.22. The quantitative comparison is shown in Table 6.9.

Table 6.9: Strain Energy Release Rate data of the MMB specimen with $G_{II}/G_T = 0.2$ compared to the material parameters.

	G$_{th}$	Difference [%]	G$_{max}$	Difference[%]
Material parameters	0.060	-	0.136	-
2D UMAT	0.061	1.4	0.143	4.7
3D UMAT	0.059	1.5	0.137	0.3

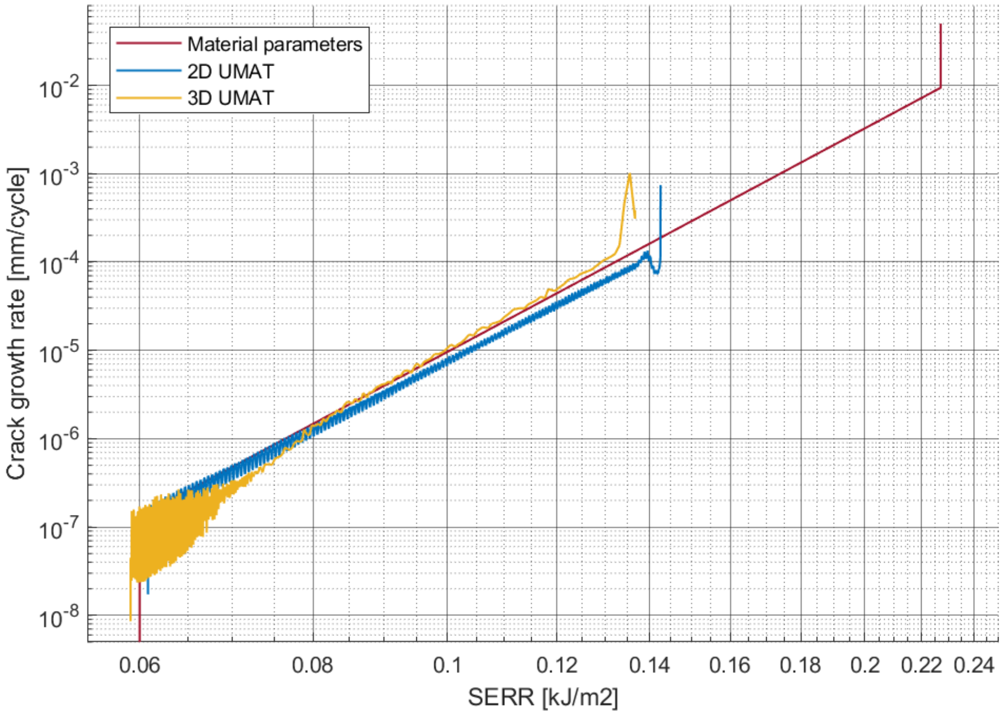

Figure 6.22: Paris relation for the 2D MMB specimen with a $G_{II}/G_T = 0.2$.

The obtained Paris relation shows good comparison to the material parameters. Similar to the DCB specimen, the final value of the SERR is slightly higher than the theoretical threshold. This can be attributed to the discrete nature of the finite element analysis. This difference would be smaller if the element size was reduced, but this would also greatly increase the computational time.

For the 3D specimen, a deviation from expected crack growth rate is seen. This happens at a cycle count of $10e6$ and a SERR of 0.08.

The crack front of the MMB specimen with a 20% mixed-mode ratio can be seen in Figure 6.23. These figures show the development of the damage variable during the analysis. The red area is completely damaged material and the blue area is completely undamaged. The initial crack location is shown with a vertical black line. Figure 6.23c shows a closer view of the crack front. The shape of the crack front does not resemble the expected finger nail shape that is seen in a coupon level fatigue analysis. It shows 5 different bulges that all have the same size. The width of the bulges is exactly the same as the width of 2 elements.

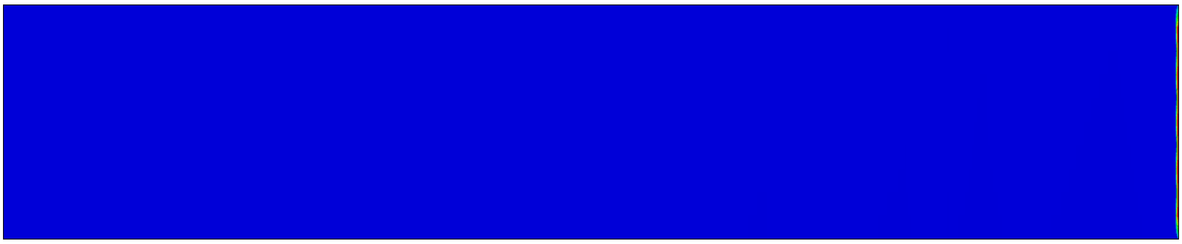

(a) Start of the fatigue loading.

(b) After 1.8e5 cycles.

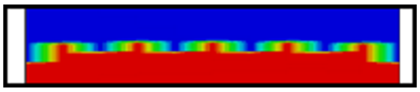

(c) Close-up of the crack front of the 3D MMB specimen with a $G_{II}/G_T = 0.2$.

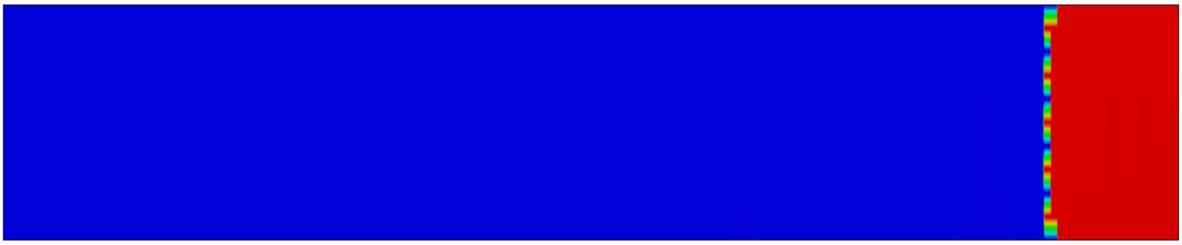

(d) Final delamination after 5e7 cycles.

Figure 6.23: Delamination length at different stages during the fatigue analysis of the MMB specimen with $G_{II}/G_T = 0.2$.

The final displacement for the MMB specimen with 50% mode-mixity is shown in Figure 6.24.

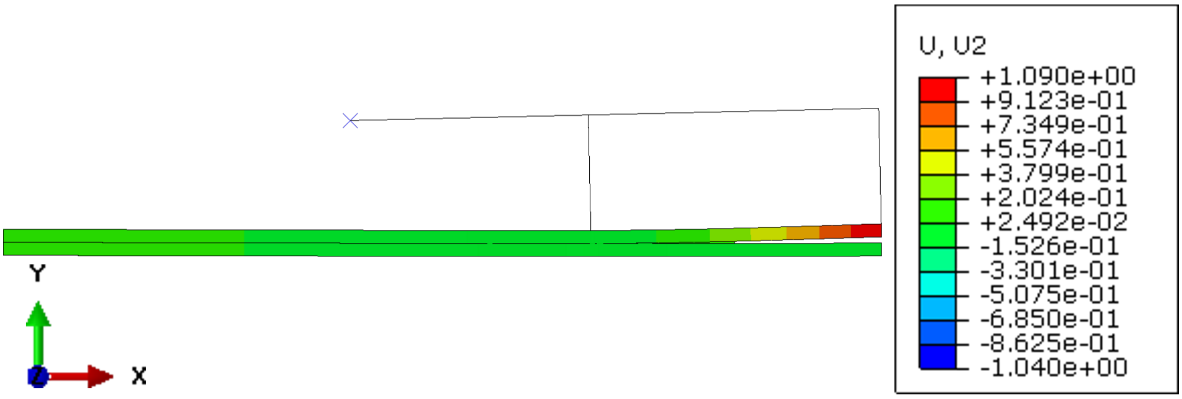

Figure 6.24: Final displacement of the MMB specimen during the fatigue analysis.

The delamination growth results for 50% mode-mixity are presented in Figure 6.25. The data is summarised in Table 6.10 and compared to the benchmark data.

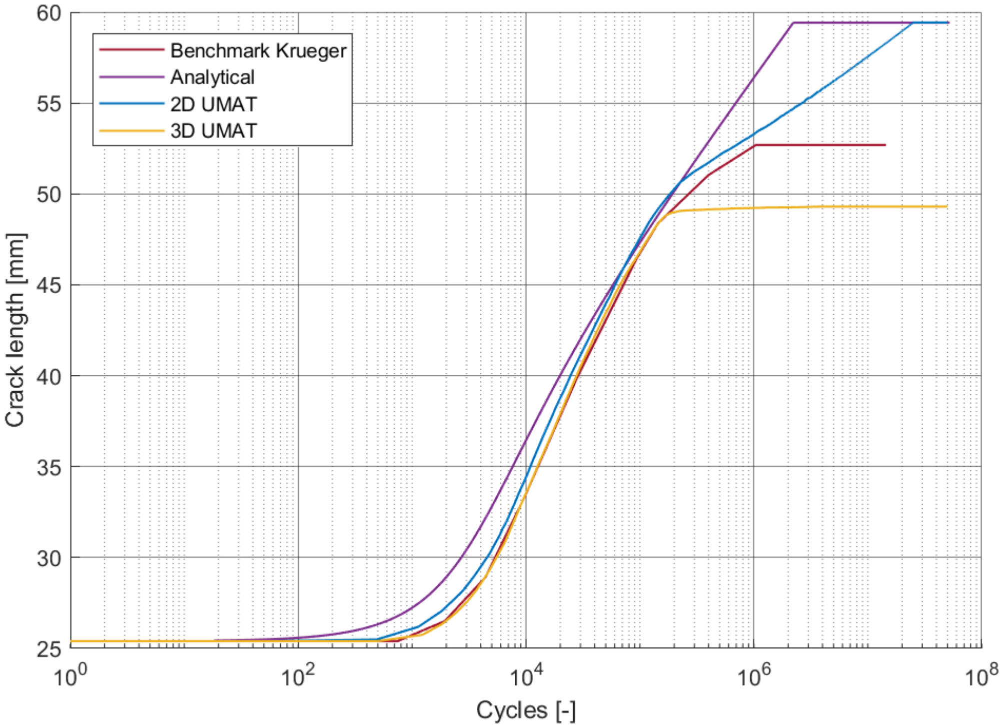

Figure 6.25: Delamination growth curve for the 2D MMB specimen with $G_{II}/G_T = 0.5$.

Table 6.10: Final crack length of the MMB specimen with $G_{II}/G_T = 0.5$ compared to the benchmark by Krüger [53] and the analytical solution.

	Final crack length [mm]	Difference [%]
Benchmark	52.7	-
2D UMAT	59.4	12.8
3D UMAT	49.3	6.4
Analytical	59.41	-
2D UMAT	59.42	0.013
3D UMAT	49.30	17.02

The number of cycles necessary for damage onset is predicted to be the same as for the benchmark. The crack propagation is also modelled adequately. Once the crack length exceeds 50.4 mm, all the results diverge. This is the point where the crack extends past the application point of the upper loading fixture. It was already seen in the static results that the LEFM calculations are not accurate beyond this crack length due to the downward force imposed by the fixture. The results from the benchmark test do not show a clear stagnation of the crack growth beyond this point. Instead, the graph is simply cut off at this point [53], therefore it is not clear whether the threshold SERR has been reached, thus making it difficult to compare this phase of the analysis to the subroutine results.

The obtained Paris relation for the 50% mode II is shown in Figure 6.26. The threshold and the maximum value of the SERR are compared in Table 6.11

Table 6.11: Strain Energy Release Rate data of the MMB specimen with $G_{II}/G_T = 0.5$ compared to the material parameters.

	G_{th}	Difference [%]	G_{max}	Difference[%]
Material parameters	0.060	-	0.194	-
2D UMAT	0.074	23.8	0.218	12.7
3D UMAT	0.096	60.7	0.217	12.0

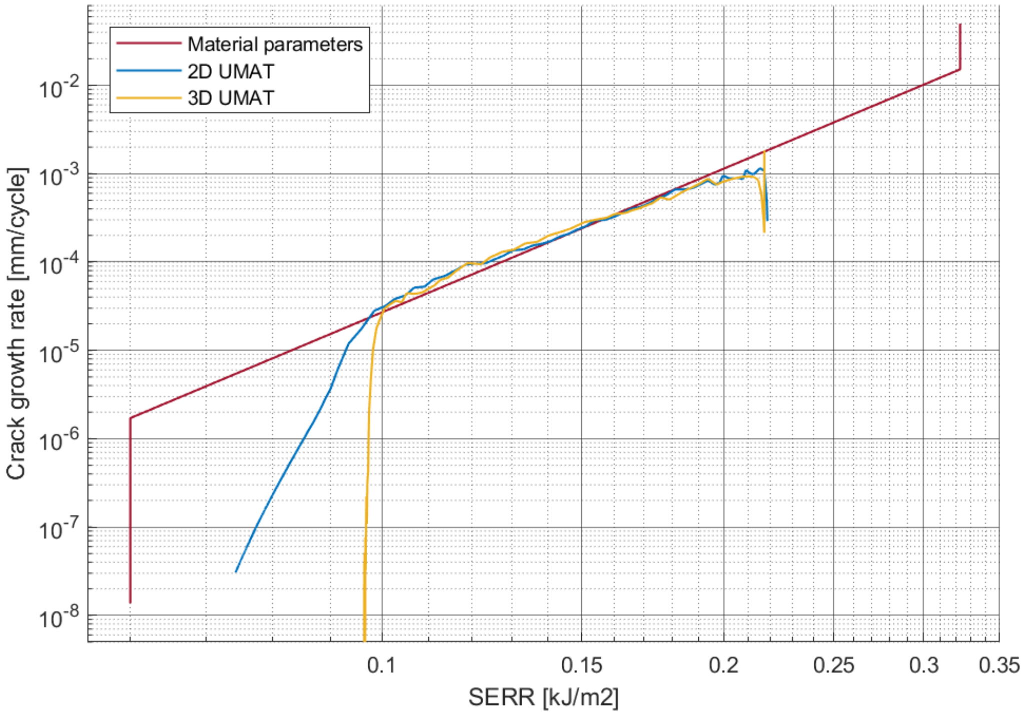

Figure 6.26: Paris relation for the 2D MMB specimen with a $G_{II}/G_T = 0.5$.

Good comparison can be seen at the start of the analysis, for high values of the SERR and crack growth rate. When the analysis progresses, the SERR decreases. Once the crack has grown beyond 50.4 mm, the analytical calculations based on the compliance no longer show a good comparison. This is similar to the results in Figure 6.25. Therefore, it is concluded that the used equations are not valid beyond this point of the crack growth. This test is used to characterize the mixed mode I/II behaviour of a structure. The purpose of the test is to gain knowledge on this behaviour on a coupon level that can be expanded to full size structures. When the crack has extended beyond this point, different loading conditions are present due to the crack closing effect of the fixture. Therefore, this behaviour is not representative for mixed-mode I/II behaviour, and can be ignored.

Different images of the crack front are presented in Figure 6.27

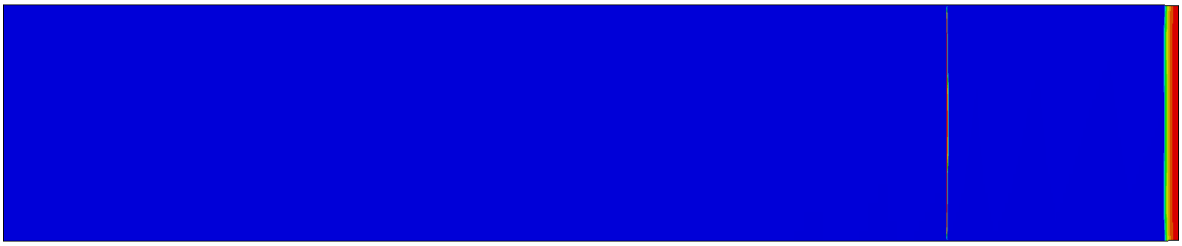

(a) Start of the fatigue loading.

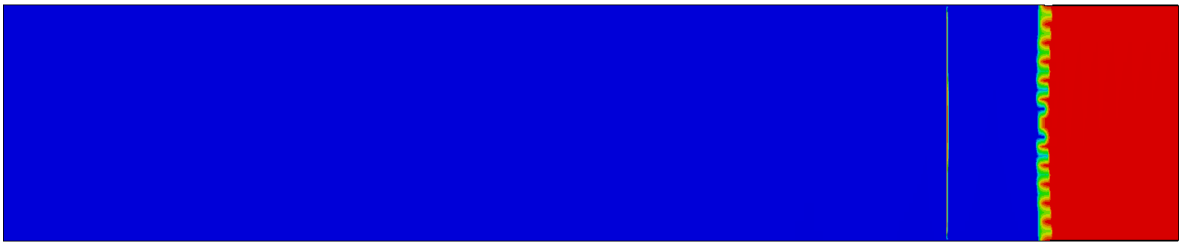

(b) After 2.3e4 cycles.

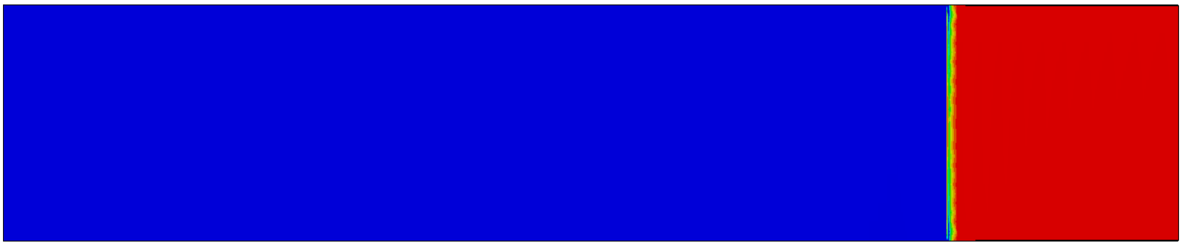

(c) Final delamination after 5e7 cycles.

Figure 6.27: Delamination length at different stages during the fatigue analysis of the MMB specimen with $G_{II}/G_T = 0.5$.

In the figures of the crack front, it can be seen that there is a line of damaged elements at the location where the upper fixture touches the specimen. This is caused by the stress concentration that results from the load application in this point. This stress concentration would be slightly resolved if more elements through the thickness of the specimen were used. This would also greatly increase the computational time. The stress concentration does not have a significant influence on the accuracy of the results.

Chapter 7

Conclusions and Recommendations

The purpose of this project was to assess the implementation of a cohesive zone model into a User Material (UMAT) for Abaqus. To improve the accuracy, several adaptations proposed in literature were implemented into the UMAT. To test this implementation, two different standardized specimens were used; the Double Cantilever Beam (DCB) specimen for pure mode I characterization and the Mixed-Mode Bending (MMB) specimen for mixed mode I and II characterization. Both specimens were subjected to static loading to verify the setup of the Finite Element (FE) model. Next, a fatigue analysis was performed and compared to a Virtual Crack Closure Technique (VCCT) benchmark. Both the static and fatigue analyses were performed with a 2D plane stress model and a full 3D model to compare the difference in accuracy. Once the behaviour of the coupon level is accurately predicted, the next step would be to expand the method to more complex assemblies such as skin stiffener specimens.

This chapter contains the conclusions that can be drawn from the project, starting with the static analyses. Secondly an overview of the adaptations is given followed by the summary of the fatigue analysis. Lastly some recommendations for future work are discussed.

7.1 Conclusions

For the static analyses for both the DCB and MMB specimens the critical failure point is determined accurately. The failure point of the DCB specimen is predicted with an error of less than 2.5%, while the MMB specimens show an error of 10% in some cases.. No significant differences can be seen in the 2D and 3D models with regard to the critical displacement under static loading. The analyses show a lower stiffness during the damage propagation when compared to the benchmark cases. This is most seen in the MMB case with a 20% mode ratio. The difference can be attributed to a different modelling of the loading fixture. Because the static loading was used as a model verification and the static failure point is accurately predicted, no further investigation was done into the difference in damage propagation. No modifications were necessary for the implementation of the theoretical model for static loading.

Several modifications to the theoretical fatigue model were necessary for a successful implementation into the UMAT. A flag parameter was included to take the fluctuating Strain Energy Release Rate (SERR) into account. The SERR steadily increases as damage builds up in an element with a sudden drop once the element fails. This would lead to an underestimation of the final crack length. By introducing a flag parameter, the SERR is only compared to the threshold value right before element failure which leads to a more accurate representation of the final crack length.

For an accurate analysis of mixed-mode loading, additional modifications were necessary. In this loading case the local SERR calculated by the Traction-Separation Law (TSL) differs from the global value because the mixed-mode ratio is not constant in the processing zone. This causes difficulties for the prediction of the final crack length since the SERR at the crack tip is lower than the global value. In the Paris relation, the global SERR should be used for an accurate predication. To solve this, the global SERR is computed using the Linear Elastic Fracture Mechanics (LEFM) equations based on the crack length.

To take the mixed-mode loading conditions into account, the penalty stiffness and the estimation of the cohesive zone area were adapted. The penalty stiffness was altered using the pure-mode interface strengths and critical SERR to determine a ratio that reduces the penalty stiffness for mode I. This results in a penalty stiffness for both shearing modes. For the estimation of the cohesive zone area, the mixed-mode interface strength is calculated using the mixed-mode ratio. Both of these adaptations results in a more versatile UMAT.

When looking at the results for the different fatigue analyses, it is seen that in all cases the predicted number of cycles to start fatigue crack growth is lower in the current models when compared to the benchmark cases. In the analysis of the DCB specimen, the onset point is 40% lower, but for the MMB specimens, the difference is almost 100%.

The damage propagation results for the fatigue loading cases show good comparison to the benchmark cases, with the exception of the MMB specimens with 50% mode-mixity when the crack grows beyond the sliding support of the loading fixture. The validity of the LEFM equations is limited to cases where the crack length does not reach the sliding support of the upper loading fixture. The loading case changes drastically when this happens, thus it is different from the intended loading case. Therefore the results beyond this point can be disregarded.

7.2 Recommendations

During the course of this project, some challenges and limitations were identified. For a successful expansion of the model to more complex structures, these should be taken into account.

Firstly, it is important to note that all the analysis in this report were performed with unidirectional 0 degree specimens. To draw conclusions on the general applicability of the model and to obtain a full overview of the behaviour of the model, different layups should be investigated. Furthermore it would be beneficial to perform analyses where the two substrates have different materials or different layups of the same materials.

Secondly, the cohesive zone model has a quite severe mesh density requirement. Mesh sizes of 0.05-0.1 mm are necessary to have enough elements in the cohesive zone. This has a big impact on the computational time. The DCB specimen for fatigue loading in this report has around 60.000 nodes. This can be considered a relatively simple geometry so to analyse more complex geometries, the required number of nodes will drastically increase, thus increasing the computational time necessary.

A third consideration is that the crack onset predicted by the UMAT is always earlier than the VCCT benchmarks. The onset phase is rather important in the lifetime of a structure since it is crucial for structural health monitoring and determining service intervals. More research is needed into this first phase of the damage process.

Fourthly, the calculation of the global SERR using LEFM equations is known for MMB specimens with a predetermined mixed-mode ratio. In more complex geometries and loading cases such as a buckled skin stiffener configuration, the mixed-mode ratio is not know beforehand and can change over the course of an analysis. There are no LEFM equations available to calculate the global SERR based on the compliance of such a structure. To solve this issue, a way has to be found to either obtain the global SERR, or to calculate the final crack length.

Lastly, to calculate the increase in fatigue damage based on the Paris relation, the cohesive zone length is an important parameter. There are a lot of different equations found in literature to calculate the cohesive zone length but almost all of them contain a constant parameter. In this project this parameter was determined by completing a static load analysis to find the real area of the cohesive zone and implementing that into the fatigue model. This is quite cumbersome and prone to errors so a better method for calculating the cohesive zone area should be developed. It would also be beneficial if the cohesive zone area can be calculated from only material and geometrical parameters such that no estimation of an extra constant is required.

Overall, the results show that the implementation of the theoretical model into a UMAT for the analysis of high-cycle fatigue is promising. The expansion of this model to bigger and more complex structures would lead to a better prediction of the delamination behaviour under fatigue loading of composite structures.

References

[1] C.G. Dávila and C. Bisagni. Fatigue life and damage tolerance of postbuckled composite stiffened structures with indentation damage. *Journal of Composite Materials*, 2018, 52 (7):931–943.

[2] C.G. Dávila and C. Bisagni. Fatigue life and damage tolerance of postbuckled composite stiffened structures with initial delamination. *Composite Structures*, 2017, 161:73–84.

[3] C. Bisagni, P. Brambilla, and C.G. Dávila. Modeling delamination in postbuckled composite structures under static and fatigue loads. In *SAMPE 2013 Conference and Exhibition*, pages 1035–1049, 2013.

[4] C. Bisagni and C.G. Dávila. Experimental investigation of the postbuckling response and collapse of a single-stringer specimen. *Composite Structures*, 2014, 108:493–503.

[5] J. Schijve. *Fatigue of Structures and Materials.* Springer, Delft, 2nd edition, 2008.

[6] R.D.S.G. Campilho and L.F.M. da Silva. Mode I fatigue and fracture behaviour of adhesively-bonded carbon fibre-reinforced polymer (CFRP) composite joints. In *Fatigue and Fracture of Adhesively-Bonded Composite Joints*, edited by A.P.. Vassilopoulos, pages 93–120. Woodhead Publishing, Cambridge, UK, 2015.

[7] J.R. Reeder. 3D mixed-mode delamination fracture criteria-an experimentalist's perspective. In *Damage in Composites*, edited by A.M.. Waas and B.V.. Sankar, volume 5, pages 129–146. DEStech Publications Inc, Lancaster, 2013.

[8] P.P. Camanho, CG. Dávila, and M.F. de Moura. Numerical simulation of mixed-mode progressive delamination in composite materials. *Journal of Composite Materials*, 2003, 37(16):1415–1438.

[9] R. Krueger. Development of a benchmark example for delamination fatigue growth prediction. *NASA/CR-2010-216723*, 2010.

[10] C. Sarrado, A. Turon, J. Renart, and I. Urresti. Assessment of energy dissipation during mixed-mode delamination growth using cohesive zone models. *Composites Part A: Applied Science and Manufacturing*, 2012, 43(11):2128–2136.

[11] M.L. Benzeggagh and M. Kenane. Measurement of mixed-mode delamination fracture toughess of unidirectional glass/epoxy composites with mixed-mode bending apparatus. *Composites Science and Technology*, 1996, 56(4):439–449.

[12] A. Turon, P.P. Camanho, J. Costa, and C.G. Dávila. A damage model for the simulation of delamination in advanced composites under variable-mode loading. *Mechanics of Materials*, 2006, 38(11):1072–1089.

[13] P. Paris and F. Erdogan. A critical analysis of crack propagation laws. *Journal of Basic Engineering*, 1963, 85(4):528–533.

[14] A.S.D. Wang, M. Slomiana, and R. Bucinell. *Delamination Crack Growth in Composite Laminates Delamination and Debonding of Materials*, pages 135–167. ASTM International, West Conshohocken, PA, 1985.

[15] W.C. de Goeij, M.J.L. van Tooren, and A. Beukers. Composite adhesive joints under cyclic loading. *Materials & Design*, 1999, 20(5):213–221.

[16] G.R. Irwin. Fracture. In *Elasticity and Plasticity/Elastizität und Plastizität*, edited by S. Flügge, pages 551–590. Springer, Berlin, 1958.

[17] R. Krueger. Virtual crack closure technique: History, approach, and applications. *Applied Mechanics Reviews*, 2004, 57(1-6):109–143.

[18] I.S. Raju. Calculation of strain-energy release rates with higher order and singular finite elements. *Engineering Fracture Mechanics*, 1987, 28(3):251 – 274.

[19] W. Brocks. The cohesive model. In *Solid Mechanics and its Applications*, volume 244, pages 151–170. Springer, Cham, Switzerland, 2018.

[20] A. Amiri-Rad and M. Mashayekhi. A cohesive zone approach for fatigue-driven delamination analysis in composite materials. *Applied Composite Materials*, 2017, 24(4): 751–769.

[21] A. Turon, C.G. Dávila, P.P. Camanho, and J. Costa. An engineering solution for mesh size effects in the simulation of delamination using cohesive zone models. *Engineering Fracture Mechanics*, 2007, 74(10):1665–1682.

[22] A.B. de Morais. Cohesive zone beam modelling of mixed-mode I-II delamination. *Composites Part A: Applied Science and Manufacturing*, 2014, 64:124–131.

[23] A. Riccio, A. Raimondo, G. Di Felice, and F. Scaramuzzino. A numerical procedure for the simulation of skin-stringer debonding growth in stiffened composite panels. *Aerospace Science and Technology*, 2014, 39:307–314.

[24] J-A. Pascoe, R. Alderliesten, and R. Benedictus. Methods for the prediction of fatigue delamination growth in composites and adhesive bonds - a critical review. *Engineering Fracture Mechanics*, 2013, 112-113:72–96.

[25] A. Tabiei and W. Zhang. Cohesive element approach for dynamic crack propagation: Artificial compliance and mesh dependency. *Engineering Fracture Mechanics*, 2017, 180: 23–42.

[26] Z. Yuan and J. Fish. Are the cohesive zone models necessary for delamination analysis? *Computer Methods in Applied Mechanics and Engineering*, 2016, 310:567–604.

[27] B. Yang, S. Mall, and K. Ravi-Chandar. A cohesive zone model for fatigue crack growth in quasibrittle materials. *International Journal of Solids and Structures*, 2001, 38(22): 3927–3944.

[28] O. Nguyen, E.A. Repetto, M. Ortiz, and R.A. Radovitzky. A cohesive model of fatigue crack growth. *International Journal of Fracture*, 2001, 110(4):351–369.

[29] H. Khoramishad, A.D. Crocombe, K.B. Katnam, and I.A. Ashcroft. Predicting fatigue damage in adhesively bonded joints using a cohesive zone model. *International Journal of Fatigue*, 2010, 32(7):1146–1158.

[30] A. Turon, J. Costa, P.P. Camanho, and C.G. Dávila. Simulation of delamination in composites under high-cycle fatigue. *Composites Part A: Applied Science and Manufacturing*, 2007, 38(11):2270–2282.

[31] D. Tumino and F. Cappello. Simulation of fatigue delamination growth in composites with different mode mixtures. *Journal of Composite Materials*, 2007, 41(20):2415–2441.

[32] A. Pirondi and F. Moroni. A progressive damage model for the prediction of fatigue crack growth in bonded joints. *The Journal of Adhesion*, 2010, 86(5-6):501–521.

[33] B.L.V. Bak, C. Sarrado, A. Turon, and J. Costa. Delamination under fatigue loads in composite laminates: A review on the observed phenomenology and computational methods. *Applied Mechanics Reviews*, 2014, 66(6):1–24.

[34] M. May and S.R. Hallett. A combined model for initiation and propagation of damage under fatigue loading for cohesive interface elements. *Composites Part A: Applied Science and Manufacturing*, 2010, 41(12):1787–1796.

[35] P.W. Harper and S.R. Hallett. A fatigue degradation law for cohesive interface elements - development and application to composite materials. *International Journal of Fatigue*, 2010, 32(11):1774–1787.

[36] M. May and S.R. Hallett. An advanced model for initiation and propagation of damage under fatigue loading - part I: Model formulation. *Composite Structures*, 2011, 93(9): 2340–2349.

[37] N. Blanco, E.K. Gamstedt, L.E. Asp, and J. Costa. Mixed-mode delamination growth in carbon-fibre composite laminates under cyclic loading. *International Journal of Solids and Structures*, 2004, 41(15):4219–4235.

[38] O. Shor and R. Vaziri. Adaptive insertion of cohesive elements for simulation of delamination in laminated composite materials. *Engineering Fracture Mechanics*, 2015, 146: 121–138.

[39] O. Shor and R. Vaziri. Application of the local cohesive zone method to numerical simulation of composite structures under impact loading. *International Journal of Impact Engineering*, 2017, 104:127–149.

[40] *ABAQUS/Standard User's Manual, Version 2017.* Simulia, 2017.

[41] C. Dávila. From S-N to the Paris law with a new mixed-mode cohesive fatigue model. *NASA/TP-2018-219838*, 2018.

[42] M.L. Falk, A. Needleman, and J.R. Rice. A critical evaluation of cohesive zone models of dynamic fracture. *Le Journal de Physique IV*, 2001, 11(PR5):43–50.

[43] A. Turon. An engineering solution for using coarse meshes in the simulation of delamination with cohesive zone models. *NASA/TM-2005-213547*, 2005.

[44] W. Van Paepegem and J. Degrieck. Fatigue degradation modelling of plain woven glass/epoxy composites. *Composites Part A: Applied Science and Manufacturing*, 2001, 32(10): 1433–1441.

[45] A. Turon, E.V. González, C. Sarrado, G. Guillamet, and P. Maimí. Accurate simulation of delamination under mixed-mode loading using a cohesive model with a mode-dependent penalty stiffness. *Composite Structures*, 2018, 184:506–511.

[46] A. Turon, J. Costa, P.P. Camanho, and P. Maimí. *Analytical and Numerical Investigation of the Length of the Cohesive Zone in Delaminated Composite Materials.* Springer Netherlands, Dordrecht, 2008.

[47] I. Di Memmo and C. Bisagni. Fatigue simulation for damage propagation in composite structures. In *Proceedings of the American Society for Composites -Thirty-second Technical Conference*, pages 1009–1019, 2017.

[48] M.F.S.F. De Moura and J.P.M. Gonçalves. Cohesive zone model for high-cycle fatigue of adhesively bonded joints under mode I loading. *International Journal of Solids and Structures*, 2014, 51(5):1123–1131.

[49] H. Truong, D. C. Lagoudas, O. Ochoa, and K. Lafdi. Fracture toughness of fiber metal laminates: Carbon nanotube modified ti - polymer matrix composite interface. *Journal of Composite Materials*, 2013, 48(22):2697–2710.

[50] E.V. González, P. Maimí, A. Turon, P.P. Camanho, and J. Renart. Simulation of delamination by means of cohesive elements using an explicit finite element code. *Computers, Materials and Continua*, 2009, 9(1):51–92.

[51] J.R. Reeder. Refinements to the mixed-mode bending test for delamination toughness. *Journal of Composites, Technology and Research*, 2003, 25(4):1–5.

[52] R. Krueger. Development and application of benchmark examples for mixed-mode I/II quasi-static delamination propagation predictions. *NASA/CR-2012-217562*, 2012.

[53] R. Krueger and N. De Carvalho. In search of a time efficient approach to crack and delamination growth predictions in composites. In *Proceedings of the American Society for Composites: Thirty-First Technical Conference*, 2016.

Appendix A

Subroutine for Static Loading

```
SUBROUTINE UMAT(STRESS,STATEV,DDSDDE,SSE,SPD,SCD,
1 RPL,DDSDDT,DRPLDE,DRPLDT,
2 STRAN,DSTRAN,TIME,DTIME,TEMP,DTEMP,PREDEF,DPRED,CMNAME,
3 NDI,NSHR,NTENS,NSTATV,PROPS,NPROPS,COORDS,DROT,PNEWDT,
4 CELENT,DFGRD0,DFGRD1,NOEL,NPT,LAYER,KSPT,JSTEP,KINC)

INCLUDE 'ABA_PARAM.INC'

CHARACTER*80 CMNAME, CPNAME
DIMENSION STRESS(NTENS),STATEV(NSTATV),
1 DDSDDE(NTENS,NTENS),DDSDDT(NTENS),DRPLDE(NTENS),
2 STRAN(NTENS),DSTRAN(NTENS),TIME(2),PREDEF(1),DPRED(1),
3 PROPS(NPROPS),COORDS(3),DROT(3,3),DFGRD0(3,3),DFGRD1(3,3),
4 JSTEP(4)

DIMENSION CFULL(NTENS,NTENS), DELTAT(NTENS)
DOUBLE PRECISION KK, SIGMA3C, TAU1C, TAU2C, G1C, G2C, G3C, ...
    ETA
DOUBLE PRECISION DMG_OLD, DMG, BETA, BI, DELTA, DELTA1, ...
    DELTA2
DOUBLE PRECISION DELTA_SHEAR, DELTA0_3, DELTA_0SHEAR
DOUBLE PRECISION DELTA0, DELTAF, RT_OLD, RT, DELTA3
DOUBLE PRECISION CF6,CF7,CF5,CF4,KSH,KB,TAU

PAREMETER(ZERO=0.D0, ONE=1.D0, TWO=2.D0, THREE=3.D0)

KK          = PROPS(1)
SIGMA3C     = PROPS(2)
```

```
TAU1C      = PROPS(3)
TAU2C      = PROPS(4)
G1C        = PROPS(5)
G2C        = PROPS(6)
G3C        = PROPS(7)
ETA        = PROPS(8)

DMG_OLD = STATEV(1)

!DISPLACEMENT AT THE END OF THE INCREMENT
DO I = 1, NTENS
    DELTAT(I) = STRAN(I) + DSTRAN(I)
END DO

DELTA3 = DELTAT(1)
DELTA1 = DELTAT(2)
!IF THE ANALYSIS IS IN 2D: DELTA2 IS ZERO, IF IT IS 3D: ...
   DELTA2 IS THE THIRD ELEMENT
IF (NTENS.EQ.TWO) THEN
    DELTA2 = ZERO
ELSE
    DELTA2 = DELTAT(3)
ENDIF

DELTA_SHEAR = SQRT(DELTA1**2+DELTA2**2)

!SHEAR MODE PENALTY STIFFNESS
KSH = G1C/G2C*(TAU2C/SIGMA3C)**2*KK
!MIXED-MODE RATIO WITH SHEAR PENALTY STIFFNESS
CF6 = KSH*DELTA_SHEAR**2 + KK*MAX(DELTA3,ZERO)**2
CF7 = KSH**2*DELTA_SHEAR**2 + KK**2*MAX(DELTA3,ZERO)**2
BI= (KSH*DELTA_SHEAR**2)/CF6
!Mixed-mode penalty stiffness
KB = KK*(ONE-BI)+KSH*BI
!DISPLACEMENT JUMP NORM
DELTA = CF6/SQRT(CF7)
!PURE MODE ONSET DISPLACEMENT JUMP
DELTA_0SHEAR = TAU1C/KSH
DELTA0_3 = SIGMA3C/KK
!MIXED-MODE ONSET DISPLACEMENT JUMP
CF4 = (KSH*DELTA_0SHEAR**2-KK*DELTA0_3**2)*(BI**ETA)
DELTA0=SQRT((KK*DELTA0_3**2+CF4)/(KB))
!MIXED-MODE FINAL DISPLACEMENT JUMP
DELTAC_SHEAR = TWO*G2C/TAU1C
DELTAC_3 = TWO*G1C/SIGMA3C
CF5 = (KSH*DELTA_0SHEAR*DELTAC_SHEAR-KK*DELTA0_3*DELTAC_3)
DELTAF = (KK*DELTA0_3*DELTAC_3+CF5*(BI**ETA))/(KB*DELTA0)
```

```
!INTERNAL VARIABLE
RT_OLD = (DELTA0*DELTAF)/(DELTAF-DMG_OLD*(DELTAF-DELTA0))
RT = MAX(RT_OLD,DELTA)
IF (DELTA.GT.RT_OLD) THEN
    DMG = (DELTAF*(RT-DELTA0))/(RT*(DELTAF-DELTA0))
    DMG = MIN(DMG,ONE)
ELSE
    DMG = DMG_OLD
ENDIF

!FULL STIFFNESS MATRIX
DO I = 1, NTENS
    DO J = 1, NTENS
        CFULL(I,J)=ZERO
    END DO
END DO

IF (DELTA3.GE.ZERO) THEN
    CFULL(1,1) = KK*(ONE-DMG)
ELSE
    CFULL(1,1) = KK
ENDIF
CFULL(2,2) = KSH*(ONE-DMG)
!CFULL(3,3) ONLY EXISTS IN 3D
IF (NTENS.EQ.THREE) THEN
    CFULL(3,3) = KSH*(ONE-DMG)
ENDIF


!STRESS CALCULATION
DO I = 1, NTENS
    STRESS(I)=ZERO
    DO J = 1, NTENS
        STRESS(I)=STRESS(I)+CFULL(I,J)*DELTAT(J)
    END DO
END DO

!TANGENT STIFFNESS MATRIX
DO I = 1, NTENS
    DO J = 1, NTENS
        DDSDDE(I,J)=ZERO
    END DO
END DO

IF (DELTA.GT.RT_OLD.AND.DELTA.LT.DELTAF) THEN
    COEFF = ((DELTAF*DELTA0)/((DELTAF-DELTA0)*DELTA**3))
    IF (DELTA3.GE.ZERO) THEN
```

```
        DDSDDE(1,1) = CFULL(1,1)-KK*COEFF*DELTA3**2
    ELSE
        DDSDDE(1,1) = KK
    ENDIF
    DDSDDE(2,2) = CFULL(2,2)-KSH*COEFF*DELTA1**2
    DDSDDE(3,3) = CFULL(3,3)-KSH*COEFF*DELTA2**2
    DDSDDE(1,2) = -KK*COEFF*DELTA1*DELTA3
    DDSDDE(2,1) = -KSH*COEFF*DELTA1*DELTA3
    IF (NTENS.EQ.THREE) THEN
        DDSDDE(1,3) = -KK*COEFF*DELTA2*DELTA3
        DDSDDE(3,1) = -KSH*COEFF*DELTA2*DELTA3
        DDSDDE(2,3) = -KSH*COEFF*DELTA1*DELTA2
        DDSDDE(3,2) = DDSDDE(2,3)
    ENDIF
ELSE
    DDSDDE(1,1) = CFULL(1,1)
    DDSDDE(2,2) = CFULL(2,2)
    IF (NTENS.EQ.THREE) THEN
        DDSDDE(3,3) = CFULL(3,3)
    END IF
ENDIF

STATEV(1) = DMG
RETURN
END
```

Appendix B

Subroutine for Fatigue Loading

```fortran
SUBROUTINE UMAT(STRESS,STATEV,DDSDDE,SSE,SPD,SCD,
1 RPL,DDSDDT,DRPLDE,DRPLDT,
2 STRAN,DSTRAN,TIME,DTIME,TEMP,DTEMP,PREDEF,DPRED,CMNAME,
3 NDI,NSHR,NTENS,NSTATV,PROPS,NPROPS,COORDS,DROT,PNEWDT,
4 CELENT,DFGRD0,DFGRD1,NOEL,NPT,LAYER,KSPT,JSTEP,KINC)

INCLUDE 'ABA_PARAM.INC'

CHARACTER*80 CMNAME, CPNAME
DIMENSION STRESS(NTENS),STATEV(NSTATV),
1 DDSDDE(NTENS,NTENS),DDSDDT(NTENS),DRPLDE(NTENS),
2 STRAN(NTENS),DSTRAN(NTENS),TIME(2),PREDEF(1),DPRED(1),
3 PROPS(NPROPS),COORDS(3),DROT(3,3),DFGRD0(3,3),DFGRD1(3,3),
4 JSTEP(4)

DIMENSION CFULL(NTENS,NTENS), DELTAT(NTENS)
DOUBLE PRECISION KK, SIGMA3C, TAU1C, TAU2C, G1C, G2C, G3C, ...
    ETA
DOUBLE PRECISION G1TH, RATIO, C1, M1, WIDTH, E3
DOUBLE PRECISION ACZ, BETA, BI, COEFF, DADN, DDDN, DELTA, ...
    DELTA0
DOUBLE PRECISION DELTA0_3, DELTA_0SHEAR, DELTA1, DELTA2, ...
    DELTA3
DOUBLE PRECISION DELTAF, DELTAG, DELTAN_MAX, DELTA_SHEAR
DOUBLE PRECISION DELTA_OLD, DMG_OLD, DMG, DMG_STAT, DMG_FAT
DOUBLE PRECISION DMG_MAX, G_MAX, G_MAX_OLD, RT_OLD, RT, ...
    TAU_OLD
DOUBLE PRECISION TAU, COEFF1, CF2, CF3, CF4, CF6, CF7, PI, Q
```

```
DOUBLE PRECISION E_I, E_II, E_M, G_C, TAU_MC, E11, E22, ...
   G12, V21
DOUBLE PRECISION KSH, KB, DELTAC_3, DELTAC_SHEAR, ...
   DDDN_OLD,DISP
DOUBLE PRECISION CRACK, COMPL, CHI, LAMBDA, FORCE, SERR, ...
   LEVER

PARAMETER(ZERO=0.D0, ONE=1.D0, TWO=2.D0, THREE=3.D0, ...
   NINE=9.D0)
PARAMETER(THIRTYTWO=32.D0, PI = TWO*ASIN(ONE))

INTEGER KFLAG
COMMON KFLAG


KK         = PROPS(1)
SIGMA3C    = PROPS(2)
TAU1C      = PROPS(3)
TAU2C      = PROPS(4)
G1C        = PROPS(5)
G2C        = PROPS(6)
G3C        = PROPS(7)
ETA        = PROPS(8)
G1TH         = PROPS(9)
RATIO      = PROPS(10)
C1       = PROPS(11)
M1       = PROPS(12)
WIDTH        = PROPS(13)
E3       = PROPS(14)
DMG_MAX    = PROPS(15)
E11          = PROPS(16)
E22      = PROPS(17)
G12      = PROPS(18)
V21      = PROPS(19)

DMG_OLD = STATEV(1)
TAU_OLD = STATEV(2)
DELTA_OLD = STATEV(3)
G_MAX_OLD = STATEV(4)
DDDN_OLD = STATEV(6)

!DISPLACEMENT AT THE END OF THE INCREMENT
DO I = 1, NTENS
    DELTAT(I) = STRAN(I) + DSTRAN(I)
END DO

!DISPLACEMENT INCREMENTS
```

```
DELTA3 = DELTAT(1)
DELTA1 = DELTAT(2)
!IF THE ANALYSIS IS IN 2D: DELTA2 IS ZERO, IF IT IS 3D: ...
   DELTA2 IS THE THIRD ELEMENT
IF (NTENS.EQ.TWO) THEN
    DELTA2 = ZERO
ELSE
    DELTA2 = DELTAT(3)
ENDIF

DELTA_SHEAR = SQRT(DELTA1**2+DELTA2**2)

!MIXED-MODE RATIO
BETA = DELTA_SHEAR/(MAX(DELTA3,ZERO)+DELTA_SHEAR)
KSH = G1C/G2C*(TAU2C/SIGMA3C)**2*KK
CF6 = KSH*DELTA_SHEAR**2 + KK*MAX(DELTA3,ZERO)**2
CF7 = KSH**2*DELTA_SHEAR**2 + KK**2*MAX(DELTA3,ZERO)**2
BI= (KSH*DELTA_SHEAR**2)/CF6
!Mixed-mode penalty stiffness
KB = KK*(ONE-BI)+KSH*BI
!DISPLACEMENT JUMP NORM
DELTA = CF6/SQRT(CF7)
!PURE MODE ONSET DISPLACEMENT JUMP
DELTA_0SHEAR = TAU1C/KSH
DELTA0_3 = SIGMA3C/KK
!MIXED-MODE ONSET DISPLACEMENT JUMP
CF4 = (KSH*DELTA_0SHEAR**2-KK*DELTA0_3**2)*(BI**ETA)
DELTA0=SQRT((KK*DELTA0_3**2+CF4)/(KB))
!MIXED-MODE FINAL DISPLACEMENT JUMP
DELTAC_SHEAR = TWO*G2C/TAU1C
DELTAC_3 = TWO*G1C/SIGMA3C
CF5 = (KSH*DELTA_0SHEAR*DELTAC_SHEAR-KK*DELTA0_3*DELTAC_3)
DELTAF = (KK*DELTA0_3*DELTAC_3+CF5*(BI**ETA))/(KB*DELTA0)
!INTERNAL VARIABLE
RT_OLD = (DELTA0*DELTAF)/(DELTAF-DMG_OLD*(DELTAF-DELTA0))
RT = MAX(RT_OLD,DELTA)
IF (DELTA.GT.RT_OLD) THEN
    DMG_STAT = (DELTAF*(RT-DELTA0))/(RT*(DELTAF-DELTA0))
    DMG_STAT = MIN(DMG_STAT,ONE)
ELSE
    DMG_STAT = DMG_OLD
ENDIF


TAU = DELTA * KB * (ONE-DMG_STAT)
!==========================Mixed-mode parameters
Q = SQRT(TWO*(SQRT(E22/E11)-V21)+E22/G12)/TWO
```

```
E_I = E22/Q
E_II = E22/Q*SQRT(E11/E22)
TAU_MC = SQRT(SIGMA3C**2+(TAU1C**2-SIGMA3C**2)*(BI**ETA))
G_C = G1C+(G2C-G1C)*(BI**ETA)
E_M = E_I*(ONE-BI)+E_II*BI
!==========================Fatigue=================================
IF (TIME(2).GT.ONE .AND. DMG_STAT .LT. ONE) THEN
    !!====CALCULATE DMG WITH OLD DDDN====
    DMG_FAT = DDDN_OLD*DTIME
    DMG = DMG_STAT+DMG_FAT
    DMG = MIN(DMG,ONE)
    !!====COMPUTE NEW DDDN====
    !SERR
    IF (DELTA .GT. ZERO) THEN
        COEFF1 = (DELTAF - (DELTAF - DELTA)**2/(DELTAF - ...
           DELTA0))
        IF (DMG_FAT .EQ. ZERO) THEN
            G_MAX = DELTA0 * KB/TWO*COEFF1
        ELSE
            TAU = DELTA * KB * (ONE-DMG)
            G_MAX=G_MAX_OLD + ...
               (TAU+TAU_OLD)*(DELTA-DELTA_OLD)/TWO
        END IF
        DELTAG = G_MAX*(ONE-RATIO**2)
        !CRACK GROWTH RATE
        IF (G_MAX.GT.ZERO.AND.G_MAX.LT.G_C) THEN
            IF (KFLAG .EQ. 0) THEN
                DADN = C1*(G_MAX)**M1
                !AREA OF COHESIVE ZONE
                ACZ = 0.1D0*(E_M*G_MAX)/((TAU_MC)**2)
                !DAMAGE VARIABLE AS A FUNCITON OF CYCLES
                CF2 = DELTAF*DELTA0*ACZ
                CF3 = ONE-DMG
                DDDN=DADN*(DELTAF*CF3+DMG*DELTA0)**2/(CF2)
                !MAX NUMBER OF CYCLES
                DELTAN_MAX = DMG_MAX/DDDN
                !CHECK FOR MAX NUMBER OF CYCLES
                IF (DTIME.GT.DELTAN_MAX) THEN
                    PNEWDT = 0.8*DELTAN_MAX/DTIME
                END IF
                !CHECK G_TH IF ELEMENT HAS JUST FAILED
                IF ((DMG .EQ. ONE) .AND. (DMG_OLD .LT. ...
                   ONE)) THEN
                    IF (C1 .GT. 10.D0) THEN
                        LEVER = 92.9D0
                        DISP = 1.27D0
                    ELSE
```

```
                        LEVER = 41.3D0
                        DISP = 1.04D0
                    END IF
                    !CALCULATION OF FINAL CRACK WITH LEFM, ...
                       ONLY FOR MMB
                    LAMBDA = 1.18D0*SQRT(E11*E22)/G12
                    CHI = SQRT(E11/(11.D0*G12)*(THREE-...
                      TWO*(LAMBDA/(ONE+LAMBDA))**2))
                    COMPL=(4.D0*(THREE*LEVER-50.4D0)**2*...
                      (CRACK+CHI*2.25D0)**3+(LEVER+50.4D0)**2*...
                      (TWO*50.4D0**3+THREE*(CRACK+0.42D0*...
                      CHI*2.25D0)**3))/(8.D0*25.4D0*2.25D0**3...
                      *50.4D0**2*E11)
                    FORCE = DISP/COMPL
                    SERR=(12.D0*(THREE*LEVER-50.4D0)**2*...
                    (CRACK+CHI*2.25D0)**2+9.D0*(LEVER+50.4D0)**2...
                    *(CRACK+0.42D0*CHI*2.25D0)**2)*FORCE**2...
                    /(16.D0*25.4D0**2*50.4D0**2*2.25D0**3*E11)
                    IF (SERR .LT. G1TH) THEN
                        KFLAG = 1
                    ELSE
                        KFLAG = 0
                    END IF
                END IF
            ELSE
            !NO INCREASE IN DAMAGE IF G IS NOT BETWEEN THE ...
               BOUNDARIES
                DDDN = ZERO
            END IF
        END IF
    END IF
ELSE
    DMG = DMG_STAT
ENDIF

!FULL STIFFNESS MATRIX
DO I = 1, NTENS
    DO J = 1, NTENS
        CFULL(I,J)=ZERO
    END DO
END DO
IF (DELTA3.GE.ZERO) THEN
    CFULL(1,1) = KK*(ONE-DMG)
ELSE
    CFULL(1,1) = KK
ENDIF
CFULL(2,2) = KSH*(ONE-DMG)
```

```
!CFULL(3,3) ONLY EXISTS IN 3D
IF (NTENS.EQ.THREE) THEN
    CFULL(3,3) = KSH*(ONE-DMG)
ENDIF

!STRESS CALCULATION
DO I = 1, NTENS
    STRESS(I)=ZERO
    DO J = 1, NTENS
        STRESS(I)=STRESS(I)+CFULL(I,J)*DELTAT(J)
    END DO
END DO

!TANGENT STIFFNESS MATRIX
DO I = 1, NTENS
    DO J = 1, NTENS
        DDSDDE(I,J)=ZERO
    END DO
END DO

IF (DELTA.GT.RT_OLD.AND.DELTA.LT.DELTAF) THEN
    COEFF = ((DELTAF*DELTA0)/((DELTAF-DELTA0)*DELTA**3))
    IF (DELTA3.GE.ZERO) THEN
        DDSDDE(1,1) = CFULL(1,1)-KK*COEFF*DELTA3**2
    ELSE
        DDSDDE(1,1) = KK
    ENDIF
    DDSDDE(2,2) = CFULL(2,2)-KSH*COEFF*DELTA1**2
    DDSDDE(3,3) = CFULL(3,3)-KSH*COEFF*DELTA2**2
    DDSDDE(1,2) = -KK*COEFF*DELTA1*DELTA3
    DDSDDE(2,1) = -KSH*COEFF*DELTA1*DELTA3
    IF (NTENS.EQ.THREE) THEN
        DDSDDE(1,3) = -KK*COEFF*DELTA2*DELTA3
        DDSDDE(3,1) = -KSH*COEFF*DELTA2*DELTA3
        DDSDDE(2,3) = -KSH*COEFF*DELTA1*DELTA2
        DDSDDE(3,2) = DDSDDE(2,3)
    ENDIF
ELSE
    DDSDDE(1,1) = CFULL(1,1)
    DDSDDE(2,2) = CFULL(2,2)
    IF (NTENS.EQ.THREE) THEN
        DDSDDE(3,3) = CFULL(3,3)
    END IF
END IF

STATEV(1) = DMG
STATEV(2) = TAU
```

```
STATEV(3) = DELTA
STATEV(4) = G_MAX
STATEV(5) = DADN
STATEV(6) = DDDN
STATEV(7) = BETA
STATEV(8) = BI
STATEV(9) = ACZ
STATEV(10) = TAU
STATEV(11) = KSH

RETURN
END
```